

Compensation for Impairments of Frequency Converters in Millimeter Wave Vector Signal Generators

by

Arthur Chung

A thesis
presented to the University of Waterloo
in fulfillment of the
thesis requirement for the degree of
Master's of Applied Science
in
Electrical Engineering

Waterloo, Ontario, Canada, 2018

© Arthur Chung 2018

I hereby declare that I am the sole author of this thesis. This is a true copy of the thesis, including any required final revisions, as accepted by my examiners.

I understand that my thesis may be made electronically available to the public.

Abstract

The upcoming fifth generation (5G) of wireless communications aims to utilize millimeter wave (mm-wave) frequencies in its infrastructure to alleviate the crowded spectrum problem below 6 GHz. At higher frequencies, modulation bandwidths of several hundreds of MHz can be utilized to increase system capacities. However, the radio frequency (RF) frontends can exhibit significant amounts of impairments over these wide bandwidths, thereby limiting the achievable output signal quality and capacity. In this work, two signal generation architectures and the accompanying compensation schemes to mitigate the impairments are proposed for the generation of wideband modulated signals at mm-wave frequencies.

The frequency dependent IQ imbalance effects in conventional direct conversion signal generation architectures over ultra wide bandwidths are first investigated. For that, a new interleaved multi-tone test signal based identification and compensation scheme is proposed. This scheme was experimentally validated by using an off-the-shelf IQ mixer operating at 30 GHz driven with an interleaved multi-tone signal with 4 GHz of modulation bandwidth and achieving a reduction in the normalized mean squared error (NMSE) from -14 dB to -38 dB. Subsequently, a low-complexity pruned Volterra series based digital predistortion (DPD) scheme was devised to mitigate the nonlinear distortions exhibited by the power amplifier stage and maximize the signal quality of orthogonal frequency division multiplexing (OFDM) signals with modulation bandwidths up to 800 MHz. After compensation of the system with 66 DPD coefficients, the OFDM signal with 800 MHz of modulation bandwidth exhibited an NMSE of -32.4 dB and an adjacent channel power ratio (ACPR) of 45 dBc.

However, the challenges associated with the implementation of traditional direct conversion architectures exacerbate as the operating frequency increases. For instance, the performance of high frequency active building blocks, e.g. mixer and amplifiers, deteriorates as the operating frequency approaches the maximum oscillation frequency of the semiconductor technology. To address this challenge, a signal generation system utilizing frequency multipliers to replace the mixer and facilitate frequency upconversion is proposed. A novel Volterra series based behavioural model is also devised to predict the nonlinear behaviour of frequency multipliers and to form the basis for synthesizing a DPD scheme capable of obtaining acceptable signal quality when driven with wideband modulated signals. Various frequency multiplier based signal generation systems were implemented using off-the-shelf frequency doublers, triplers, and quadruplers to serve as proof of concept prototypes. Experiments confirmed the ability to generate modulated signals with competitive error vector magnitudes (EVM) and ACPR levels with low complexity DPD schemes.

Acknowledgements

I would like to thank my supervisor Professor Boumaiza for providing me with his guidance in this research work and the opportunity to take part in the research activities of the Emerging Radio Systems Group (EmRG). I would also like to thank Professor Mitran for his help and support in the research of frequency multiplier based vector signal generators.

Thank you to all of my fellow EmRG lab members for their mentorship, encouragement and discussions in the office and in the laboratory. Thank you to Yehia, Marwen, and Peter for their support and mentorship in learning about digital predistortion, RF measurement setups, and RF systems.

Thank you to my family for their support and encouragement.

Table of Contents

List of Tables	vii
List of Figures	viii
1 Introduction	1
2 Background Theory	5
2.1 Overview of IQ Imbalance Effects	5
2.2 Overview of Digital Predistortion Theory	7
3 IQ Imbalance Compensation and Digital Predistortion for Millimeter-Wave Signal Generation Using a Reduced Sampling Rate Transmitter Observation Receiver	13
3.1 Literature Review	13
3.2 Wideband IQ Imbalance Detection and Compensation Scheme	16
3.2.1 Proposed IQ Imbalance Detection and Compensation	16
3.2.2 IQ Imbalance Detection With a Sub-Nyquist Rate Transmitter Observation Receiver	21
3.3 Test and Measurement Results	26
3.3.1 Test and Measurement Setup	26
3.3.2 Ultra-wideband IQ Imbalance Compensation Results	27
3.3.3 DPD Measurement Results	30
3.4 Conclusions	34

4	Digital Predistortion for Frequency Multiplier Based High Frequency Wideband Signal Generators	36
4.1	Literature Review	38
4.2	Frequency Multiplier Behavioural Models	39
4.3	Digital Predistortion for Frequency Multipliers Driven With Vector Modulated Signals	44
4.4	Statistical Noise Analysis for Frequency Multipliers	47
4.5	Test and Measurement Results	53
4.5.1	Linearization of a Single Frequency Doubler	56
4.5.2	Linearization of a Frequency Quadrupler	57
4.5.3	Linearization of a Frequency Tripler	62
4.6	Conclusions	65
5	Conclusions	66
5.1	Future Work	67
	References	68

List of Tables

3.1	Measured VSG signal quality results before and after IQ imbalance detection and compensation with the time and proposed frequency domain based methods	29
3.2	Measured results of the proposed IQ imbalance detection and compensation method with the modified 4 GHz interleaved multi-tone test signal with 200 tones using a NR and sub NR TOR	31
3.3	Summary of the measured signal quality before and after linearization of a mm-wave PA using the reduced complex baseband sampling TOR	34
4.1	Simulated impact of a noiseless and distortionless frequency multiplier on the input noise signal given an input signal power of $E \tilde{z}(n) ^2 = 0$ dBm and an output signal power of $E [(\tilde{z}(n) ^2)^D] = 0$ dBm	53
4.2	Linearization results for the frequency doubler system generating OFDM signals at 12.5 GHz	57
4.3	Linearization results for a frequency quadrupler generating OFDM signals at 25 GHz	62
4.4	Linearization results for the frequency tripler system generating OFDM signals at 63 GHz	62

List of Figures

1.1	(a) Direct conversion TX architecture (b) Heterodyne TX architecture. . .	2
2.1	Direct conversion upconversion stage block diagram.	6
2.2	IQ imbalance and compensator model real valued filters.	7
2.3	Example of (a) the envelope’s magnitude and spectrum of an OFDM signal with a 320 MHz modulation bandwidth with a PAPR of 8.6 dB (b) a PA’s gain and PAE characteristics versus input power.	8
2.4	TX with a TOR for IQ imbalance detection and DPD training.	9
2.5	Example of gain and phase distortion curves for a PA, its PD, and the resulting linearized PA.	10
2.6	Learning architectures to train the predistorter modules: (a) Indirect learning (b) Direct learning.	12
3.1	IQ imbalance and compensator models using (a) complex valued filters or (b) real valued filters.	14
3.2	Joint IQ imbalance and DPD model structure.	15
3.3	Effects of the IQ imbalance on the interleaved multi-tone test signal on the interleaved multi-tones.	17
3.4	Computational complexity comparison for IQ imbalance detection and compensation of the time domain and proposed frequency domain method. . .	22
3.5	Without careful construction of the proposed interleaved multi-tone test signal, aliased tones from the 2nd Nyquist zone ($p = 2$) overlap with the non-aliased tones in the reduced sampling rate TOR.	23

3.6	(a) Setting the frequency offset in the proposed interleaved multi-tone test signal avoids overlap from aliasing allowing for estimation of the Nyquist rate sampled output. (b) Increasing the sub-sampling ratio requires more frequency offsets to be introduced into the multi-tone structure to avoid overlap from the aliasing. In this case, 2 offsets are introduced to prevent overlap from the 2nd and 3rd Nyquist zones where $p = 2$, and $p = 3$, respectively.	24
3.7	Reconstructing the NR signal from the sub-sampled signal.	25
3.8	mm-wave test and measurement setup to validate the proposed IQ imbalance detection and compensation scheme [27]–[29].	27
3.9	Measured IQ imbalance filter frequency responses of the direct conversion signal generation system at 30 GHz across 4 GHz: (a) magnitude response, (b) phase response.	28
3.10	Reconstructed NR rate signal using the sub-sampling TOR at sub-sampling ratios of 2, 4, 8 for IQ imbalance detection.	30
3.11	Measured spectra of the mm-wave PA output when driven with ultra-wideband signals at 30 GHz with the reduced sampling rate TOR with sub-sampling ratios of 4 and 8. (a) 320 MHz carrier aggregated OFDM signals (b) 800 MHz carrier aggregated OFDM signal.	33
4.1	(a) Conventional signal generation system (b) Nonlinear mixer based signal generation (c) Frequency multiplier based signal generation system.	37
4.2	Frequency multiplier model and its complex baseband equivalent model.	39
4.3	Frequency multiplier DPD module and the frequency multiplier based vector signal generator block diagram.	45
4.4	Frequency multiplier model used for noise analysis.	47
4.5	Output noise power versus the input signal to noise ratio assuming $\sigma_s^2 = 1$ W for distortionless and noiseless PAs, doublers, triplers, and quadruplers.	52
4.6	Output spectra of an ideal frequency multiplier (a) without predistortion applied, and (b) with predistortion applied.	54
4.7	Test setup for investigating frequency multiplier based signal generation [27], [29], [55], [56]	55

4.8	Measured output spectra of a frequency doubler driven with an OFDM signal with (a) 200 MHz of modulation bandwidth, (b) 400 MHz of modulation bandwidth.	58
4.9	Distortion curves of a frequency doubler driven by an OFDM signal with 400 MHz of modulation bandwidth: (a) gain distortion, (b) phase distortion.	59
4.10	Demodulated and equalized OFDM signal's constellations for a linearized frequency doubler driven with (a) 200 MHz of modulation bandwidth at 12.5 GHz for case (d), (b) 400 MHz of modulation bandwidth at 12.5 GHz for case (d).	59
4.11	Measured output spectra of a frequency quadrupler driven with an OFDM signal with (a) 200 MHz of modulation bandwidth, (b) 400 MHz of modulation bandwidth.	60
4.12	Distortion curves of a frequency quadrupler when driven by an OFDM signal with 400 MHz modulation bandwidth: (a) gain distortion, and (b) phase distortion.	61
4.13	Demodulated and equalized OFDM signal's constellations for a Linearized frequency quadrupler driven with (a) 200 MHz of modulation bandwidth at 25 GHz for case (d), and (b) 400 MHz of modulation bandwidth at 25 GHz for case (d).	61
4.14	Measured output spectra of a frequency tripler driven with an OFDM signal with a (a) 200 MHz modulation bandwidth, (b) 400 MHz modulation bandwidth.	63
4.15	Distortion curves of a frequency tripler when driven with an OFDM signal with 400 MHz modulation bandwidth: (a) gain distortion (b) frequency phase distortion.	64
4.16	Demodulated and equalized OFDM signal's constellations for a linearized frequency tripler driven with (a) 200 MHz of modulation bandwidth at 63 GHz for case (d), (b) 400 MHz modulation bandwidth at 63 GHz for case (d).	64
5.1	Achieved signal quality in the investigation of frequency multiplier based vector signal generation systems for OFDM signals with modulation bandwidths of (a) 160 and 200 MHz and (b) 320 and 400 MHz [33].	67

Chapter 1

Introduction

In the current generation of wireless communications, the crowded spectrum below 6 GHz poses a limitation on the achievable data rate due to the limited available bandwidth [1]–[3]. This poses an issue for the targeted fifth Generation (5G) applications [2], such as enhanced mobile, machine to machine, and vehicle to vehicle communications. To alleviate this issue, the upcoming 5G infrastructure targets operation in the millimeter-wave (mm-wave) frequency bands and as a result, it enables the transmission of signals with modulation bandwidths spanning several hundreds of MHz for achieving a higher overall system capacity [1]–[3]. This enables wideband communication systems to achieve low latency, reliable communications, and peak data rates in the multi-Gb/s range [1], [3].

However, mm-wave radio frequency (RF) frontends suffer from an increased amount of impairments over these wide modulation bandwidths resulting in degradation of the transmitted signal quality in terms of the normalized mean squared error (NMSE) between the transmitted signal and the desired signal, error vector magnitude (EVM) and adjacent channel power ratio (ACPR). The degraded signal quality results in a reduced achievable system capacity. This motivates the need to explore transmitter (TX) architectures and signal processing techniques at the system level to mitigate these impairments. Conventional TX systems can be described by either the direct conversion architecture shown in Fig. 1.1(a) or the heterodyne architecture shown in Fig. 1.1(b). The difference between the architectures is that the direct conversion architecture generates the in-phase (I) and quadrature (Q) signals at baseband from the digital to analog converter (DAC) and an IQ mixer upconverts the signal directly to an RF frequency, while the heterodyne architecture requires the DAC to generate the signal at an intermediate frequency (IF) prior to an additional stage of frequency upconversion. Since the DAC generates the signal at an IF in the heterodyne architecture, the DAC would have a higher sampling rate requirement,

which grows with the signal bandwidth. The heterodyne architecture would also require a bandpass filter (BPF) at the output to filter out the unwanted sideband that would be present due to the IQ imbalance in the IQ mixer. In comparison, the direct conversion architecture requires a lower sampling rate DAC as the signal is generated at baseband, and the baseband signal is then directly upconverted to an RF frequency through the IQ mixer without generating an unwanted sideband. However in the direct conversion architecture, when the frequency dependent IQ imbalance effects are not properly addressed, the output signal quality will be significantly deteriorated.

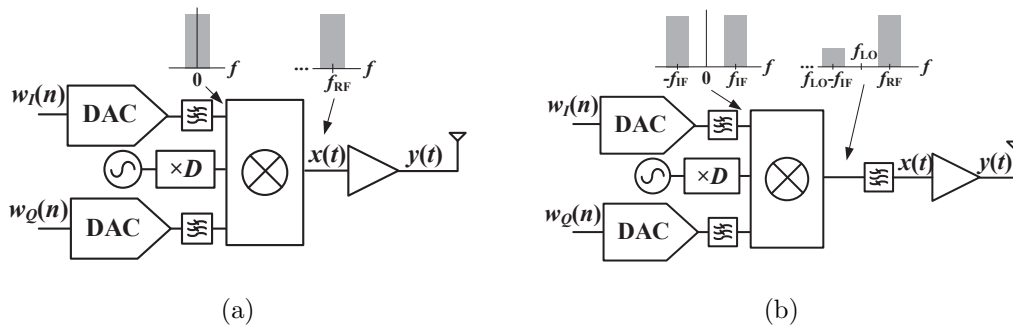


Figure 1.1: (a) Direct conversion TX architecture (b) Heterodyne TX architecture.

Furthermore, achieving spectrally efficient communication requires more sophisticated modulation schemes such as quadrature amplitude modulation (QAM) or orthogonal frequency division multiplexing (OFDM), which exhibit high peak-to-average power ratios (PAPRs). With the non-constant envelope signals, the system engineer could operate the amplitude sensitive components, e.g. the power amplifier (PA), in their power back-off region to avoid nonlinear distortions. However when the PA is operated in its power backoff region, it would operate with a degraded power efficiency. To mitigate the nonlinear distortions in the high efficiency region of operation, several linearization techniques have been explored. For instance, digital predistortion (DPD) is a technique that compensates for the nonlinear behaviour of the PA and has been implemented in the previous generations of wireless communication systems [4]. The extension of the DPD schemes for wideband linearization of mm-wave PAs is to be investigated for efficiently generating high quality wideband signals.

Given the significant IQ imbalance effects in direct conversion architectures, this thesis proposes an interleaved multi-tone test signal based wideband IQ imbalance identification and compensation scheme using a reduced sampling transmitter observation receiver

(TOR). Subsequently, a low-complexity pruned Volterra series based DPD scheme is constructed for the linearization of mm-wave PAs driven with wideband signals.

However with an increasing operating frequency, generating high quality wideband signals with an appropriate output power, and power efficiency becomes increasingly difficult. For instance, active components such as mixers and amplifiers are limited in their performance by the breakdown voltages and maximum oscillation frequency (f_{\max}) of semiconductor technologies [5]. In an attempt to tackle these challenges that conventional direct conversion architectures can face at frequencies near and above f_{\max} , this thesis proposes a frequency multiplier based signal generator utilizing frequency multipliers for frequency up-conversion of wideband vector modulated signals to the mm-wave and sub-terahertz (sub-THz) frequencies. For this, a complex baseband equivalent (CBBE) Volterra series is first derived for the behavioural modelling of frequency multipliers. A DPD scheme is then presented for compensating for the nonlinear distortions generated by frequency multipliers when driven with non-constant envelope signals. The validation of this approach at the mm-wave frequencies serves as a proof of concept for its extension to the sub-THz frequency ranges.

This thesis is organized into the following chapters. First the background theory behind IQ imbalance and DPD are given in Chapter 2. Chapter 3 then begins with providing a literature review of the compensation schemes for IQ imbalance, and joint IQ imbalance and DPD. Afterwards, the proposed interleaved multi-tone test signal based IQ imbalance detection and compensation scheme, and low complexity DPD scheme is introduced. Subsequently in Chapter 4, a literature review on the current techniques to generate high frequency vector modulated signals at the high frequency ranges are described. Afterwards a review of the literature on high frequency signal generation and DPD schemes for frequency multipliers are discussed. Then, the proposed frequency multiplier based vector modulated signal generation architecture and compensation schemes are presented. Lastly, the conclusions and the future work of this thesis are summarized in Chapter 5.

Notation: The column vector $[b_1, \dots, b_n]^T$ is denoted by a lower case boldface font \mathbf{b} , while its sub-vector $[b_i, \dots, b_j]^T$ is denoted by b_i^j . A matrix of size $n \times m$ is denoted by an upper case boldface font \mathbf{B} , while its $m \times n$ transpose is denoted by \mathbf{B}^T , and its $m \times n$ Hermitian transpose is denoted by \mathbf{B}^H . The product of n scalar differentials $d\tau_1 \cdots d\tau_n$ is written as $d\boldsymbol{\tau}_n$. Sets are denoted with calligraphic type, e.g. \mathcal{S} . The space of real numbers is denoted by \mathbb{R} , and the space of complex numbers is denoted by \mathbb{C} . The real part of the variable $b \in \mathbb{C}$ is denoted by $\mathcal{R}\{b\}$ and its complex conjugate is denoted by b^* . The CBBE signal of the passband signal $b(t)$ is denoted by $\tilde{b}(t)$. Given the integers, $1, \dots, n$, we let \mathcal{P}_n denote the set of $n!$ permutations. A permutation $\pi \in \mathcal{P}_n$ on a vector \mathbf{b} results in the reordering of the elements in $\mathbf{b} = [b_1, \dots, b_n]$ according to π , i.e. it is defined as $\pi(\mathbf{b}) = [b_{\pi(1)}, \dots, b_{\pi(n)}]^T$.

For example, a permutation $\pi \in \mathcal{P}_n$, with $\pi(2) = 4$, $\pi(4) = 2$, and otherwise $\pi(i) = i$ (i.e. a permutation that swaps the first and third element) applied to $\mathbf{b} = [24, 52, 35, 0, 7]^T$ results in $\pi(\mathbf{b}) = [24, 0, 35, 52, 7]^T$. We also define the subset $\mathcal{P}_n(k) \subset \mathcal{P}_n$ to be the permutations that preserve the relative order of the first k and last $n - k$ elements, it is defined as $\mathcal{P}_n(k) = \{\pi \in \mathcal{P}_n \mid \pi(1) < \pi(2) < \dots < \pi(k), \pi(k+1) < \pi(k+2) < \dots < \pi(n-k)\}$. The expectation operator is denoted by $\mathbb{E}[\cdot]$.

Chapter 2

Background Theory

2.1 Overview of IQ Imbalance Effects

The detailed block diagram of the upconversion stage of the direct conversion architecture is shown in Fig. 2.1. The IQ imbalance arises from the analog components through the following effects. First, the amplitudes of each path differ, which is caused by the frequency dependent gain imbalance between the two paths. Secondly, a hybrid 90° coupler is used to drive the mixers with two local oscillator (LO) signals that are ideally 90° out of phase. The non-ideality of the hybrid 90° coupler can result in a phase offset from the ideal 90° offset between the two paths. Thirdly, the phase response of the components in the two paths are not matched over the entire frequency range of operation resulting in frequency dependent phase imbalance. Lastly, DC offsets between the two paths from the DAC can result in an additional LO feedthrough at the output.

In order to model these effects, we first consider the case of narrowband signals; hence, frequency independent effects can be considered. As illustrated in Fig. 2.1, the I and Q mixers have gains of h_1 and h_2 and are fed with LO signals with a frequency of ω_{LO} , the hybrid 90° has a phase offset of ϕ , and the DC offsets of $V_{I,\text{offset}}$ and $V_{Q,\text{offset}}$ are injected by the DAC. We can then compute the RF signal, $x(t)$, resulting from the upconversion of the I component, $w_I(t)$, and the Q component, $w_Q(t)$, through

$$\begin{aligned} x(t) &= x_I(t) + x_Q(t) \\ &= h_1(w_I(t) + V_{I,\text{offset}}) \cos(\omega_{LO}t) - h_2(w_Q(t) + V_{Q,\text{offset}}) \sin(\omega_{LO}t - \phi) \\ &= (h_1(w_I(t) + V_{I,\text{offset}}) + h_2 \sin(\phi)(w_Q(t) + V_{Q,\text{offset}})) \cos(\omega_{LO}t) \\ &\quad - h_2 \cos(\phi)(w_Q(t) + V_{Q,\text{offset}}) \sin(\omega_{LO}t). \end{aligned} \tag{2.1}$$

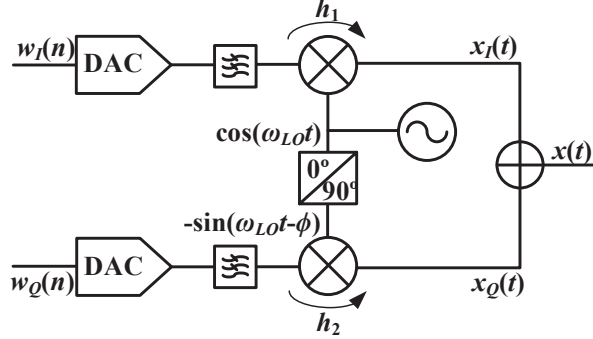


Figure 2.1: Direct conversion upconversion stage block diagram.

From (2.1), we can write this in its CBBE form in matrix notation as

$$\begin{bmatrix} \tilde{x}_I(t) \\ \tilde{x}_Q(t) \end{bmatrix} = \underbrace{\begin{bmatrix} h_1 & h_2 \sin(\phi) \\ 0 & h_2 \cos(\phi) \end{bmatrix}}_{\tilde{\mathbf{H}}} \begin{bmatrix} \tilde{w}_I(t) \\ \tilde{w}_Q(t) \end{bmatrix} + \begin{bmatrix} \tilde{x}_{I,\text{offset}} \\ \tilde{x}_{Q,\text{offset}} \end{bmatrix}, \quad (2.2)$$

where $\tilde{\mathbf{H}}$ is the IQ imbalance matrix. Due to the phase imbalance, the I component of the output signal $x(t)$ contains a portion of the input signal's Q component. If we only consider gain imbalance to be present, then the cross term $h_2 \sin(\phi) = 0$, but the output would have amplitude mismatch between the I and Q components. The DC offsets contribute to an LO feedthrough term and this is problematic because the LO feedthrough term in direct conversion architectures lies directly in the center of the output signal. This feedthrough term can also add destructively or constructively with the leaked LO signal attributed to the finite LO-RF isolation of the mixers. For the IQ imbalance to not have an effect on the signal quality, $h_1 = h_2$, and $\phi = 0$. To compensate the frequency independent effects, only the gain imbalance and phase offset parameters have to be determined. Afterwards, the signals can be compensated by applying $\tilde{\mathbf{H}}^{-1}$ prior to sending the signal to the DACs.

In the case with wideband signals where frequency dependent IQ imbalance effects are present, then we can no longer consider the gains to be constants. At complex baseband, the four real valued filter model shown in Fig. 2.2 can be adopted [6]. The input signal,

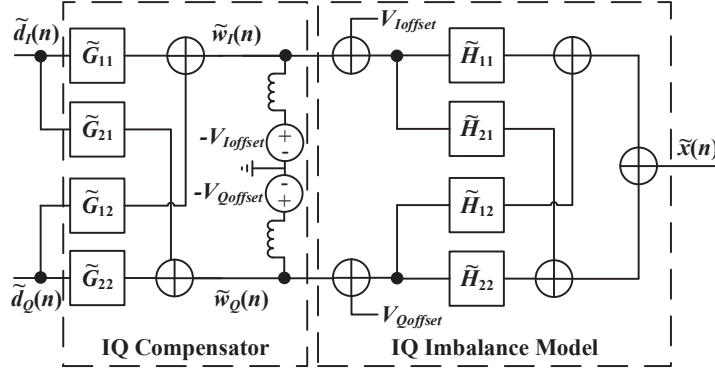


Figure 2.2: IQ imbalance and compensator model real valued filters.

$\tilde{w}(n) = \tilde{w}_I(n) + j\tilde{w}_Q(n)$, is related to the output signal $\tilde{x}(n) = \tilde{x}_I(n) + j\tilde{x}_Q(n)$ through

$$\begin{aligned} \tilde{x}(n) = & \sum_{i=0}^M \tilde{h}_{11}(i)\tilde{w}_I(n-i) + \sum_{i=0}^M \tilde{h}_{12}(i)\tilde{w}_Q(n-i) \\ & + j \left(\sum_{i=0}^M \tilde{h}_{22}(i)\tilde{w}_Q(n-i) + \sum_{i=0}^M \tilde{h}_{21}(i)\tilde{w}_I(n-i) \right), \end{aligned} \quad (2.3)$$

where M is the order of the IQ imbalance FIR filters, $\tilde{h}_{11}(n)$, $\tilde{h}_{12}(n)$, $\tilde{h}_{21}(n)$, $\tilde{h}_{22}(n)$. If there were no gain or phase imbalances in the direct conversion architecture, then $\tilde{h}_{12}(n) = \tilde{h}_{21}(n) = 0$ and $\tilde{h}_{11}(n) = \tilde{h}_{22}(n)$. The frequency independent case is also a special case of the four real valued filter model when $M = 0$, where $\tilde{h}_{11}(n) = h_1$, $\tilde{h}_{12}(n) = h_2 \sin(\phi)$, $\tilde{h}_{21}(n) = 0$, and $\tilde{h}_{22}(n) = h_2 \cos(\phi)$. Although the model is simplistic, the challenge of compensating for the IQ imbalance effects is in the identification of the four filters from a single measurement point of $x(t)$. Chapter 3 discusses the challenges, current literature and the proposed method of compensating for the frequency dependent effects over wide bandwidths.

2.2 Overview of Digital Predistortion Theory

After the frequency upconversion of the modulated signal to an RF frequency, an output stage consisting of driver amplifiers and a PA stage are required to boost the signal power to an appropriate level for signal transmission over the air. However, the PA is an amplitude

sensitive device, whose gain depends on the input signal near its peak output power. Given constant envelope signals, such as phase or frequency modulated signals, there would be no added distortions from the PA stage. In contrast, the envelopes of spectral efficient signals typically exhibit high PAPRs. For instance, the OFDM signal with a modulation bandwidth of 320 MHz shown in Fig. 2.3(a) exhibits 8.6 dB of PAPR. When PAs are subjected with such signals near their peak efficiency region of operation, they exhibit nonlinear distortions due to the PA's gain dependency on the input power as illustrated in Fig. 2.3(b).

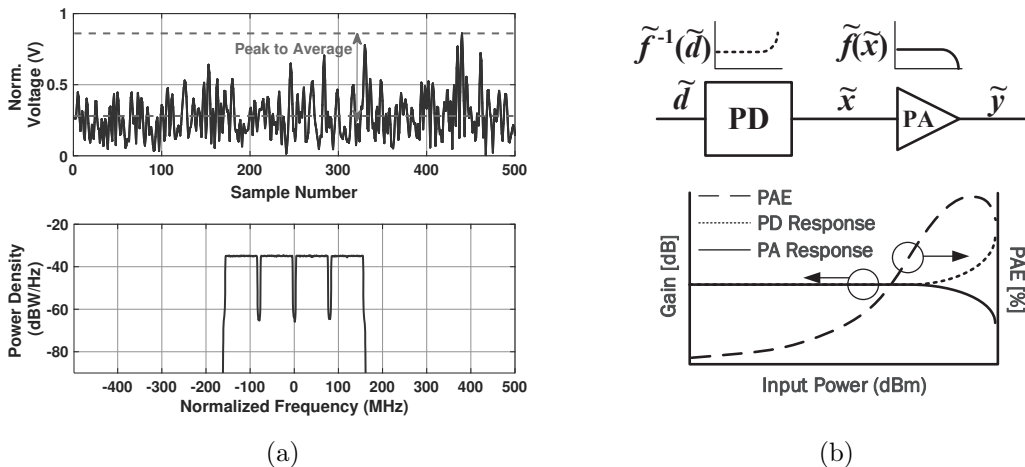


Figure 2.3: Example of (a) the envelope's magnitude and spectrum of an OFDM signal with a 320 MHz modulation bandwidth with a PAPR of 8.6 dB (b) a PA's gain and PAE characteristics versus input power.

To avoid these nonlinear distortions, the PA can be operated in its power back-off region where the gain is constant for low input powers. However the PA's power added efficiency (PAE) given in terms of the PA's input power P_{in} , output power P_{out} and DC power consumption P_{DC} by

$$PAE = \frac{P_{out} - P_{in}}{P_{DC}}$$

decreases at back-off power levels resulting in a degraded overall system efficiency. To mitigate the nonlinear distortions, while maintaining operation in the high efficiency region, linearization techniques such as DPD can be utilized. As illustrated in Fig. 2.3(b),

DPD mitigates the nonlinear distortion by modelling the inverse behaviour of the PA in a predistorter (PD) module. To observe the PA's behaviour, a TOR shown in Fig. 2.4 is required. Due to the bandwidth expansion in the signal when the PA is operated non-linearly, a wideband TOR would be required to capture the PA's output signal. A high speed analog to digital converter (ADC) would be needed in the TOR hardware to capture the desired output signal with an expanded bandwidth resulting in an increased power consumption. Then, the baseband signal processing system uses the observed output data to train and apply the PD to mitigate the nonlinear distortions and compensate for the IQ imbalances present in the system. It is noted that the predistorted signal would also possess an expanded bandwidth and would require IQ imbalance compensation over this expanded bandwidth. In this thesis, the bandwidth of the IQ imbalance compensator is referred to as the total correction bandwidth (TCB).

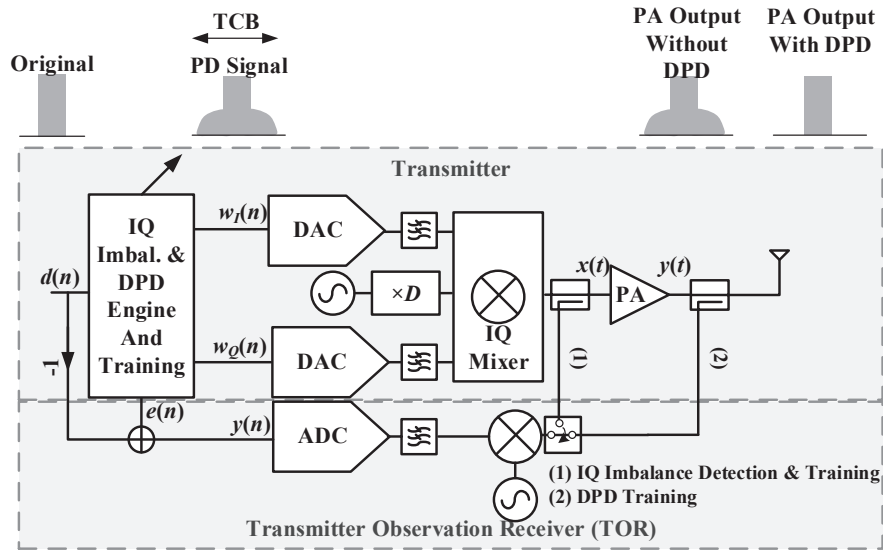


Figure 2.4: TX with a TOR for IQ imbalance detection and DPD training.

When the distortions are static, or the PA is memoryless (ML), then a simple polynomial model for modelling the PA and the PD suffices. Due to the matching networks, dynamic thermal effects and dynamics of the semiconductor device, the PA exhibits linear and nonlinear memory effects, where the PA's current output depends on the past inputs [7]. The static nonlinear distortions and memory attributed distortions created by the PA can be analyzed in terms of the amplitude induced amplitude (AM-AM) distortions

and amplitude induced phase (AM-PM) distortions. An example of the gain and phase distortions curves of a PA, its PD, and the linearized PA are shown in Fig. 2.5. If the PA only exhibited static behaviour, then for every input power there would only be one possible gain and phase distortion value.

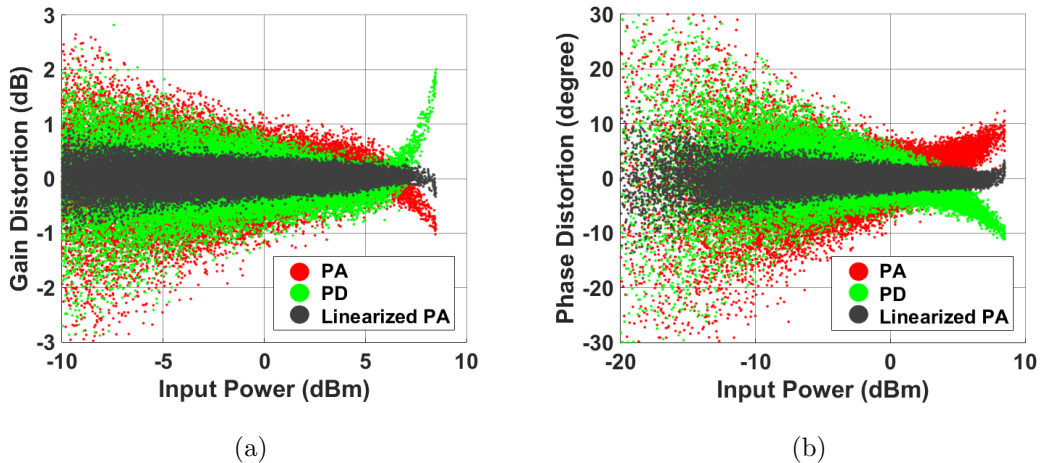


Figure 2.5: Example of gain and phase distortion curves for a PA, its PD, and the resulting linearized PA.

For that reason, there is a requirement for the behavioural models used in modelling PAs and the PD module to be able to handle these memory effects. To handle the nonlinear dynamic behaviour of the PA, Volterra series based models mapped to their CBBEs are used. With these models, the PA's output $\tilde{y}(n)$ can be modelled as a linear combination of basis functions $\tilde{\psi}_i(\tilde{\mathbf{x}}(n))$ through

$$\tilde{y}(n) = \sum_{i=1}^K \tilde{f}(i) \tilde{\psi}_i(\tilde{\mathbf{x}}(n)), \quad (2.4)$$

where $f(i)$ are the model parameters, $\tilde{\mathbf{x}}(n) = [x(n), \dots, x(n - L + 1)]^T$ is a vector of L samples of the PA's input signal and K is the total number of basis functions. The basis functions of (2.4) are chosen to ensure that the observed distortions, i.e. the AM-AM and AM-PM distortions, of the PA are modelled. For instance from the baseband equivalent Volterra series for PAs of [8], the basis functions are given by

$$\tilde{\psi}_i(\tilde{\mathbf{x}}(n)) = \prod_{p_1=1}^{k(i)+1} \tilde{x}(n - m_{p_1}(i)) \prod_{p_2=k(i)+2}^{2k(i)+1} \tilde{x}^*(n - m_{p_2}(i)),$$

where $\{m_{p_1}(i)\}_{p_1=1}^{k(i)+1}$ and $\{m_{p_2}(i)\}_{p_2=k(i)+2}^{2k(i)+1}$ represent the memory lags of the i th basis function, $2k(i) + 1$ is the nonlinearity order of the i th basis function. If the PA exhibited memoryless behaviour, then all of the memory lags are 0, i.e. $m_{p_1}(i) = m_{p_2}(i) = 0$ for any p_1, p_2 and i . Due to the large complexity of applying the Volterra model directly, several approaches have been used to prune the model for more feasible models, such as the dynamic deviation reduction (DDR) Volterra series [9], generalized memory polynomial (GMP) [10], and complexity reduced Volterra (CRV) series [11]. Their adoption for the linearization of mm-wave PAs driven with wideband signals need to be investigated due to the fear of the escalation in the required number of DPD coefficients.

For the identification of the PA model, the input and output relationship in (2.4) can be written concisely in vector notation as

$$\tilde{\mathbf{y}}(n) = \tilde{\boldsymbol{\psi}}^T(\tilde{\mathbf{x}}(n))\tilde{\mathbf{f}}_K. \quad (2.5)$$

where $\tilde{\mathbf{f}}_K = [f(1), \dots, f(K)]^T$ and $\boldsymbol{\psi}(\tilde{\mathbf{x}}(n)) = [\tilde{\psi}_1(\tilde{\mathbf{x}}(n)), \dots, \tilde{\psi}_K(\tilde{\mathbf{x}}(n))]^T$. Given L samples of the PA's observed output from the TOR, we can then write the vector of output samples as a function of the input signal $\tilde{x}(n)$ given by

$$\tilde{\mathbf{y}}(n) = \tilde{\boldsymbol{\Psi}}(\tilde{\mathbf{x}}(n))\tilde{\mathbf{f}}_K, \quad (2.6)$$

where $\tilde{\boldsymbol{\Psi}}(\tilde{\mathbf{x}}(n)) = [\tilde{\boldsymbol{\psi}}(\tilde{\mathbf{x}}(n)), \dots, \tilde{\boldsymbol{\psi}}(\tilde{\mathbf{x}}(n - L + 1))]^T$ and this matrix of basis functions is assumed to have K linearly independent columns. The parameters $f(i)$ of the behavioural model can then be identified through a least squares error (LSE) estimate given by

$$\tilde{\mathbf{f}}_K = \left(\tilde{\boldsymbol{\Psi}}^H(\tilde{\mathbf{x}}(n))\tilde{\boldsymbol{\Psi}}(\tilde{\mathbf{x}}(n)) \right)^{-1} \tilde{\boldsymbol{\Psi}}^H(\tilde{\mathbf{x}}(n))\tilde{\mathbf{y}}(n), \quad (2.7)$$

Alternatively, the parameters can be adaptively identified through LSE identification algorithms, such as Newton's approach or the recursive least squares (RLS) approach.

For the PD to correct for the distortions created by the PA, it is assumed that the inverse of the PA's model has a similar model structure, i.e., a Volterra series based model, for relating the predistorted signal $\tilde{z}(n)$ and the input $\tilde{\mathbf{d}}(n)$ through

$$\tilde{z}(n) = \sum_{i=1}^{K_{\text{PD}}} \tilde{f}_{\text{PD}}(i)\tilde{\psi}_{\text{PD},i}(\tilde{\mathbf{d}}(n)), \quad (2.8)$$

where K_{PD} are the total number of coefficients of the PD, $\tilde{f}_{\text{PD}}(i)$ are the PD's model parameters, and $\tilde{\psi}_{\text{PD},i}(\tilde{\mathbf{d}}(n))$ are the PD's i th basis function.

For the identification of the PD, two approaches are commonly used. In the indirect learning case illustrated in Fig. 2.6(a), the assumption of equivalence between the post-inverse and the pre-inverse of the PA is utilized. As a result, we can form an LSE estimate of the PD's parameters, $\tilde{\mathbf{f}}_{K_{PD}}$, through the post inverse's parameters given by

$$\tilde{\mathbf{f}}_{K_{PD}} = \left(\tilde{\Psi}_{PD}^H(\tilde{\mathbf{y}}(n)) \tilde{\Psi}_{PD}(\tilde{\mathbf{y}}(n)) \right)^{-1} \tilde{\Psi}_{PD}^H(\tilde{\mathbf{y}}(n)) \tilde{\mathbf{x}}(n). \quad (2.9)$$

In the direct learning case illustrated in Fig. 2.6(b), the parameters of the PD module directly are identified by minimizing the LSE, $\tilde{\mathcal{E}}$, between the observed PA output signal $\tilde{y}(n)$ and the desired signal $\tilde{d}(n)$ given by

$$\tilde{\mathcal{E}} = \sum_n \left| \tilde{d}(n) - \tilde{y}(n) \right|^2.$$

The PD's parameters, $\tilde{\mathbf{f}}_{K_{PD}}$, can be estimated using adaptive update algorithms, such as Newton's approach or an RLS method. For instance, [12] derives the update equation for Newton's approach, where the ℓ th iteration's value of the PD's parameters, $\tilde{\mathbf{f}}_{K_{PD},\ell}$, is given by

$$\tilde{\mathbf{f}}_{K_{PD},\ell} = \tilde{\mathbf{f}}_{K_{PD},\ell-1} + \mu \left(\tilde{\Psi}_{PD}^H(\tilde{\mathbf{d}}(n)) \tilde{\Psi}_{PD}(\tilde{\mathbf{d}}(n)) \right)^{-1} \tilde{\Psi}_{PD}^H(\tilde{\mathbf{d}}(n)) \left(\tilde{\mathbf{d}}(n) - \tilde{\mathbf{y}}(n) \right), \quad (2.10)$$

where μ is the learning parameter that is determined based on the convergence criteria and the rate of convergence desired.

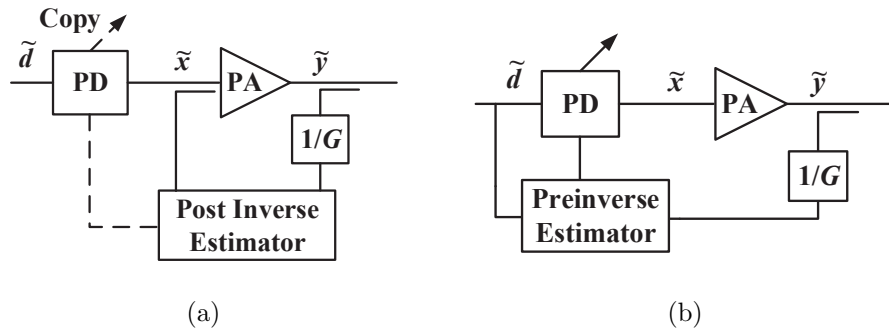


Figure 2.6: Learning architectures to train the predistorter modules: (a) Indirect learning (b) Direct learning.

Chapter 3

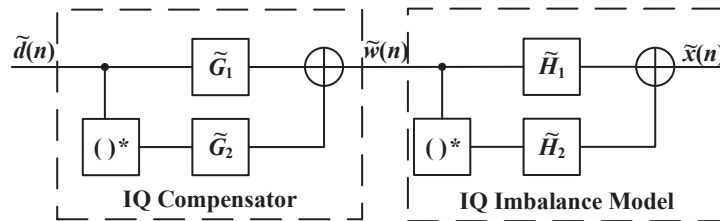
IQ Imbalance Compensation and Digital Predistortion for Millimeter-Wave Signal Generation Using a Reduced Sampling Rate Transmitter Observation Receiver

In this chapter, the proposed IQ imbalance compensation scheme and rearranged Volterra based DPD scheme will be presented. An overview of the literature on the current schemes for IQ imbalance detection and compensation are first presented. Afterwards, the proposed IQ imbalance compensation scheme are introduced. In the test and measurement section, results for validating the proposed IQ imbalance detection and compensation scheme and the devised DPD scheme are described. The work in this chapter is based on the work in [13].

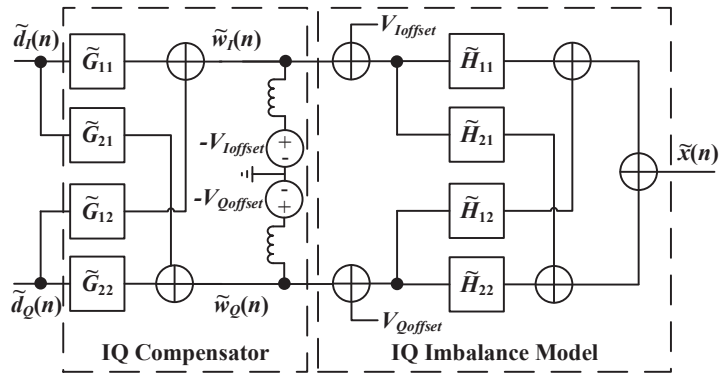
3.1 Literature Review

For third and fourth generation wireless communication infrastructures, signals with modulation bandwidths limited to tens of MHz are used. To mitigate the IQ imbalance effects in these systems, numerous approaches have been proposed in the literature. With narrowband signals, the assumption of frequency independent IQ imbalance effects could be

applied and it led the authors in [14] to analyze the IQ imbalance effects and develop methods to adaptively compensate for them. When signals with wider bandwidths are used, frequency dependent effects start to arise and the authors in [6], [15]–[19] have proposed IQ imbalance detection and compensation methods that are based on using a combination of the following approaches (1) time or frequency domain identification and compensation (2) formulating special test signals, and (3) utilizing either the real-valued or complex valued filter based IQ imbalance models shown in Fig. 3.1.



(a)



(b)

Figure 3.1: IQ imbalance and compensator models using (a) complex valued filters or (b) real valued filters.

These methods include: (a) maximizing the image rejection through estimating the optimal complex valued filter using a statistical compensation method using modulated test signals [15], (b) Swept continuous wave (CW) or multi-tone test signals for incoherent measurement based IQ imbalance detection [16], (c) utilizing multi-tone test signals in a modified steepest descent method for parametric sub-band based IQ imbalance detection and compensation for maximizing image rejection [17], (d) mitigating the IQ imbalance

imbalance through real-valued compensation filters through a LSE method with modulated signals [6], [18], and e) using the pilots of modulated signals for estimating the I and Q path frequency responses separately followed by an online re-calibration method for the time-variant IQ imbalance parameters [19].

Furthermore, there are limiting effects on the DPD linearization capacity due to IQ imbalance effects in direct conversion transmitters [6], [14], [18], [20]. To account for these effects, joint nonlinear IQ imbalance and joint linear IQ imbalance with nonlinear PA compensation schemes have been investigated, which use some form of the model structure shown in Fig. 3.2. [21]–[24]. These schemes include implementing a dual input Volterra series [21], [24], parallel Hammerstein model [22], and pruned Volterra models [23]. These joint compensation schemes typically involve a larger number of basis functions for a given PA, IQ imbalance frequency response, and a set of signal statistics. Due the nature of some of the models, joint IQ imbalance and DPD schemes also involve more sophisticated parameter estimation algorithms compared to those used for separate IQ imbalance compensation and DPD methods.

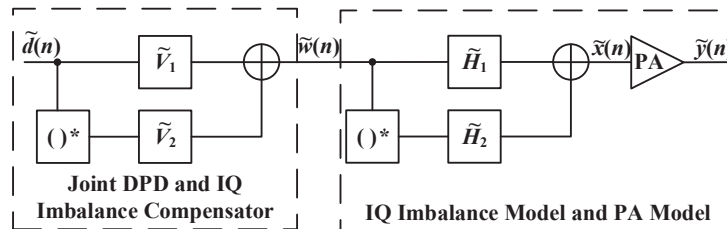


Figure 3.2: Joint IQ imbalance and DPD model structure.

The application of the aforementioned schemes to wideband mm-wave direct conversion TXs generating signals with modulation bandwidths in the hundreds of MHz becomes more challenging due to the exacerbation of the IQ imbalance and PA nonlinear distortions. For example, to detect hardware non-idealities it is necessary to implement a TOR, which generally includes an ADC that should be able to capture the TCB, which is proportional to the modulation bandwidth of the signal. For the targeted wideband signals for the mm-wave frequencies, the power consumption of the TOR would increase and the SFDR of the TOR would worsen.

To address these issues with wideband mm-wave direct conversion TXs, this thesis separates the IQ imbalance and PA nonlinearity compensation schemes. For the IQ imbalance detection and compensation method, an interleaved multi-tone test signal for a frequency

domain based IQ imbalance detection and compensation method utilizing a sub-Nyquist TOR is proposed. Afterwards to handle the nonlinear distortions presented by mm-wave PAs driven by wideband modulated signals, the CRV model in [11] is rearranged to enable a low complexity pruned Volterra based DPD scheme.

3.2 Wideband IQ Imbalance Detection and Compensation Scheme

3.2.1 Proposed IQ Imbalance Detection and Compensation

In this thesis, the frequency dependent IQ imbalance model response of the direct upconversion architecture in Fig. 2.1 are modelled using the real-valued filter model network shown in Fig. 3.1(b) [6], [18]. In the following frequency domain approach, the filter responses for a discrete set of frequencies are estimated and stored in a look-up-table (LUT). By using the real-valued filter model, it enables the use of the conjugate symmetry property of the frequency responses and this reduces the number of LUT entries in half.

To be able to separate the frequency responses imbalance causing the Q tones to leak into the I tones and vice versa, the orthogonality property between the signal's I and Q components can be used. This enables the design of a test signal whose I and Q frequency components can be separated in the frequency domain. This leads to the proposed offline IQ imbalance detection method that relies on constructing an interleaved multi-tone test signal consisting of an I signal, $\tilde{w}_I(n)$, whose frequency components do not lie on the same frequency grid as the Q signal, $\tilde{w}_Q(n)$. These two signals are described by

$$\tilde{w}_I(n) = \sum_{r=0}^{N_I-1} \cos \left(\underbrace{2\pi \frac{f_0 + r\Delta f + f_{\text{offset}}}{F_s} n + \phi_r}_{\omega_{I,r}} \right), \quad (3.1)$$

$$\tilde{w}_Q(n) = \sum_{r=0}^{N_Q-1} \cos \left(\underbrace{2\pi \frac{f_0 + r\Delta f}{F_s} n + \phi_r}_{\omega_{Q,r}} \right), \quad (3.2)$$

where N_I and N_Q are the number of tones, f_0 is the initial frequency, ϕ_r is a set of phases chosen to control the PAPR of the test signal, Δf is the tone spacing, f_{offset} is

the frequency grid offset between the $\tilde{w}_I(n)$ and $\tilde{w}_Q(n)$ signals, and F_s is the sampling rate of the baseband system. ω_I and ω_Q denote the frequency grid of the I and Q tones, respectively. The process in which the interleaved multi-tone test signal passes through the filter network is illustrated in Fig. 3.3. When IQ imbalance is present in the system, the I and Q frequency grids will become interleaved in the I and Q part of the output signal. If there was no imbalance present in the system, then the cross filter terms $\tilde{H}_{12}(e^{j\omega})$ and $\tilde{H}_{21}(e^{j\omega})$ would be 0 and the I and Q components of the output signal $\tilde{x}(n)$ would only contain their original frequency components but filtered by $\tilde{H}_{11}(e^{j\omega})$ and $\tilde{H}_{22}(e^{j\omega})$.

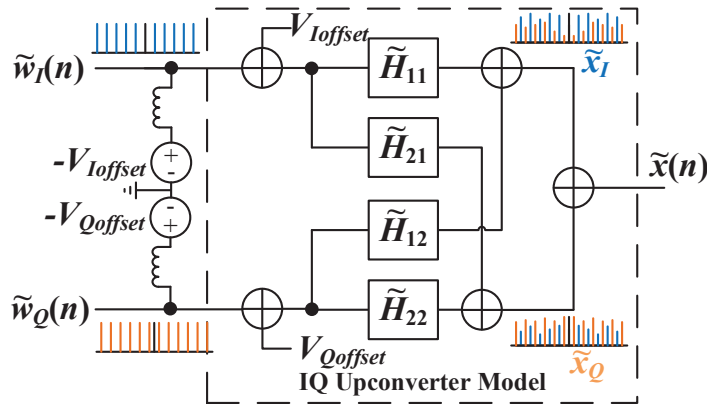


Figure 3.3: Effects of the IQ imbalance on the interleaved multi-tone test signal on the interleaved multi-tones.

For the test signal's settings, the number of tones N_I and N_Q are chosen based on the TCB desired. To ensure that the interpolation between the LUT entries accurately models the IQ imbalance frequency response, the tone spacing Δf is chosen appropriately. The frequency grid offset, f_{offset} , is set to ensure that the $\tilde{w}_I(n)$ and $\tilde{w}_Q(n)$ frequency components do not lie on top of each other's components. For example, the frequency offset can be set to $f_{offset} = \Delta f/2$. To control the PAPR of the signal, the random phases ϕ_r can be set in two manners. If a small PAPR is desired, then one can use the phase function described by

$$\phi_r = \frac{\pi r}{2N} (r - 3) \quad (3.3)$$

to minimize the PAPR for the case where $\phi_r \in [0, \pi]$ and N is the total number of tones in the multi-tone [25], [26]. If a larger PAPR is desired, then the phases could be distributed

according to a Gaussian distribution, i.e. $\phi_r \sim \mathcal{N}(0, \sigma_\phi^2)$, where σ_ϕ^2 is set to achieve a certain PAPR. To minimize the LO feedthrough to the RF port from the IQ mixer, the DC offsets, $V_{I,\text{offset}}$, and $V_{Q,\text{offset}}$ found through a gradient descent search are injected into the I and Q paths as shown in Fig. 3.3.

The interleaved multi-tone test signal has several advantages over the swept CW test signal and the modulated test signals. First, the proposed test signal enables faster detection compared to a swept CW based methods and secondly, the IQ imbalance detection using the interleaved multi-tone test signal is less sensitive to measurement noise compared to modulated signals based methods. This is because of the periodic property of the multi-tone test signal where the average power distributed over a discrete number of frequencies as opposed to non-periodic modulated signals where the average power of the signal is distributed over a continuous range of frequencies. As a result, generating a multi-tone signal always results in a higher SFDR compared to generating a non-periodic modulated signal with a continuous spectrum. All of IQ imbalance compensation filters can be identified in the time domain method or in the proposed frequency domain method using the proposed interleaved multi-tone test signal.

In the time domain, we would have $L + 1$ measurement data points of the input signal $\tilde{\mathbf{w}} = [\tilde{w}(0), \dots, \tilde{w}(L - 1)]^T$, where $\tilde{w}(n) = \tilde{w}_I(n) + j\tilde{w}_Q(n)$ and the output signal $\tilde{\mathbf{x}} = [\tilde{x}(0), \dots, \tilde{x}(L - 1)]^T$, where $\tilde{x}(n) = \tilde{x}_I(n) + j\tilde{x}_Q(n)$. The output signal is related to the input test signal $\tilde{w}(n)$ and the four IQ imbalance compensation FIR filters, $\tilde{g}_{11}(n)$, $\tilde{g}_{12}(n)$, $\tilde{g}_{21}(n)$, $\tilde{g}_{22}(n)$, of order M by

$$\begin{aligned} \tilde{w}(n) = & \sum_{i=0}^M \tilde{g}_{11}(i)\tilde{x}_I(n-i) + \sum_{i=0}^M \tilde{g}_{12}(i)\tilde{x}_Q(n-i) \\ & + j \left(\sum_{i=0}^M \tilde{g}_{22}(i)\tilde{x}_Q(n-i) + \sum_{i=0}^M \tilde{g}_{21}(i)\tilde{x}_I(n-i) \right). \end{aligned} \quad (3.4)$$

The relationship in (3.4) can be written succinctly in vector notation as

$$\begin{aligned} \tilde{w}(n) = & \tilde{\mathbf{x}}_I^T(n)\tilde{\mathbf{g}}_{11} + j\tilde{\mathbf{x}}_I^T(n)\tilde{\mathbf{g}}_{21} + \tilde{\mathbf{x}}_Q^T(n)\tilde{\mathbf{g}}_{21} + j\tilde{\mathbf{x}}_Q^T(n)\tilde{\mathbf{g}}_{22} \\ = & \tilde{\mathbf{x}}_I^T(n) (\tilde{\mathbf{g}}_{11} + j\tilde{\mathbf{g}}_{21}) + \tilde{\mathbf{x}}_Q^T(n) (\tilde{\mathbf{g}}_{21} + j\tilde{\mathbf{g}}_{22}), \end{aligned}$$

where $\tilde{\mathbf{x}}_I(n) = [\tilde{x}_I(n), \dots, \tilde{x}_I(n - M + 1)]^T$, $\tilde{\mathbf{x}}_Q(n) = [\tilde{x}_Q(n), \dots, \tilde{x}_Q(n - M + 1)]^T$, and $\tilde{\mathbf{g}}_{ij} = [\tilde{g}_{ij}(0), \dots, \tilde{g}_{ij}(M - 1)]^T$. Under the assumption that the columns of the matrix $\tilde{\mathbf{X}}$ are linearly independent, the LSE estimate of the four compensation FIR filters [18] can

be formulated through

$$\begin{aligned} \tilde{w}_{M-1}^{M+L-2} &= \underbrace{\begin{bmatrix} \tilde{\mathbf{X}}_I & \tilde{\mathbf{X}}_Q \end{bmatrix}}_{\tilde{\mathbf{X}}} \begin{bmatrix} \tilde{\mathbf{g}}_{11} + j\tilde{\mathbf{g}}_{21} \\ \tilde{\mathbf{g}}_{12} + j\tilde{\mathbf{g}}_{22} \end{bmatrix} \\ \begin{bmatrix} \tilde{\mathbf{g}}_{11} + j\tilde{\mathbf{g}}_{21} \\ \tilde{\mathbf{g}}_{12} + j\tilde{\mathbf{g}}_{22} \end{bmatrix} &= (\tilde{\mathbf{X}}^H \tilde{\mathbf{X}})^{-1} \tilde{\mathbf{X}}^H \tilde{\mathbf{w}}, \end{aligned} \quad (3.5)$$

where

$$\begin{aligned} \tilde{\mathbf{X}}_I &= [\tilde{\mathbf{x}}_I(M-1), \dots, \tilde{\mathbf{x}}_I(M+L-2)]^T, \\ \tilde{\mathbf{X}}_Q &= [\tilde{\mathbf{x}}_Q(M-1), \dots, \tilde{\mathbf{x}}_Q(M+L-2)]^T. \end{aligned}$$

The four compensation filters are then applied to the desired signal $\tilde{\mathbf{d}}(n)$ through

$$\tilde{w}_{M-1}^{M+L-2} = \underbrace{\begin{bmatrix} \tilde{\mathbf{D}}_I & \tilde{\mathbf{D}}_Q \end{bmatrix}}_{\tilde{\mathbf{D}}} \begin{bmatrix} \tilde{\mathbf{g}}_{11} + j\tilde{\mathbf{g}}_{21} \\ \tilde{\mathbf{g}}_{12} + j\tilde{\mathbf{g}}_{22} \end{bmatrix}, \quad (3.6)$$

where

$$\begin{aligned} \tilde{\mathbf{D}}_I &= [\tilde{\mathbf{d}}_I(M-1), \dots, \tilde{\mathbf{d}}_I(M+L-2)]^T, \\ \tilde{\mathbf{D}}_Q &= [\tilde{\mathbf{d}}_Q(M-1), \dots, \tilde{\mathbf{d}}_Q(M+L-2)]^T. \end{aligned}$$

A disadvantage of the time domain approach is that it requires a pseudo-inverse operation of the block convolution matrix $\tilde{\mathbf{X}}$. This matrix can be ill-conditioned without regularization resulting in model accuracy degradation. In terms of the computational complexity, the LSE solution requires $\mathcal{O}(4LM^2)$ operations for the pseudo inverse and the compensation computational complexity is on the order of $\mathcal{O}(LM)$. The time domain method also does not take full advantage of the interleaved property of the multi-tone test signal proposed here.

In the proposed frequency domain based IQ imbalance detection and compensation method, the IQ imbalance frequency domain model relates the interleaved multi-tone test signals $\tilde{W}_I(e^{j\omega})$ and $\tilde{W}_Q(e^{j\omega})$ to the output signals, $\tilde{X}_I(e^{j\omega})$ and $\tilde{X}_Q(e^{j\omega})$ through

$$\begin{bmatrix} \tilde{X}_I(e^{j\omega}) \\ \tilde{X}_Q(e^{j\omega}) \end{bmatrix} = \underbrace{\begin{bmatrix} \tilde{H}_{11}(e^{j\omega}) & \tilde{H}_{12}(e^{j\omega}) \\ \tilde{H}_{21}(e^{j\omega}) & \tilde{H}_{22}(e^{j\omega}) \end{bmatrix}}_{\tilde{\mathbf{H}}(e^{j\omega})} \begin{bmatrix} \tilde{W}_I(e^{j\omega}) \\ \tilde{W}_Q(e^{j\omega}) \end{bmatrix}, \quad (3.7)$$

where $\omega = 2\pi f/F_s$ and F_s is the complex baseband sampling rate.

Any IQ imbalance causes the tones to appear in the other's frequency grid as shown in Fig. 3.3. Due to the interleaved frequency grid of the original I and Q signals, the test signal enables the forward model extraction of $\tilde{H}_{11}(e^{j\omega})$, $\tilde{H}_{12}(e^{j\omega})$, $\tilde{H}_{21}(e^{j\omega})$, and $\tilde{H}_{22}(e^{j\omega})$ in a single step compared to the swept CW method. This also allows for the simultaneous estimation of the relative delay between the I and Q paths.

The frequency domain forward model extraction of the four filters is done using the IQ modulators output signal $\tilde{X}_I(e^{j\omega})$ and $\tilde{X}_Q(e^{j\omega})$ and its input signals $\tilde{W}_I(e^{j\omega_I})$ and $\tilde{W}_Q(e^{j\omega_Q})$. For instance, the forward model $\tilde{H}_{11}(e^{j\omega_I})$ is identified by computing the transfer function relating the input tones on the ω_I frequency grid, $\tilde{W}_I(e^{j\omega_I})$, and the tones on the ω_I frequency grid in the output signal $\tilde{X}_I(e^{j\omega})$ through

$$\tilde{H}_{11}(e^{j\omega_I}) = \frac{\tilde{X}_I(e^{j\omega_I})}{\tilde{W}_I(e^{j\omega_I})}. \quad (3.8)$$

Additionally, the IQ imbalance filter $\tilde{H}_{12}(e^{j\omega_Q})$ causing the leakage of the Q tones into the I component of the output, $\tilde{X}_I(e^{j\omega})$ is computed through

$$\tilde{H}_{12}(e^{j\omega_Q}) = \frac{\tilde{X}_I(e^{j\omega_Q})}{\tilde{W}_Q(e^{j\omega_Q})}, \quad (3.9)$$

using the input tones on the ω_Q frequency grid, $\tilde{W}_Q(e^{j\omega_Q})$, and the tones lying on the ω_Q frequency grid in the output signal $\tilde{X}_I(e^{j\omega})$.

Similarly using the output signal $\tilde{X}_Q(e^{j\omega})$ and the input signals $\tilde{W}_Q(e^{j\omega_Q})$ and $\tilde{W}_I(e^{j\omega_I})$, the forward models $\tilde{H}_{22}(e^{j\omega_Q})$ and $\tilde{H}_{21}(e^{j\omega_I})$ are extracted through

$$\tilde{H}_{21}(e^{j\omega_I}) = \frac{\tilde{X}_Q(e^{j\omega_I})}{\tilde{W}_I(e^{j\omega_I})}, \quad (3.10)$$

$$\tilde{H}_{22}(e^{j\omega_Q}) = \frac{\tilde{X}_Q(e^{j\omega_Q})}{\tilde{W}_Q(e^{j\omega_Q})}. \quad (3.11)$$

In constructing the four forward models, it is noted that the conjugate symmetry property of the filters is exploited to deduce the values of the filters for the negative frequencies, i.e. $\tilde{\mathbf{H}}(e^{-j\omega}) = \tilde{\mathbf{H}}^*(e^{j\omega})$.

After constructing the four forward models, the frequency grids between the filters need to be aligned because of the frequency grid offset f_{offset} between the I and Q frequency grids.

A cubic spline interpolator is used to align the LUTs with a wider frequency span on to the smaller frequency grid. For example when $N_I > N_Q$, $\tilde{H}_{21}(e^{j\omega_I})$ and $\tilde{H}_{11}(e^{j\omega_I})$ are interpolated on to the ω_Q frequency grid resulting in the LUTs with the same look up ω_Q frequency grid. From the estimated forward model $\tilde{\mathbf{H}}(e^{j\omega})$, the IQ imbalance compensation model $\tilde{\mathbf{G}}(e^{j\omega})$ composed of $\tilde{G}_{11}(e^{j\omega})$, $\tilde{G}_{12}(e^{j\omega})$, $\tilde{G}_{21}(e^{j\omega})$, $\tilde{G}_{22}(e^{j\omega})$ is constructed using

$$\tilde{\mathbf{G}}(e^{j\omega}) = \begin{bmatrix} \tilde{H}_{11}(e^{j\omega}) & \tilde{H}_{12}(e^{j\omega}) \\ \tilde{H}_{21}(e^{j\omega}) & \tilde{H}_{22}(e^{j\omega}) \end{bmatrix}^{-1}. \quad (3.12)$$

To apply the four IQ compensation filters in $\tilde{\mathbf{G}}(e^{j\omega})$, the compensation filter values are interpolated across the normalized frequency grid ω using the cubic spline interpolator. Afterwards, the compensated $\tilde{W}_I(e^{j\omega})$ and $\tilde{W}_Q(e^{j\omega})$ baseband signals are computed for each frequency bin using

$$\begin{bmatrix} \tilde{W}_I(e^{j\omega}) \\ \tilde{W}_Q(e^{j\omega}) \end{bmatrix} = \begin{bmatrix} \tilde{G}_{11}(e^{j\omega}) & \tilde{G}_{12}(e^{j\omega}) \\ \tilde{G}_{21}(e^{j\omega}) & \tilde{G}_{22}(e^{j\omega}) \end{bmatrix} \begin{bmatrix} \tilde{D}_I(e^{j\omega}) \\ \tilde{D}_Q(e^{j\omega}) \end{bmatrix}. \quad (3.13)$$

Again, the conjugate symmetry property of the filters can be exploited to find the values of the filters for the negative frequencies, i.e. $\tilde{\mathbf{G}}(e^{-j\omega}) = \tilde{\mathbf{G}}^*(e^{j\omega})$. Lastly, the IQ imbalance compensated signal $\tilde{W}(e^{j\omega})$ is transformed back to the time domain.

In terms of the frequency domain's computational complexity, the identification of $\tilde{\mathbf{H}}(e^{j\omega})$ requires $\mathcal{O}(L \log L + N_Q + N_I)$ operations when using the conjugate symmetry property of the real-valued filters. For the identification of $\tilde{\mathbf{G}}(e^{j\omega})$, the computational complexity is on the order of $\mathcal{O}(N_Q + N_I)$ operations. To compare the time domain and frequency domain we compare the case where the LUT have the same number of entries as the order of the time domain FIR filters, i.e. $M = N_I = N_Q$. In this case, the proposed frequency domain method's computational complexity is on the order of $\mathcal{O}(L \log L + M)$ compared to the time domain method's computational complexity order of $\mathcal{O}(LM^2 + L^3)$. For applying the compensation scheme the computational complexity of the frequency domain method on the order of $\mathcal{O}(L \log L)$ compared to the time domain method's $\mathcal{O}(LM)$. This computational complexity comparison is summarized through Fig. 3.4, which shows that for an increasing M , the computational complexity of the proposed frequency domain method's does not grow as quickly when compared to the time domain method.

3.2.2 IQ Imbalance Detection With a Sub-Nyquist Rate Transmitter Observation Receiver

As the modulation bandwidth of the signal increases, the TCB increases proportionally resulting in large IQ imbalance detection capability requirement for the TOR. In this

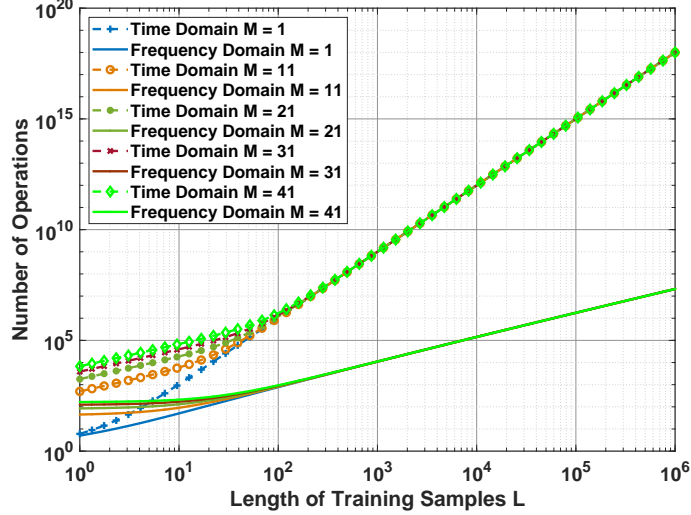


Figure 3.4: Computational complexity comparison for IQ imbalance detection and compensation of the time domain and proposed frequency domain method.

section, the method to engineer the structure of the proposed interleaved multi-tone test signal to reduce the required TOR sampling rate for IQ imbalance detection is introduced. In the proposed multi-tone test signal, the parameters that affect the frequency spacing of the tones at the TX input are Δf , and f_{offset} . First consider a TX output signal $\tilde{x}(n)$ with a bandwidth equal to the TCB requiring a Nyquist rate of $F_s \geq 2\text{TCB}$. The sub-Nyquist rate TOR with a downsampling factor of D , downsamples $\tilde{x}(n)$ to a rate of F_s/D to create a sub-Nyquist rate sampled sequence $\tilde{x}(Dn)$. If Δf and f_{offset} of the multi-tone test signal are not chosen correctly then using the sub-Nyquist sampling TOR will cause undesired overlapping from the aliased tones as shown in Fig. 3.5. The boundary, $F_s/2D$, between the 1st Nyquist zone, $p = 1$ and the 2nd Nyquist zone $p = 2$, lies directly in the middle of an I and Q tone causing the 2nd Nyquist zone image to fold into the 1st Nyquist zone.

To avoid this issue, frequency offsets can be introduced into the multi-tone test signal. Let the frequency components of the test signal be designated with $f_j, f_k \in \{\mathcal{F}_I \cup \mathcal{F}_Q\}$ where \mathcal{F}_I is the set of all tones in the I signal $\tilde{w}_I(t)$ and \mathcal{F}_Q is the set of all frequency components in the Q signal $\tilde{w}_Q(t)$. For the aliased tones to not overlap with the first Nyquist zone tones, the condition described by

$$f_j \neq \left| \frac{(p-1)F_s}{D} - f_k \right| ; j < k \quad (3.14)$$

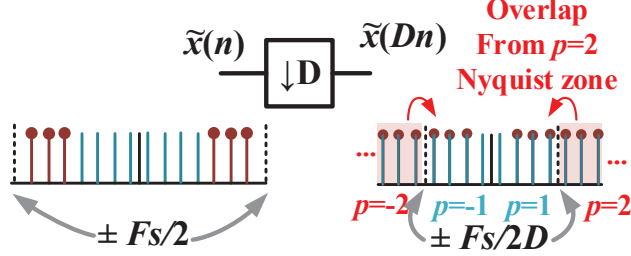


Figure 3.5: Without careful construction of the proposed interleaved multi-tone test signal, aliased tones from the 2nd Nyquist zone ($p = 2$) overlap with the non-aliased tones in the reduced sampling rate TOR.

should be satisfied where F_s is the Nyquist sampling rate of $F_s = 2\text{TCB}$.

To satisfy this condition, frequency offsets $f_{\text{offset},u}$ are introduced into the multi-tone signal near the beginning of the p -th Nyquist zone. The tones f'_k in the p -th Nyquist zone are now offset by $f_{\text{offset},u}$, and are described by

$$f'_k = f_k + f_{\text{offset},u} \quad (3.15)$$

where $\frac{(p-1)F_s}{2D} < f_k < \frac{pF_s}{2D}$, and p is a positive integer. The frequency offsets, $f_{\text{offset},u}$, also need to satisfy

$$f_{\text{offset},u} \neq \Delta f - f_{\text{offset},v} ; u \neq v. \quad (3.16)$$

This prevents overlapping from the aliased tones due to the symmetric folding around the edge of the p -th Nyquist zone, and folding from the other aliased tones from other Nyquist zones.

For instance to avoid aliasing in the prior example, a frequency offset $f_{\text{offset},1}$ is added to the tone closest to the right side of the $F_s/2D$ edge, as shown in Fig. 3.6(a). When the signal is sub-sampled and the 2nd Nyquist zone's image folds into the 1st Nyquist zone, the aliased tones do not overlap. Furthermore, a different case is shown in Fig. 3.6(b), where there are two offsets $\{f_{\text{offset},1}, f_{\text{offset},2}\}$ in the test signal to prevent the aliases from the $p = 2$ and $p = 3$ Nyquist zones near the frequencies $f = F_s/2D$ and $f = F_s$ from folding on to each other when they are sampled by the sub-sampling TOR.

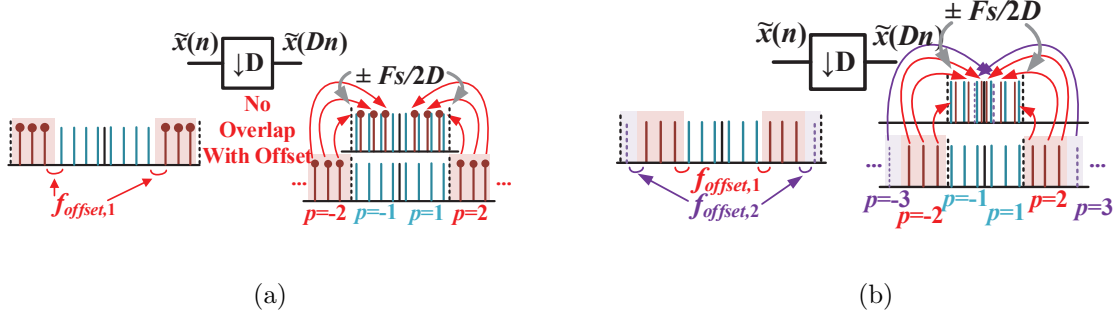


Figure 3.6: (a) Setting the frequency offset in the proposed interleaved multi-tone test signal avoids overlap from aliasing allowing for estimation of the Nyquist rate sampled output. (b) Increasing the sub-sampling ratio requires more frequency offsets to be introduced into the multi-tone structure to avoid overlap from the aliasing. In this case, 2 offsets are introduced to prevent overlap from the 2nd and 3rd Nyquist zones where $p = 2$, and $p = 3$, respectively.

As a numerical example, consider a complex interleaved multi-tone signal with tones starting at a frequency of 2 MHz, have a tone spacing of $\Delta f = 10$ MHz, and a modulation bandwidth of 600 MHz. If $\tilde{x}(n)$ is detected with a TOR operating at 500 MS/s, then near the end of the first Nyquist zone, a frequency offset of 21 MHz is introduced into the I and Q multi-tone signals. This places the tone after 242 MHz tone at 253 MHz so that in the reduced sampling rate TOR case, the alias folds back at 247 MHz instead of overlapping with the 242 MHz tone.

For the estimate of the Nyquist rate (NR) sampled TX output multi-tone signal $\tilde{x}(n)$ from the sub NR sampled signal $\tilde{x}(Dn)$, the proposed method occurs in the frequency domain as illustrated in Fig. 3.7. The desired NR sampled output signal is denoted by $\tilde{X}_{NR}(e^{j\omega})$. At the sub-sampling rate of F_s/D , the non-aliased tones in the ± 1 st Nyquist zone are denoted as $\tilde{X}_{\pm 1}(e^{j\omega_{\pm 1}})$, aliased tones from the p -th Nyquist zone denoted as $\tilde{X}_p(e^{j\omega_p})$, and ω_p represents the frequency grid of the p -th Nyquist zone. The NR sampled signal $\tilde{X}_{NR}(e^{j\omega})$ is sectioned into the p -th Nyquist zone at the sampling rate F_s/D as shown in Fig. 3.6(b) and is given by

$$\tilde{X}_{NR}(e^{j\omega}) = \sum_{\substack{i=-p \\ i \neq 0}}^p \tilde{X}_i(e^{j\omega_i}). \quad (3.17)$$

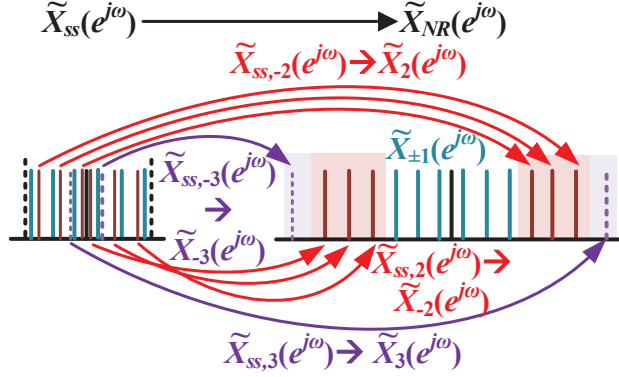


Figure 3.7: Reconstructing the NR signal from the sub-sampled signal.

When the sub-sampling TOR samples the output $\tilde{x}(n)$ at F_s/D , we receive the sub-sampled signal $\tilde{X}_{SS}(e^{j\omega})$. This is expressed as

$$\begin{aligned} \tilde{X}_{SS}(e^{j\omega}) &= \sum_{\substack{i=-p \\ i \text{ even}}}^p \tilde{X}_i \left(e^{j(-1)^{\frac{i}{2}} \omega_i} \right) e^{j \left(\frac{(-1)^{\frac{i}{2}+1} i}{2D} \omega_{F_s} \right)} \\ &+ \sum_{\substack{i=-p \\ i \text{ odd}}}^{-1} \tilde{X}_i \left(e^{j(-1)^{\frac{i+1}{2}} \omega_i} \right) e^{j \left(\frac{(-1)^{\frac{i-1}{2}} (i+1)}{2D} \omega_{F_s} \right)} + \sum_{\substack{i=1 \\ i \text{ odd}}}^p \tilde{X}_i \left(e^{j(-1)^{\frac{i-1}{2}} \omega_i} \right) e^{j \left(\frac{(-1)^{\frac{i+1}{2}} (i-1)}{2D} \omega_{F_s} \right)}, \end{aligned} \quad (3.18)$$

where we describe the sub-sampled signal as the sum of the tones in the aliased p Nyquist zones, and the tones in the ± 1 st Nyquist zone where $\omega_{F_s} = 2\pi$.

Since the frequency offsets introduced into the test-signal to prevent overlapping during the aliasing process, the original p -th Nyquist zone of the aliased tones are known and can be denoted by $\tilde{X}_{SS,p}(e^{j\omega_{SS,p}})$ where $\omega_{SS,p}$ denotes of the frequency grid of the aliased p -th Nyquist zone. Using the sub-sampled multi-tone signal, an estimate of the NR multi-tone signal, $\hat{\tilde{X}}_{NR}(e^{j\omega})$, can be reconstructed by applying frequency translations to the

sub-sampled signal in (3.18) as shown in Fig. 3.7 and described by

$$\begin{aligned} \hat{X}_{\text{NR}}(e^{j\omega}) = & \sum_{\substack{i=-p \\ i \text{ even}}}^p \tilde{X}_{\text{SS},i} \left(e^{j(-1)^{\frac{i}{2}+1}\omega_{\text{SS},i}} \right) e^{j(\frac{-i}{2D}\omega_{F_s})} \\ & + \sum_{\substack{i=-p \\ i \text{ odd}}}^{-1} \tilde{X}_{\text{SS},i} \left(e^{j(-1)^{\frac{i+1}{2}}\omega_{\text{SS},i}} \right) e^{j(\frac{i+1}{2D}\omega_{F_s})} + \sum_{\substack{i=1 \\ i \text{ odd}}}^p \tilde{X}_{\text{SS},i} \left(e^{j(-1)^{\frac{i-1}{2}}\omega_{\text{SS},i}} \right) e^{j(\frac{i-1}{2D}\omega_{F_s})}. \end{aligned} \quad (3.19)$$

With the estimated NR output signal of the direct conversion transmitter, the detection of the IQ imbalance and construction of the IQ imbalance compensators can be done using the proposed frequency domain method. When the sub-Nyquist rate TOR maintains an SFDR level similar to the SFDR of the NR TOR, then with the same number of samples captured, the IQ imbalance detection and compensation method can be performed. Furthermore, the frequency grid resolution of a signal with a NR of F_s , sub-sampling ratio of D , and L samples is $f_{\text{res}} = \frac{F_s}{DL}$. So as D increases, the resolution becomes finer. However the IQ imbalance detection time for the sub-Nyquist TOR increases by the sub-sampling ratio of D in order to capture the same number of samples.

3.3 Test and Measurement Results

3.3.1 Test and Measurement Setup

The test setup shown in Fig. 3.8 was used to validate the proposed IQ imbalance detection and compensation method for mm-wave direct conversion TXs generating wide-band signals. The vector signal generator (VSG) portion of the system consists of the Keysight M8190A arbitrary waveform generator (AWG) to generate the baseband signals, MLIQ-1845 IQ mixer to upconvert the signal to the RF frequency of 30 GHz, and MAAM-011109 and HMC-1132 amplifiers as drivers for the PA stage. The PA used in the setup is the HMC-1131, which has an output 1 dB compression point of 23 dBm. To capture the signal, the TOR is composed of a MM1-1140HS mixer to downconvert the signal to an IF of 2.2 GHz, and the 8-bit 13 GHz bandwidth 40 GS/s Keysight DSA91304A high speed oscilloscope to digitize the signal for IQ imbalance detection, DPD training and signal analysis. The Keysight N5183B MXG signal generator sources are used to provide an LO signal to the mixers. To validate the reduced sampling rate observations, the received data from the oscilloscope are downsampled to the desired sampling rate for signal analysis.

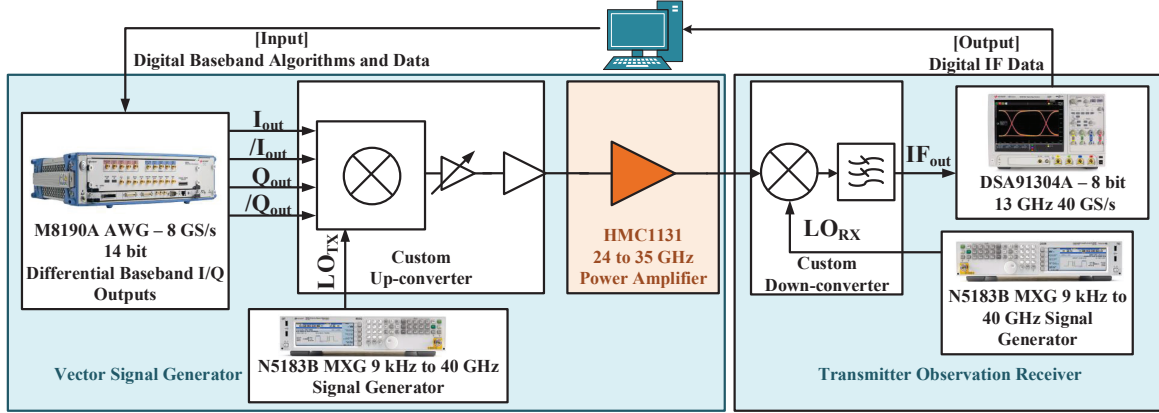


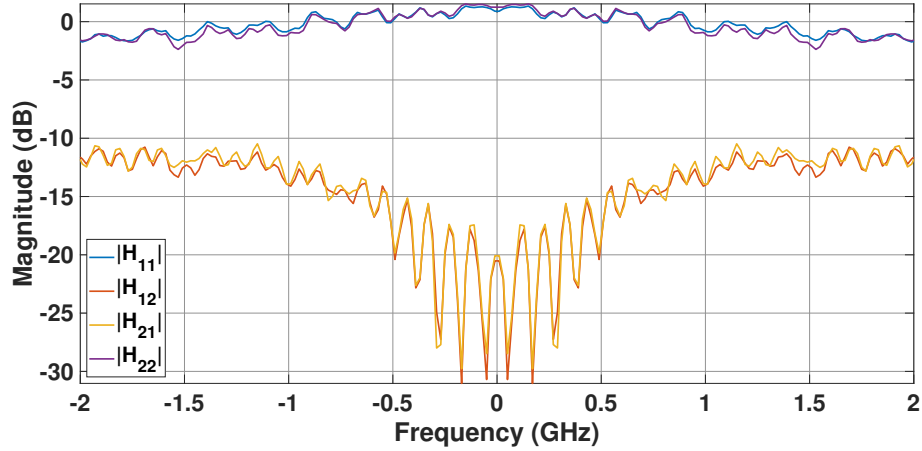
Figure 3.8: mm-wave test and measurement setup to validate the proposed IQ imbalance detection and compensation scheme [27]–[29].

Before performing the following measurements, the TOR’s frequency response was extracted at the NR using a known reference source, Keysight U9391G comb generator, directly connected to the input of the TOR. As the focus of this work is on the IQ imbalance compensation and DPD with a reduced sampling rate TOR, the TOR’s frequency response was extracted at the NR and applied at the NR prior to sub-sampling. However to extract the TOR’s response using a reduced sampling rate, the work in [30] focusing on receiver calibration using a reduced sampling rate for DPD systems can be applied.

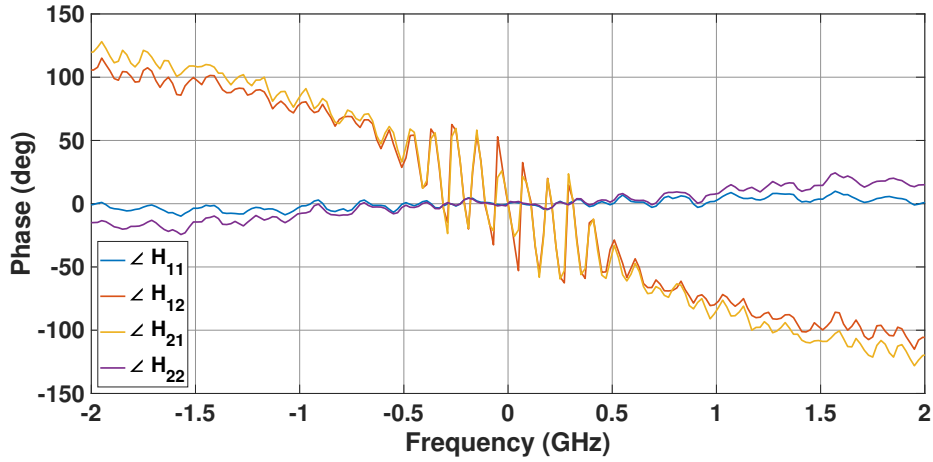
3.3.2 Ultra-wideband IQ Imbalance Compensation Results

In the process of detecting the IQ imbalance present in the VSG and compensating for its effects, the PA is bypassed. For the validation of the proposed method at the NR, an interleaved multi-tone test signal with 4 GHz of modulation bandwidth and a 10.8 dB PAPR is used. The test signals settings are as follows: $f_0 = 10$ MHz, $\Delta f = 20$ MHz, $f_{\text{offset}} = 10$ MHz, and $F_s = 8$ GS/s. With these test signal settings, $\tilde{w}_I(n)$ contains tones starting at 20 MHz and $\tilde{w}_Q(n)$ contains tones that start at 10 MHz. Using the methods discussed in Section 3.2 the four IQ imbalance frequency responses can be extracted utilizing the time domain FIR approach and the frequency domain LUT method. The resulting forward models of the IQ imbalance frequency responses are shown in Fig. 3.9. It is found that over a large bandwidth spanning multi-GHz, the IQ imbalance effects are non-negligible even though the fractional bandwidth at the RF center frequency of 30 GHz is small. This

indicates that the IQ imbalance effects may predominantly take place at the baseband frequencies resulting in the non-negligible distortions present at the RF.



(a)



(b)

Figure 3.9: Measured IQ imbalance filter frequency responses of the direct conversion signal generation system at 30 GHz across 4 GHz: (a) magnitude response, (b) phase response.

After applying the IQ imbalance compensation filters, Table 3.1 summarizes the results when the identified compensation filters are applied to a 4 GHz multi-tone signal with a different set of phases compared to that of the original training signal and an OFDM validation signals with a modulation bandwidth of 800 MHz. In order to achieve the same

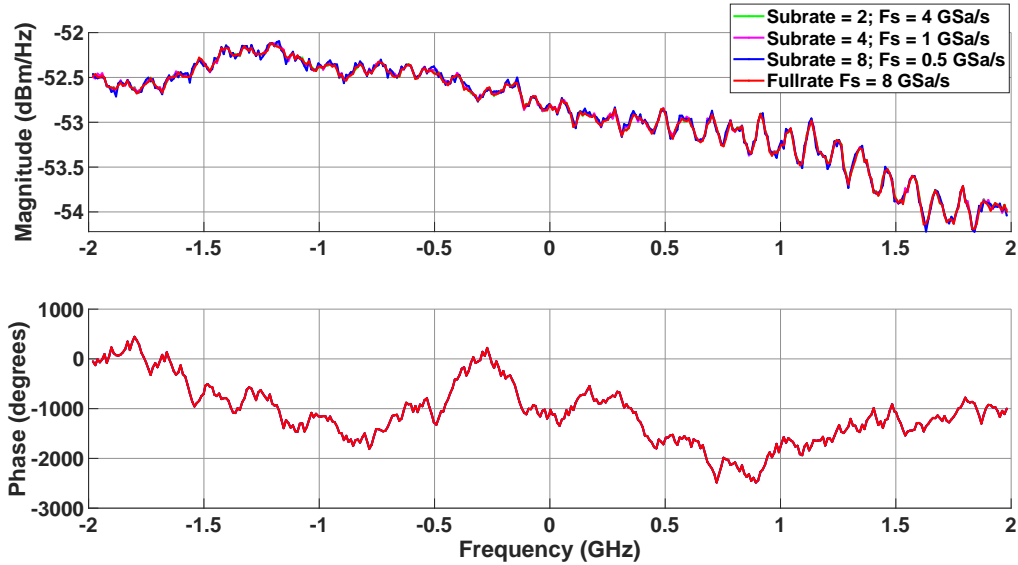
signal quality in terms of the NMSE between the output and input, 300 taps per FIR filter were required in the time domain method whereas the proposed frequency domain approach required 210 tones to identify each compensation LUT. In both cases, the ACPR remained at 46 dBc. Using the compensation filters on the 4 GHz interleaved multi-tone signal, there was a reduction the NMSE from -10.5 dB to -35.9 dB in the frequency domain and -32.8 dB in the time domain approach. The application of the compensation model to the 800 MHz carrier aggregated OFDM signal results in an NMSE of -32.0 dB for both time domain and frequency domain approaches. Based on these results, the proposed method presents a scalable and efficient method to detect and compensate for IQ imbalance effects over wide bandwidths.

Table 3.1: Measured VSG signal quality results before and after IQ imbalance detection and compensation with the time and proposed frequency domain based methods

4 GHz Multi-tone Signal 10.8 dB PAPR			
	Before	Time Domain (300 taps per filter)	Frequency Domain (LUT Approach 210 entries)
NMSE (dB)	-10.5	-32.8	-35.9
ACPR (dBc)	46	46	46
800 MHz Carrier Aggregated OFDM Signal 8.5 dB PAPR			
		Time Domain (300 taps per filter)	Frequency Domain (LUT Approach 210 entries)
NMSE (dB)		-32.0	-32.0
ACPR (dBc)		46	46

Furthermore for validating the proposed method of Section 3.2 of detecting IQ imbalance in direct conversion TXs using a reduced sampling rate TOR, frequency grid offsets were introduced into the interleaved multi-tone test signal with a modulation bandwidth of 4 GHz generated at a $F_s = 8$ GS/s. The starting tone frequency f_0 was set to 2 MHz, $\Delta f = 10$ MHz, and the set of frequency offsets introduced into the p th Nyquist zones of $p = 2$ to $p = 8$ were $\{0 \text{ MHz}, 1 \text{ MHz}, 1 \text{ MHz}, 2 \text{ MHz}, 2 \text{ MHz}, -1 \text{ MHz}, -1 \text{ MHz}\}$ for a target sub-Nyquist sampling rate of 0.5 GS/s. With these frequency offsets introduced into the multi-tone signal, the aliasing phenomenon from the sub-Nyquist sampling TOR does not cause the higher Nyquist zones to overlap with the 1st Nyquist zone or with the other aliased tones. In the validation process, after receiving the equalized TOR's signal $\tilde{y}(n)$ with a complex baseband sampling rate of 8 GS/s, the signal was then downsampled from

Nyquist rate case of 8 GS/s to the sub-Nyquist rates of 1 GS/s and 500 MS/s. From the sub-sampled signal $\tilde{y}(Dn)$, the received non-aliased and aliased tones were identified in the frequency domain and used to reconstruct the NR signal $\tilde{y}(n)$ as shown in Fig. 3.10, where the full rate signal is reconstructed in terms of its magnitude and phase from different sub-sampling rates.



(a)

Figure 3.10: Reconstructed NR rate signal using the sub-sampling TOR at sub-sampling ratios of 2, 4, 8 for IQ imbalance detection.

The resulting measured IQ imbalance compensation results using a NR and sub NR sampling TOR are summarized in Table 3.2, which presents the NMSE and ACPR of the output of the VSG after detecting the IQ imbalance with the modified 4 GHz interleaved multi-tone signal with a PAPR of 8.9 dB. The NMSE values presented in Table 3.2 differ from those in Table 3.1 because a different amplifying path was used in the custom upconverter. However, when examining the improvement in the NMSE both tables show similar performances.

3.3.3 DPD Measurement Results

In this section, the aspect of utilizing DPD to linearize mm-wave PAs driven with wideband signals is validated. The linearization capacity with and without IQ imbalance

Table 3.2: Measured results of the proposed IQ imbalance detection and compensation method with the modified 4 GHz interleaved multi-tone test signal with 200 tones using a NR and sub NR TOR

	Before	TOR Complex Baseband Sampling Rate F_s (GS/s)			
		8	4	1	0.5
NMSE (dB)	-14.0	-37.7	-37.7	-37.1	-36.5
ACPR (dBc)	46	46	46	46	46

compensation is also examined to verify the signal quality deterioration when IQ imbalance compensation is not applied. In the following application of DPD with the proposed IQ imbalance compensation method, the CRV behavioural model in [11] is rearranged to give

$$\begin{aligned}
 \tilde{y}(n) = & \sum_{\substack{i=0 \\ i \text{ even}}}^N \alpha_i \tilde{x}(n) |\tilde{x}(n)|^i + \sum_{m=1}^{M_L} \beta_m \tilde{x}(n-m) \\
 & + \sum_{\substack{i=1 \\ i \text{ odd}}}^N \sum_{m=1}^{M_{NL}} \sum_{\substack{k=2 \\ k \text{ even}}}^N \gamma_{i,m,k} \tilde{x}(n) |\tilde{x}(n)|^{i-1} |\tilde{x}(n-m)|^k \\
 & + \sum_{\substack{i=2 \\ i \text{ even}}}^N \sum_{m=1}^{M_{NL}} \sum_{\substack{k=1 \\ k \text{ odd}}}^N \zeta_{i,m,k} |\tilde{x}(n)|^i \tilde{x}(n-m) |\tilde{x}(n-m)|^{k-1},
 \end{aligned} \tag{3.20}$$

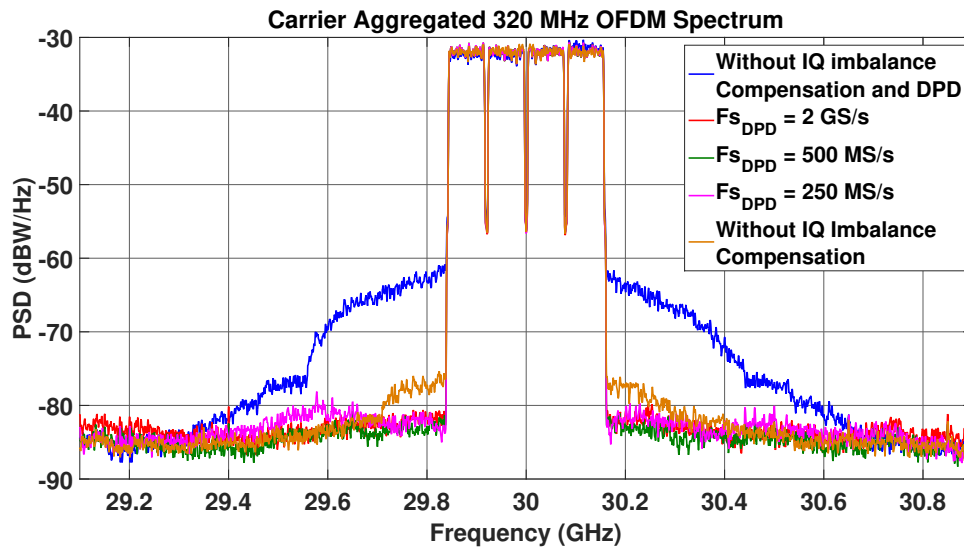
where $\tilde{y}(n)$, $\tilde{x}(n)$ are the complex baseband signal models of the input and output of the PA, respectively. The model settings are given by N the nonlinearity setting, M_L the linear memory depth, and M_{NL} the nonlinear memory depth. The model coefficients are given by the set of coefficients $\{\alpha_i, \beta_m, \gamma_{i,m,k}, \zeta_{i,m,k}\}$.

The rearrangement of the CRV model enables the effective pruning of the model to describe the behaviour of the PA in terms of its static nonlinearity, linear memory and nonlinear memory effects. Specifically, the first sum in (3.20) represents the static nonlinear basis functions. The second sum in (3.20) represents the linear memory basis functions, i.e. the frequency response of the PA. The last two sums in (3.20) represent the nonlinear memory effects. With the model parameters, N , M_L , M_{NL} , the basis functions of the CRV model are chosen to achieve mm-wave PA linearization with ultra-wideband signals. For higher order nonlinear memory basis functions, the M_{NL} setting can be decreased for the

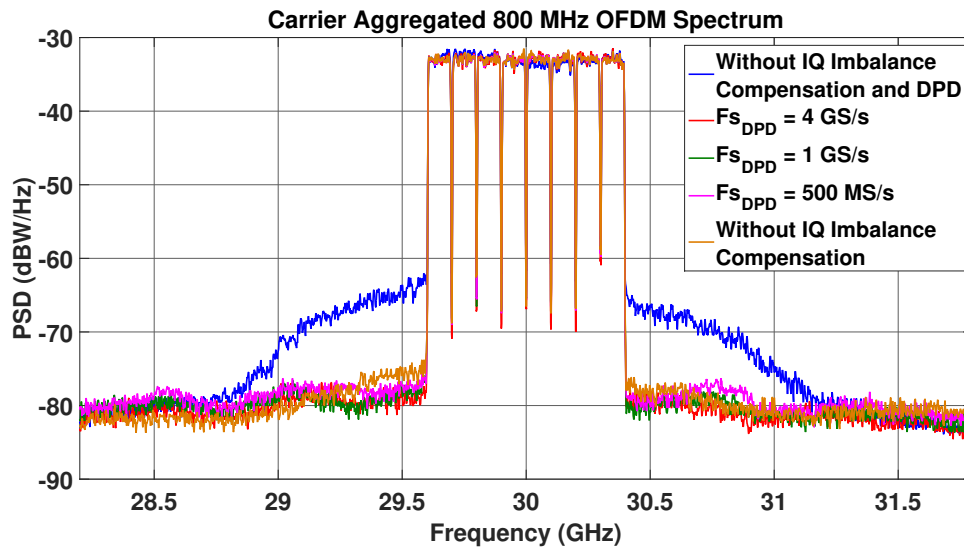
higher order nonlinear memory basis functions. As a result, only the lower order nonlinear memory basis functions will be observed and dominant in their effect on the signal. This leads to the pruning strategy where the resulting model only consist of nonlinear memory basis functions from the rearranged CRV model that fit the condition $(i + m + k) \leq N$. In order to identify the DPD coefficients with the sub-sampling TOR, the full reconstruction of the PA's output signal is not required [31], [32]. Thus to identify the DPD coefficients with a reduced complex baseband sampling rate TOR, the direct learning approach in [32] is employed.

With the obtained IQ imbalance compensation LUTs, a 30 GHz PA (HMC-1131) with an output 1 dB compression point of 23 dBm is inserted in between the VSG and the reduced sampling TOR with sub-sampling ratios of 4 and 8. The pruned CRV model's linear memory depth was scaled according to the signal bandwidth used and the nonlinear memory basis functions were chosen using the strategy discussed in the previous paragraph. The feasibility of DPD for the linearization of mm-wave PAs driven with ultra-wideband signals was validated using carrier aggregated OFDM signals with modulation bandwidths of 320 MHz and 800 MHz and PAPRs of 8 to 9 dB stimuli for a mm-wave PA at 30 GHz. The spectra of the signals at the output of the mm-wave PA without DPD and IQ imbalance compensation, with DPD and IQ imbalance compensation with a full complex baseband sampling rate TOR of 2 GS/s and 4 GS/s for the 320 MHz and 800 MHz cases, respectively, and sub-sampling ratios of 4 and 8 are shown in Fig. 3.11. In each case, the resulting signal quality measuring the TX output signal quality and resulting number of DPD model coefficients are shown in Table 3.3. Without IQ imbalance compensation, the predistorter performance is significantly deteriorated in all cases. In the 800 MHz case, the resulting ACPR degradation is not as severe due to the dynamic range limitation of the TOR.

From the measurement results, the linear memory depth, scales with the signal bandwidth implying most of the distortions that scale with the bandwidth are linear memory distortions due to the frequency response of the PA. On the other hand the static nonlinear and nonlinear memory distortions are not dependent on the signal's bandwidth but the amount of distortions captured by the TOR over the TCB. In the case of the 320 MHz signal, the fifth order intermodulation distortion appears well above the measurement noise floor in the captured signal compared to the 800 MHz case and this requires an increase in the nonlinearity order. For both modulation bandwidth cases, less than 100 coefficients are needed for the linearization of the mm-wave PA driven with the wideband signals. Moreover when DPD is applied, there is an NMSE improvement of at least 14 dB in all cases, and the ACPR at the output of the mm-wave PA is improved by at least 10 dBc. By comparing the DPD results and their model sizes in Table 3.3, it is found that with an



(a)



(b)

Figure 3.11: Measured spectra of the mm-wave PA output when driven with ultra-wideband signals at 30 GHz with the reduced sampling rate TOR with sub-sampling ratios of 4 and 8. (a) 320 MHz carrier aggregated OFDM signals (b) 800 MHz carrier aggregated OFDM signal.

Table 3.3: Summary of the measured signal quality before and after linearization of a mm-wave PA using the reduced complex baseband sampling TOR

Carrier Aggregated 320 MHz OFDM Signal					
	No IQ Comp. & No DPD	With CRV DPD ($N = 9, M_{Linear} = 20$) M_{NL} such that ($i + m + k \leq N$) No. DPD Coeff. 77			
		2 GS/s	500 MS/s	250 MS/s	No IQ Comp.
NMSE (dB)	-19.0	-36.5	-35.9	-36.5	-29.9
ACPR (L/U) (dBc)	33/34	50/50	50/50	49/49	47/45
Carrier Aggregated 800 MHz OFDM Signal					
	No IQ Comp. & No DPD	With CRV DPD ($N = 7, M_{Linear} = 40$) M_{NL} such that ($i + m + k \leq N$) No. DPD Coeff. 66			
		4 GS/s	1 GS/s	500 MS/s	No IQ Comp.
NMSE (dB)	-17.4	-32.4	-32.4	-32.0	-22.4
ACPR (L/U) (dBc)	35/37	46/45	45/45	44/44	44/42

increasing modulation bandwidth, only the linear memory depth of the DPD model increases.

3.4 Conclusions

An offline IQ detection and compensation method using an interleaved multi-tone test signal with a reduced sampling rate TOR for mm-wave digital predistortion systems was proposed. The proposed IQ imbalance detection and compensation method was validated a mm-wave IQ upconverter driven with a 4 GHz interleaved multi-tone test signal at 30 GHz. Using a reduced sampling rate TOR resulted a complete reduction in the NMSEs from -14 to -38 dBc between the input and output signals. With the IQ imbalance compensated TX, a rearranged CRV model for mm-wave PA linearization facilitated the flexibility in choosing

the model's basis functions allowing for the reduction in the number of DPD coefficients. The low complexity DPD scheme with the reduced complex baseband sampling TOR was then used for the successful linearization using of a mm-wave PA operating at 30 GHz and driven by OFDM signals with modulation bandwidths of 320 MHz and 800 MHz. For example, after compensating for the distortions present in the frequency converter, it was used to generate an OFDM signal with a modulation bandwidth of 800 MHz, an ACPR level of 45 dBc and an NMSE of -32 dB. It was found that only the linear memory depth of the DPD model needed to be scaled with the modulation bandwidth to successfully linearize a mm-wave PA driven with wideband signals.

Chapter 4

Digital Predistortion for Frequency Multiplier Based High Frequency Wideband Signal Generators

In the conventional architecture in Fig. 4.1(a), the PA is subjected to signals with high PAPR results in nonlinear distortions when the PA is operated in its high power and high efficiency region of operation. To avoid the nonlinear distortions, the PA can be operated in its power back-off region at the cost of a reduced efficiency. However, at high frequencies the output power and efficiency are already limited due to the limited breakdown voltage and maximum oscillation frequency of conventional transistor technologies [5]. For mitigating these nonlinear distortions, DPD schemes can be deployed. Due to the gain compression behaviour exhibited by the PA, the PD exhibits a gain expansion behaviour. Consequently, the predistorted signal possesses an increased PAPR compared to the original signal, which then requires sufficient power backoff to prevent saturation of the PA and limits the benefits of DPD.

The second and third architectures shown in Fig. 4.1(b)-(c) employ a nonlinear mixer or a frequency multiplier as part of the frequency conversion chain. This variant is a potential solution for generating vector modulated signals at the high frequencies where the performance of active circuits, e.g. mixers, and PAs are limited. For instance, it enables the generation of signals past the maximum oscillation frequency, f_{\max} of typical transistor technologies. The maximum oscillation frequency is characterized by the frequency at which the maximum available power gain drops to unity.

To investigate the frequency multiplier based signal generation system, this chapter will

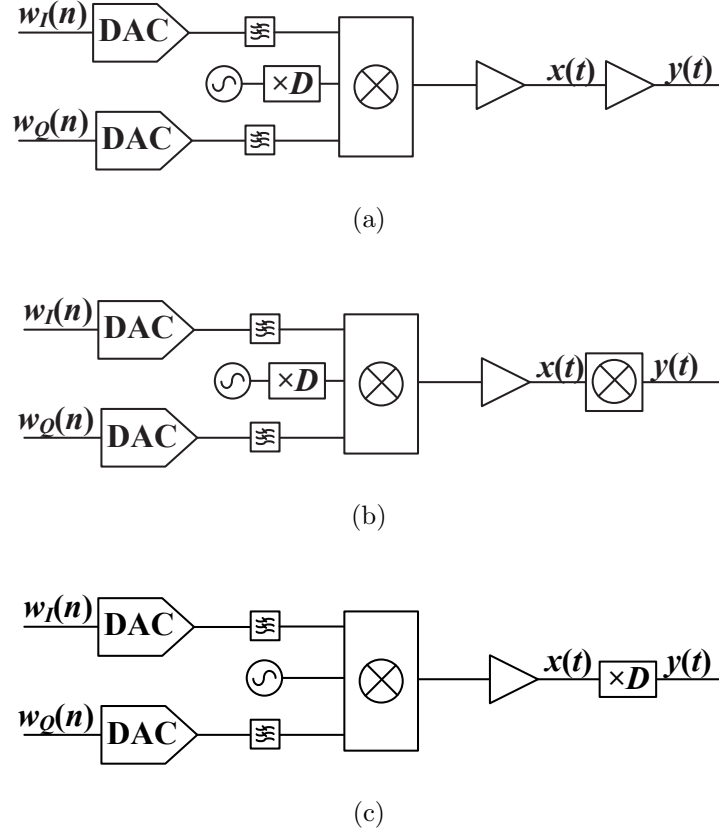


Figure 4.1: (a) Conventional signal generation system (b) Nonlinear mixer based signal generation (c) Frequency multiplier based signal generation system.

first provide an overview of the current techniques to generate signals at high frequencies and compensation schemes for frequency multipliers driven with vector modulated signals. Following the literature review is the derivation of the proposed Volterra series based behavioural model and description of the proposed Volterra series influenced DPD scheme for frequency multipliers. The impact of the innate nonlinear nature of the frequency multiplier on the input noise signal is then studied. Lastly, the test and measurement results to validate the potential of frequency multiplier based high frequency wideband vector signal generators is validated at the mm-wave as a proof of concept. The work in this chapter extends the work done in [33].

4.1 Literature Review

There have been attempts to use conventional direct conversion or heterodyne signal generation architectures for the high mm-wave and sub-THz frequency ranges, such as [34]–[37]. Given the limitations of the semiconductor technologies in the operation near the f_{\max} , the results with low order modulation schemes showed limited output power and signal quality. This motivates the need to investigate alternative methods for vector modulated signal generation.

To tackle the issue of low output power near and above f_{\max} , the architecture shown in Fig. 4.1(b) with cubic and square mixers with power combining have been proposed in [38], [39] for the frequency conversion of vector modulated signals to the high frequencies. However the nonlinear mixing results in non-negligible image and spurious signals located close to the frequency band of interest, thereby requiring an additional high order filtering stage at the output.

In order to improve the achievable signal quality and relax the output filter requirement at the high frequencies, the third variant in Fig. 4.1(c) employs a frequency multiplier as part of the frequency conversion chain. This enables the extension of existing high quality low frequency vector signal sources for the generation of signals at carrier frequencies that are comparable or higher than f_{\max} . When frequency multipliers are used for frequency conversion, they are typically driven by spectrally inefficient constant envelope signals, such as frequency modulated continuous wave radar signals [40]–[42] or phase modulated signals [35], [43]. With vector modulated signals, the architecture in Fig. 4.1(c) can be duplicated and arranged into an outphasing configuration [44], [45]. Although the frequency multipliers are driven by outphased phase modulated signals, when the modulation bandwidth increases, significant calibration efforts are required to mitigate the amplitude and phase imbalance between the paths. When the architecture in Fig. 4.1(c) is used directly to generate vector modulated signals, the frequency multiplier is driven with spectrally efficient vector modulated signals exhibiting high PAPRs and would result in unwanted nonlinear distortions. To mitigate the unwanted distortions linearization techniques such as digital predistortion (DPD) can be deployed.

Motivated by the application of DPD for the linearization of PAs, several approaches to linearize frequency multipliers driven by vector modulated signals have been proposed in the literature and were validated at the microwave and W-band frequency ranges [46]–[52]. In [46], look up table (LUT) and polynomial function based models for the behavioural modelling and predistortion of frequency multipliers were proposed. This was then extended in [47]–[49] in the application of frequency doubler based dual-band transmitters.

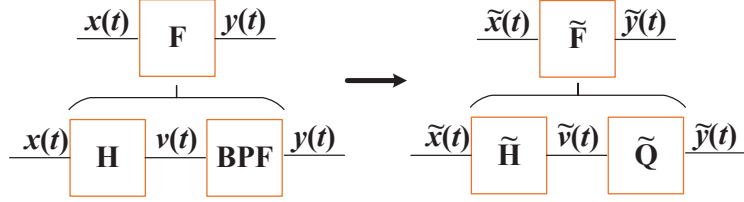


Figure 4.2: Frequency multiplier model and its complex baseband equivalent model.

These works proposed a low-complexity DPD scheme, but demonstrated limited linearization capacity with relatively narrowband validation signals. The polynomial based DPD for frequency multipliers was extended in [50] to generate low order modulation signals (QPSK and 16-QAM) at the W-band frequencies, but the results showed that there were non-negligible residual distortions after applying the polynomial based PDs. Recently in [51], an approach to linearize frequency quadruplers when stimulated with high order QAM signals using a quadrupling memory polynomial based DPD was proposed. However, the approach resulted in a cascade of two high complexity DPD modules, and the results shown demonstrated limited linearization capacity as the relatively low modulation bandwidth increased. Furthermore, authors in [52] proposed a phase retarder predistorter for frequency sextuplers to generate phase shift keying (PSK) signals. However, post compensation methods were required to cope with residual distortions for recovering the PSK symbols.

To enable high quality, wideband and spectral efficient vector modulated signals (e.g. high order QAM and OFDM) at the high frequencies, this thesis proposes frequency multiplier based vector signal generation using a three box DPD module to compensate for the nonlinear distortions exhibited by frequency multipliers.

4.2 Frequency Multiplier Behavioural Models

Below, we derive the CBBE Volterra model for a non-ideal frequency multiplier. We consider the frequency multiplier system F with a noiseless passband input $x(t)$ and a passband output $y(t)$ shown in Fig. 4.2. It is composed of a nonlinear module H followed by a BPF to reject unwanted harmonics. The nonlinear module H is modelled using a continuous time Volterra series [53], which relates the passband output signal $v(t)$ to the

passband input signal $x(t)$ by

$$v(t) = \sum_{n=0}^{\infty} \int_{\mathbb{R}^n} h(\boldsymbol{\tau}_n) \prod_{j=1}^n x(t - \tau_j) d\boldsymbol{\tau}_n, \quad (4.1)$$

where $\boldsymbol{\tau}_n = [\tau_1, \dots, \tau_n]^T$ and the Volterra kernels are denoted by $h(\boldsymbol{\tau}_n)$. The passband signal $x(t)$ is related to its CBBE signal $\tilde{x}(t)$ and the angular carrier frequency ω_c by

$$\begin{aligned} x(t) &= \mathcal{R} \{ \tilde{x}(t) e^{j\omega_c t} \} \\ &= \frac{1}{2} (\tilde{x}(t) e^{j\omega_c t} + \tilde{x}^*(t) e^{-j\omega_c t}). \end{aligned}$$

Using this representation, the output $v(t)$ can be written as

$$\begin{aligned} v(t) &= \sum_{n=0}^{\infty} \int_{\mathbb{R}^n} h(\boldsymbol{\tau}_n) \prod_{j=1}^n \mathcal{R} \{ \tilde{x}(t - \tau_j) e^{j\omega_c(t - \tau_j)} \} d\boldsymbol{\tau}_n \\ &= \sum_{n=0}^{\infty} \int_{\mathbb{R}^n} \frac{h(\boldsymbol{\tau}_n)}{2^n} \prod_{j=1}^n (\tilde{x}(t - \tau_j) e^{j\omega_c(t - \tau_j)} + \tilde{x}^*(t - \tau_j) e^{-j\omega_c(t - \tau_j)}) d\boldsymbol{\tau}_n. \end{aligned} \quad (4.2)$$

The equation in (4.2) results in harmonic components centered at integer multiples of ω_c can be expressed as

$$\begin{aligned} v(t) &= \sum_{k=0}^{\infty} v_k(t) \\ &= \sum_{k=0}^{\infty} \mathcal{R} \{ \tilde{v}_k(t) e^{jk\omega_c t} \}, \end{aligned}$$

where $\tilde{v}_k(t)$ combines all of the product terms of (4.2) that result in a carrier component of $k\omega_c$. At the output of the nonlinear module H , a BPF is used to reject the unwanted harmonics in $v(t)$ resulting in an output

$$y(t) = \mathcal{R} \{ \tilde{v}_D(t) e^{jD\omega_c t} \},$$

that only possesses frequency components centered around $D\omega_c$. To find an expression for $\tilde{y}(t) = \tilde{v}_D(t)$, from the n -fold integral in (4.2), the terms with the carrier term $e^{jD\omega_c t}$ need to be determined. As the terms in (4.2) with angular carrier frequencies of $D\omega_c$ are only obtained from the product of $k + D$ non-conjugate terms $\tilde{x}(t - \tau_j) e^{j\omega_c(t - \tau_j)}$ and

k conjugated terms $\tilde{x}^*(t - \tau_j)e^{-j\omega_c(t - \tau_j)}$, we first consider the products of order $2k + D$, $k = 0, 1, 2, \dots$. Hence, the passband signal $s(t)$ containing only product orders of $2k + D$ is given by

$$\begin{aligned} s(t) &= \sum_{k=0}^{\infty} \int_{\mathbb{R}^{2k+D}} \frac{h(\boldsymbol{\tau}_{2k+D})}{2^{2k+D}} \prod_{j=1}^{2k+D} (\tilde{x}(t - \tau_j)e^{j\omega_c(t - \tau_j)} + \tilde{x}^*(t - \tau_j)e^{-j\omega_c(t - \tau_j)}) d\boldsymbol{\tau}_{2k+D} \\ &= \sum_{k=0}^{\infty} \int_{\mathbb{R}^{2k+D}} \frac{h(\boldsymbol{\tau}_{2k+D})}{2^{2k+D}} s(t, \boldsymbol{\tau}_{2k+D}) d\boldsymbol{\tau}_{2k+D}, \end{aligned} \quad (4.3)$$

where

$$s(t, \boldsymbol{\tau}_{2k+D}) = \prod_{j=1}^{2k+D} (\tilde{x}(t - \tau_j)e^{j\omega_c(t - \tau_j)} + \tilde{x}^*(t - \tau_j)e^{-j\omega_c(t - \tau_j)}). \quad (4.4)$$

From the 2^{2k+D} possible terms from the products of order $2k + D$ in (4.4), we now isolate the terms with a carrier component of $e^{jD\omega_c t}$. Again, these occur when there is a product of $k + D$ positive and k negative carrier components from the $2k + D$ fold product. To isolate the terms in the product that lead to a linear combination of the product terms that belong to $\tilde{y}(t)$, we first define a set \mathcal{S}_k^{2k+D} of all binary vectors \mathbf{c} of length $2k + D$ with $k + D$ ones and k zeros:

$$\mathcal{S}_k^{2k+D} = \left\{ \mathbf{c} \in \{0, 1\}^{2k+D} \mid \sum_{u=1}^{2k+D} c_u = k + D \right\}.$$

We can then write the terms of the $2k + D$ fold product with a carrier component $e^{jD\omega_c t}$ as

$$\begin{aligned} \tilde{\xi}(t, \boldsymbol{\tau}_{2k+D}) &= \sum_{\mathbf{c} \in \mathcal{S}_k^{2k+D}} \prod_{j=1}^{2k+D} (\tilde{x}(t - \tau_j)e^{-jD\omega_c \tau_j})^{c_j} (\tilde{x}^*(t - \tau_j)e^{jD\omega_c \tau_j})^{1-c_j} \\ &= \sum_{\mathbf{c} \in \mathcal{S}_k^{2k+D}} \prod_{j=1}^{2k+D} e^{jD\omega_c \tau_j(1-2c_j)} (\tilde{x}(t - \tau_j))^{c_j} (\tilde{x}^*(t - \tau_j))^{1-c_j} \\ &= \sum_{\mathbf{c} \in \mathcal{S}_k^{2k+D}} A(\boldsymbol{\tau}_{2k+D}, \mathbf{c}) \prod_{j=1}^{2k+D} (\tilde{x}(t - \tau_j))^{c_j} (\tilde{x}^*(t - \tau_j))^{1-c_j}, \end{aligned} \quad (4.5)$$

where $A(\boldsymbol{\tau}_{2k+D}, \mathbf{c}) = \prod_{j=1}^{2k+D} e^{jD\omega_c\tau_j(1-2c_j)}$. Using the linear combination of product terms identified in (4.5) with a carrier component $e^{jD\omega_c t}$, the passband output signal $y(t)$ containing only the D th harmonic of $v(t)$ can be written as

$$\begin{aligned} y(t) &= \sum_{k=0}^{\infty} \int_{\mathbb{R}^{2k+D}} \frac{h(\boldsymbol{\tau}_{2k+D})}{2^{2k+D}} \left(\tilde{\xi}(t, \boldsymbol{\tau}_{2k+D}) e^{jD\omega_c t} + \tilde{\xi}^*(t, \boldsymbol{\tau}_{2k+D}) e^{-jD\omega_c t} \right) d\boldsymbol{\tau}_{2k+D} \\ &= \frac{1}{2} \left(\tilde{y}(t) e^{jD\omega_c t} + \tilde{y}^*(t) e^{-jD\omega_c t} \right). \end{aligned}$$

Consequently, we can then write the CBBE of the output signal $\tilde{y}(t)$ as

$$\begin{aligned} \tilde{y}(t) &= \sum_{k=0}^{\infty} \int_{\mathbb{R}^{2k+D}} \frac{h(\boldsymbol{\tau}_{2k+D})}{2^{2k+D-1}} \tilde{\xi}(t, \boldsymbol{\tau}_{2k+D}) d\boldsymbol{\tau}_{2k+D} \\ &= \sum_{k=0}^{\infty} \int_{\mathbb{R}^{2k+D}} \sum_{\mathbf{c} \in \mathcal{S}_k^{2k+D}} \tilde{g}(\boldsymbol{\tau}_{2k+D}, \mathbf{c}) \prod_{j=1}^{2k+D} (\tilde{x}(t - \tau_j))^{c_j} (\tilde{x}^*(t - \tau_j))^{1-c_j} d\boldsymbol{\tau}_{2k+D}, \quad (4.6) \end{aligned}$$

where

$$\tilde{g}(\boldsymbol{\tau}_{2k+D}, \mathbf{c}) = \frac{h(\boldsymbol{\tau}_{2k+D})}{2^{2k+D-1}} A(\boldsymbol{\tau}_{2k+D}, \mathbf{c}).$$

The expression in (4.6) can further be simplified by combining duplicate distortion basis functions. For example, $\boldsymbol{\tau}_5 = [\tau_1, \tau_2, \tau_3, \tau_4, \tau_5]^T$, and $\mathbf{c} = [1, 1, 1, 1, 0]^T$ results in a distortion basis function $\tilde{x}(t - \tau_1)\tilde{x}(t - \tau_2)\tilde{x}(t - \tau_3)\tilde{x}(t - \tau_4)\tilde{x}^*(t - \tau_5)$, which is the same as the distortion basis function $\tilde{x}^*(t - \tau_5)\tilde{x}(t - \tau_1)\tilde{x}(t - \tau_2)\tilde{x}(t - \tau_3)\tilde{x}(t - \tau_4)$ generated by $\boldsymbol{\tau}'_5 = [\tau_5, \tau_1, \tau_2, \tau_3, \tau_4]^T$, and $\mathbf{c}' = [0, 1, 1, 1, 1]^T$. This is because $\boldsymbol{\tau}_5$ and \mathbf{c} are related to $\boldsymbol{\tau}'_5$ and \mathbf{c}' through the same permutation, $\pi \in \mathcal{P}_{2k+D}(k+D)$, i.e. π is the permutation resulting in $\pi(\boldsymbol{\tau}_5) = \boldsymbol{\tau}'_5$, $\pi(\mathbf{c}) = \mathbf{c}'$. Hence, consider a reference binary vector $\mathbf{c}_{k+D,k} \in \mathcal{S}_k^{2k+D}$ defined by

$$\mathbf{c}_{k+D,k} = \underbrace{[1, \dots, 1]}_{k+D \text{ ones}}, \underbrace{[0, \dots, 0]}_{k \text{ zeros}}]^T,$$

and it is noted that every vector $\mathbf{c} \in \mathcal{S}_k^{2k+D}$ is a permutation of this reference vector $\mathbf{c}_{k+D,k}$.

Then, the continuous time CBBE Volterra model for the frequency multiplier with a multiplication factor of D is given by

$$\tilde{y}(t) = \sum_{k=0}^{\infty} \int_{\mathbb{R}^{2k+D}} \tilde{f}(\boldsymbol{\tau}_{2k+D}) \prod_{i=1}^{k+D} \tilde{x}(t - \tau_i) \prod_{j=k+D+1}^{2k+D} \tilde{x}^*(t - \tau_j) d\boldsymbol{\tau}_{2k+D}, \quad (4.7)$$

where the effective Volterra kernels $\tilde{f}(\boldsymbol{\tau}_{2k+D})$ are given by

$$\tilde{f}(\boldsymbol{\tau}_{2k+D}) = \sum_{\pi \in \mathcal{P}_{2k+D}(k+D)} \tilde{g}(\pi(\boldsymbol{\tau}_{2k+D}), \pi(\mathbf{c}_{k+D,k})). \quad (4.8)$$

In the case where we apply the Volterra kernel's symmetry property where for any permutation $\pi \in \mathcal{P}_{2k+D}(k+D)$, $h(\pi(\boldsymbol{\tau}_{2k+D})) = h(\boldsymbol{\tau}_{2k+D})$, our effective Volterra kernels simplify to

$$\tilde{f}(\boldsymbol{\tau}_{2k+D}) = \binom{2k+D}{k+D} \tilde{g}(\boldsymbol{\tau}_{2k+D}, \mathbf{c}_{k+D,k}), \quad (4.9)$$

since there are $\binom{2k+D}{k+D}$ permutations in $\mathcal{P}_{2k+D}(k+D)$.

To apply this CBBE Volterra behavioural model to a physical frequency multiplier system, we now constrain the model's maximum nonlinearity order up to $2N + D$, apply the causality property of the physical model, and apply the limited memory constraint where only inputs up to time $T_{ss} < \infty$ contribute to the output resulting in

$$\tilde{y}(t) = \sum_{k=0}^N \int_{[0, T_{ss}]^{2k+D}} \tilde{f}(\boldsymbol{\tau}_{2k+D}) \prod_{i=1}^{k+D} \tilde{x}(t - \tau_i) \prod_{j=k+D+1}^{2k+D} \tilde{x}^*(t - \tau_j) d\boldsymbol{\tau}_{2k+D} \quad (4.10)$$

as the continuous time CBBE Volterra model for a physical frequency multiplier with a multiplication factor D .

The bandlimited output signal is then sampled at a sampling rate of f_s and written in its triangular form, which results in

$$\tilde{y}(n) = \sum_{k=0}^N \sum_{\ell_1^{k+D} \in \mathcal{I}_{k+D}} \sum_{\ell_{k+D+1}^{2k+D} \in \mathcal{I}_k} \tilde{f}(\ell_1^{2k+D}) \prod_{i=1}^{k+D} \tilde{x}(n - \ell_i) \prod_{j=k+D+1}^{2k+D} \tilde{x}^*(n - \ell_j) \quad (4.11)$$

as the discrete time CBBE Volterra model for a frequency multiplier with a multiplication factor D , where $\ell_1^{2k+D} = [\ell_1, \dots, \ell_{2k+D}]^T \in \{0, \dots, M\}^{2k+D}$, such that $M = \lceil T_{ss} f_s \rceil$ and \mathcal{I}_p , for any integer p , denotes the set

$$\mathcal{I}_p = \{\mathbf{q} \in \{0, \dots, M\}^p \mid 0 \leq q_1 \leq \dots \leq q_p \leq M\}.$$

As a first example, if we consider the case of a power amplifier, where $D = 1$, then the discrete time CBBE Volterra model of order $2N + 1$ is given by

$$\tilde{y}(n) = \sum_{k=0}^N \sum_{\ell_1^{k+1} \in \mathcal{I}_{k+1}} \sum_{\ell_{k+2}^{2k+1} \in \mathcal{I}_k} \tilde{f}(\ell_1^{2k+1}) \prod_{i=1}^{k+1} \tilde{x}(n - \ell_i) \prod_{j=k+2}^{2k+1} \tilde{x}^*(n - \ell_j), \quad (4.12)$$

which is identical to the CBBE model given by [8] and confirms the generalizability of this behavioural model. As a second example, if we consider the case of a frequency doubler where $D = 2$, the discrete time CBBE Volterra model of order $2N + 2$ is given by

$$\tilde{y}(n) = \sum_{k=0}^N \sum_{\ell_1^{k+2} \in \mathcal{I}_{k+2}} \sum_{\ell_{k+3}^{2k+2} \in \mathcal{I}_k} \tilde{f}(\ell_1^{2k+2}) \prod_{i=1}^{k+2} \tilde{x}(n - \ell_i) \prod_{j=k+3}^{2k+2} \tilde{x}^*(n - \ell_j). \quad (4.13)$$

As another example, if we consider the case of a frequency tripler where $D = 3$, the discrete time CBBE Volterra model of order $2N + 3$ is given by

$$\tilde{y}(n) = \sum_{k=0}^N \sum_{\ell_1^{k+3} \in \mathcal{I}_{k+3}} \sum_{\ell_{k+4}^{2k+3} \in \mathcal{I}_k} \tilde{f}(\ell_1^{2k+3}) \prod_{i=1}^{k+3} \tilde{x}(n - \ell_i) \prod_{j=k+4}^{2k+3} \tilde{x}^*(n - \ell_j). \quad (4.14)$$

For a ML frequency multiplier system with multiplier factor D and $M = 0$, the CBBE Volterra model of order $2N + D$ is given by

$$\tilde{y}(n) = \sum_{k=0}^N \tilde{f}_k \tilde{x}^D(n) |\tilde{x}(n)|^{2k}. \quad (4.15)$$

It is interesting to note that the difference between the CBBE Volterra series model for a frequency multiplier and that of a PA (i.e. where $D = 1$) is that the basis terms now introduce PM-PM distortion where the output phase is scaled by the frequency multiplication factor D . This scaling will introduce a bandwidth expansion by a factor of D and consequently, the TOR path used for training the DPD scheme must be able to capture this bandwidth expansion. However in practice, the D th order root box of the DPD module, as shown in the following section, can be used to reduce for this bandwidth expansion of D prior to sending the signal.

4.3 Digital Predistortion for Frequency Multipliers Driven With Vector Modulated Signals

In this section, the proposed three module DPD model of [33] is extended for the linearization of the general frequency multiplier system. The model is shown in Fig. 4.3 where \tilde{H}_{IQ} represents the frequency response of the signal generation system, \tilde{F} represents the frequency multiplier system, \tilde{G}_{IQ} represents the linear filter to compensate for the signal

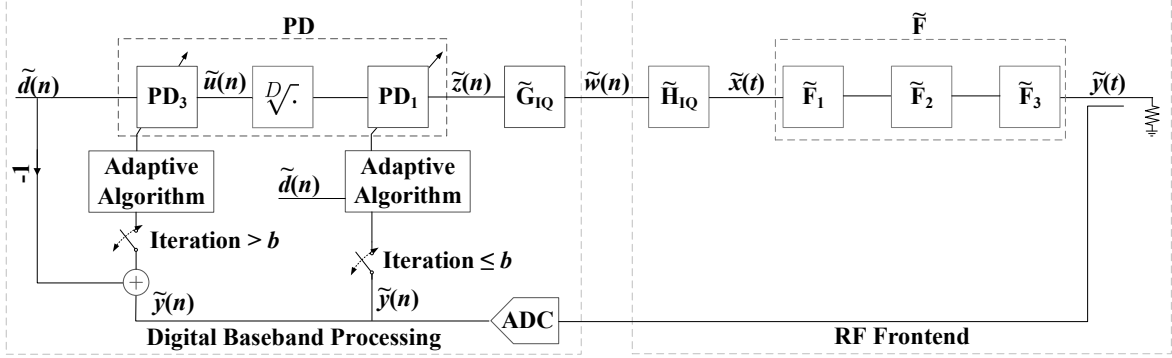


Figure 4.3: Frequency multiplier DPD module and the frequency multiplier based vector signal generator block diagram.

generation module's frequency response, PD_1 represents the first predistorter module, and PD_3 represents the third predistorter module.

In reality, either passive frequency multipliers or active frequency multipliers can be employed into the vector signal generator. Passive frequency multipliers are required to be driven into their nonlinear region and exhibit a conversion loss [54]. While, active frequency multipliers are often biased at or below the threshold voltage and would require sufficient drive power for the circuit to operate in its appropriate nonlinear region [54]. To accommodate for these two different implementations, the frequency multiplier system \tilde{F} includes an input buffer amplifier represented by \tilde{F}_1 to ensure that the frequency multiplier block denoted by \tilde{F}_2 is driven into its nonlinear region to maximize the desired output harmonic. The output buffer represented by \tilde{F}_3 is used to boost the signal power or to drive the PA. To correct for the PM-PM distortions and the strong AM-AM distortions from the frequency multiplier module \tilde{F}_2 , a D -th order root module is needed. A D -th order root is computed as

$$\sqrt[D]{\tilde{u}(n)} = |\tilde{u}(n)|^{1/D} \exp\left(j \frac{\phi_{\text{unwrapped}}(\tilde{u}(n))}{D}\right), \quad (4.16)$$

where the unwrapped phase $\phi_{\text{unwrapped}}(\cdot)$ is needed to avoid discontinuities in the phase. Due to the reduction in the phase variation from the D -th order root module, the spectrum of the predistorted signal is compressed. The input buffer amplifier, \tilde{F}_1 , would then be driven by a relatively narrowband signal with a large skirt at its input. This implies that if the overall frequency multiplier system contains a cascade of multiple frequency multiplication stages, then all stages until the last frequency multiplication stage will be

subjected to narrowband signals. Most of the distortions exhibited by the stages until the last frequency multiplier stage can then be modelled as memoryless distortions. This allows the entire chain can be considered as a single frequency multiplier for DPD training when there is a cascade of multiplier frequency multiplier stages. Thus, a memoryless polynomial module PD_1 is needed to compensate for \tilde{F}_1 's behaviour. The output of the D th order root module and PD_1 is described by

$$\tilde{z}(n) = \sum_{k=1}^{N_1} \psi_{1,k} \sqrt[D]{\tilde{u}(n)} |\tilde{u}(n)|^{(k-1)} \quad (4.17)$$

where N_1 is the nonlinearity setting of the PD_1 .

After \tilde{F}_2 , the desired signal's phase variation will be restored and the signal will be expanded to its original bandwidth. The output buffer amplifier \tilde{F}_3 will then be driven with wideband signals and will exhibit nonlinear distortions and distortions attributed to memory effects. Thus, the complexity reduced Volterra series model of [11] given by

$$\begin{aligned} \tilde{u}(n) = & \sum_{\substack{i=0 \\ i \text{ even}}}^{N_3} \alpha_i \tilde{d}(n) |\tilde{d}(n)|^i + \sum_{m=1}^{M_{NL3}} \beta_m \tilde{d}(n-m) \\ & + \sum_{\substack{i=1 \\ i \text{ odd}}}^{N_3} \sum_{m=1}^{M_{NL3}} \sum_{\substack{k=2 \\ k \text{ even}}}^{N_3} \gamma_{i,m,k} \tilde{d}(n) |\tilde{d}(n)|^{i-1} |\tilde{d}(n-m)|^k \\ & + \sum_{\substack{i=2 \\ i \text{ even}}}^{N_3} \sum_{m=1}^{M_{NL3}} \sum_{\substack{k=1 \\ k \text{ odd}}}^{N_3} \zeta_{i,m,k} |\tilde{d}(n)|^i \tilde{d}(n-m) |\tilde{d}(n-m)|^{k-1} \end{aligned} \quad (4.18)$$

is used for PD_3 to compensate for the residual nonlinear and linear distortions. In this model, N_3 denotes the nonlinearity setting of PD_3 , M_{L3} denotes the linear memory depth, M_{NL3} denotes the nonlinear memory depth, and the model parameters are denoted by $\{\alpha_i, \beta_m, \gamma_{i,m,k}, \zeta_{i,m,k}\}$. The pruning strategy for this model is based on the reduced nonlinear memory for higher order terms, so the nonlinear memory basis functions are limited to those that satisfy the condition $i + m + k \leq N_3$.

Since the overall predistorted signal $\tilde{z}(n)$ is a nonlinear function of its parameters, the identification of the parameters is done in multiple stages using an iterative direct learning algorithm. PD_3 is first bypassed by setting $\tilde{u}(n) = \tilde{d}(n)$ and the parameters of PD_1 are determined. After b iterations, the training of PD_1 is then paused and the training of PD_3 is performed.

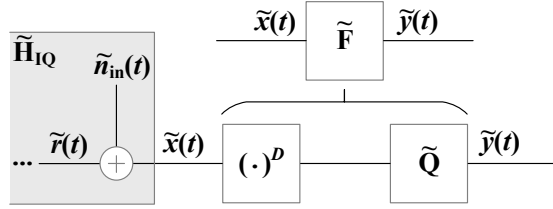


Figure 4.4: Frequency multiplier model used for noise analysis.

A disadvantage of the frequency multiplier based vector signal generation is that the predistorted signal exhibits a large DC component and a large skirt. As discussed in [33], the baseband signal generation hardware will need to be DC coupled or will need to be able to generate the predistorted signal at an IF to prevent additional distortions. Due to the large skirt of the signal and the requirement to generate a signal at an IF, a higher requirement on the sampling rate of the DAC is imposed. If the predistorted signal's bandwidth is not large enough then deterioration in the linearization capacity of the DPD module is compromised as reported in [51].

4.4 Statistical Noise Analysis for Frequency Multipliers

The output noise signal of a linear PA is only a function of the input referred noise signals. However the inherent nonlinear nature of the frequency multiplier requires the effect on the input noise signal to be studied. With this motivation, this section investigates the influence of the frequency multiplier on the input noise signal. The model used in the following noise analysis is shown in Fig. 4.4 where a noiseless and distortionless frequency multiplier is considered followed by a filter denoted by \tilde{Q} . The CBBE input signal $\tilde{x}(t)$ is given by

$$\tilde{x}(t) = \tilde{r}(t) + \tilde{n}_{\text{in}}(t),$$

where $\tilde{r}(t)$ is the noiseless output of the signal generation module and $\tilde{n}_{\text{in}}(t)$ is the added output referred noise of the signal generation module that is independent of the signal $\tilde{r}(t)$. For the following derivation, we consider the frequency response \tilde{H}_{IQ} of the signal generation shown in Fig. 4.3 to be pre-compensated for, resulting in $\tilde{r}(t) = \tilde{z}(t)$ where $\tilde{z}(t)$ is the predistorted signal. The noise component $\tilde{n}_{\text{in}}(t)$ is modelled as a circularly symmetric

complex random signal with zero mean and power $\text{E} |\tilde{n}_{\text{in}}(t)|^2 = 2\sigma_N^2$. The factor of 2 is merely added for the sake of normalization as will become apparent in the derivations below. Specifically, we consider the case where $\tilde{n}_{\text{in}}(t)$ is the thermal noise added by the signal generation module, and can thus be described by a circularly symmetric complex Gaussian signal with zero mean and power $\text{E} |\tilde{n}_{\text{in}}(t)|^2 = 2\sigma_N^2$, i.e. $\tilde{n}_{\text{in}}(t) \sim \mathcal{CN}(0, 2\sigma_N^2)$. Moreover, we assume the noiseless component $\tilde{z}(t)$ to be modelled as a circularly symmetric complex random signal with zero mean and power $\text{E} |\tilde{z}(t)|^2 = 2\sigma_s^2$. If we assume that $\tilde{z}(t)$ is an OFDM signal, then it is well modelled as a circularly symmetric complex Gaussian signal with zero mean, i.e. $\tilde{z}(t) \sim \mathcal{CN}(0, 2\sigma_s^2)$.

At the input to the frequency multiplier, the passband signal is related to its CBBE components through

$$x(t) = \frac{1}{2} (\tilde{x}(t)e^{j\omega_c t} + \tilde{x}^*(t)e^{-j\omega_c t}).$$

The passband signal $x(t)$ is zero mean, since $\text{E}[\tilde{x}(t)] = 0$. As a result, the power of $x(t)$ is given by

$$\begin{aligned} \text{E} [x^2(t)] &= \frac{1}{4} \text{E} \left[(\tilde{x}(t)e^{j\omega_c t} + \tilde{x}^*(t)e^{-j\omega_c t})^2 \right] \\ &= \frac{1}{4} \text{E} [\tilde{x}^2(t)e^{j2\omega_c t} + 2\tilde{x}(t)\tilde{x}^*(t) + (\tilde{x}^*(t))^2 e^{-j2\omega_c t}] \\ &= \frac{1}{2} \text{E} |\tilde{x}(t)|^2, \end{aligned} \tag{4.19}$$

where $\text{E}[\tilde{x}^2(t)] = 0$ and $\text{E}[(\tilde{x}^*(t))^2] = 0$ due to the circularly symmetric property of $\tilde{x}(t)$. As a result the total power of the passband signal $x^2(t)$ is determined by

$$\begin{aligned} \text{E} [x^2(t)] &= \frac{1}{2} \text{E} |\tilde{x}(t)|^2 \\ &= \frac{1}{2} \text{E} |\tilde{z}(t) + \tilde{n}_{\text{in}}(t)|^2 \\ &= \frac{1}{2} \text{E} [|\tilde{z}(t)|^2 + 2\mathcal{R} \{\tilde{z}(t)\tilde{n}_{\text{in}}^*(t)\} + |\tilde{n}_{\text{in}}(t)|^2] \\ &= \frac{1}{2} (\text{E} |\tilde{z}(t)|^2 + \text{E} |\tilde{n}_{\text{in}}(t)|^2), \end{aligned}$$

where $\text{E} [\mathcal{R} \{\tilde{z}(t)\tilde{n}_{\text{in}}^*(t)\}] = \mathcal{R} \{\text{E} [\tilde{z}(t)\tilde{n}_{\text{in}}^*(t)]\} = 0$ because $\tilde{z}(t)$ and $\tilde{n}_{\text{in}}(t)$ are independent and zero mean. As a result, the input signal power at the input of the frequency multiplier

is given by

$$\begin{aligned} \mathbb{E} [z^2(t)] &= \frac{1}{2} \mathbb{E} |\tilde{z}(t)|^2 \\ &= \sigma_s^2, \end{aligned}$$

while the input noise power is given by

$$\begin{aligned} \mathbb{E} [n_{\text{in}}^2(t)] &= \frac{1}{2} \mathbb{E} |\tilde{n}_{\text{in}}(t)|^2 \\ &= \sigma_N^2, \end{aligned}$$

and it is noted that the normalization factor of 2 introduced in $\mathbb{E} |\tilde{z}(t)|^2$ and $\mathbb{E} |\tilde{n}_{\text{in}}(t)|^2$ is used to cancel out the factor of 1/2 in (4.19). The ratio of the input signal power and noise power yields the input SNR:

$$\text{SNR}_{\text{in}} = \frac{\mathbb{E} |\tilde{z}(t)|^2}{\mathbb{E} |\tilde{n}_{\text{in}}(t)|^2}. \quad (4.20)$$

When the passband signal $x(t)$ passes through the distortionless and noiseless frequency multiplier with a frequency multiplication factor of D , the bandpass filtered output signal $y(t)$ after accounting for a gain of q from the filter \tilde{Q} , is written in terms of its CBBE components as

$$y(t) = \frac{q}{2^D} \left(\tilde{x}^D(t) e^{jD\omega_c t} + (\tilde{x}^*(t))^D e^{-jD\omega_c t} \right), \quad (4.21)$$

where

$$\begin{aligned} \tilde{x}^D(t) &= (\tilde{z}(t) + \tilde{n}_{\text{in}}(t))^D \\ &= \tilde{z}^D(t) + \underbrace{\sum_{k=1}^D \binom{D}{k} \tilde{z}^{D-k}(t) \tilde{n}_{\text{in}}^k(t)}_{\tilde{n}_{\text{out}}(t)}. \end{aligned} \quad (4.22)$$

The only term in (4.22) that contributes to a desired signal term is the term given by $\tilde{z}^D(t)$, while the other terms in the binomial expansion are the noise and distortion components denoted as $\tilde{n}_{\text{out}}(t)$. Hence using (4.21) and (4.22), it is deduced that the desired output signal term, $s_{\text{out}}(t)$, in terms of its CBBE components is given by

$$s_{\text{out}}(t) = \mathcal{R} \{ \tilde{z}^D(t) e^{jD\omega_c t} \},$$

and the output noise term $n_{\text{out}}(t)$ in terms of its CBBE components is given by

$$n_{\text{out}}(t) = \mathcal{R} \left\{ \tilde{n}_{\text{out}}(t) e^{jD\omega_c t} \right\}.$$

Then, the power of the output signal $y(t)$ is given by

$$\begin{aligned} \mathbb{E} [y^2(t)] &= \frac{q^2}{2^{2D}} \mathbb{E} \left[(|\tilde{x}(t)|^2)^D \right] \\ &= \frac{q^2}{2^{2D}} \mathbb{E} \left[(|\tilde{z}(t) + \tilde{n}_{\text{in}}(t)|^2)^D \right], \end{aligned}$$

while the power of the desired signal term $s_{\text{out}}(t)$ is given by

$$\mathbb{E} [s_{\text{out}}^2(t)] = \frac{q^2}{2^{2D}} \mathbb{E} \left[(|\tilde{z}(t)|^2)^D \right].$$

and the power of the output noise signal, $n_{\text{out}}(t)$, of the frequency multiplier is given by

$$\mathbb{E} [n_{\text{out}}^2(t)] = \frac{q^2}{2^{2D}} \mathbb{E} \left[(|\tilde{z}(t) + \tilde{n}_{\text{in}}(t)|^2)^D \right] - \frac{q^2}{2^{2D}} \mathbb{E} \left[(|\tilde{z}(t)|^2)^D \right]. \quad (4.23)$$

To evaluate the expectations above, we now use the facts that $\tilde{z}(t) \sim \mathcal{CN}(0, 2\sigma_s^2)$, and $\tilde{n}_{\text{in}}(t) \sim \mathcal{CN}(0, 2\sigma_N^2)$. Then, $|\tilde{z}(t)|^2$, $|\tilde{n}_{\text{in}}(t)|^2$, and $|\tilde{x}(t)|^2$ are distributed according to exponential distributions with means $2\sigma_s^2$, $2\sigma_N^2$, and $2(\sigma_s^2 + \sigma_N^2)$, respectively. Using the moments of the exponential distribution, the total output power of $y(t)$ can be written as

$$\begin{aligned} \mathbb{E} [y^2(t)] &= \frac{q^2}{2^{2D}} \mathbb{E} \left[(|\tilde{x}(t)|^2)^D \right] \\ &= \frac{q^2}{2^D} D! (\sigma_s^2 + \sigma_N^2)^D. \end{aligned}$$

With a normalization factor $q^2 = 2^D / D!$, the output signal power can be written as

$$\begin{aligned} \mathbb{E} [s_{\text{out}}^2(t)] &= \frac{q^2}{2^{2D}} \mathbb{E} \left[(|\tilde{z}(t)|^2)^D \right] \\ &= (\sigma_s^2)^D, \end{aligned}$$

while the power of the output noise term $n_{\text{out}}(t)$ is given by

$$\begin{aligned}
\mathbb{E} [n_{\text{out}}^2(t)] &= \frac{q^2}{2^{2D}} \mathbb{E} \left[(|\tilde{z}(t) + \tilde{n}_{\text{in}}(t)|^2)^D \right] - \frac{q^2}{2^{2D}} \mathbb{E} \left[(|\tilde{z}(t)|^2)^D \right] \\
&= (\sigma_s^2 + \sigma_N^2)^D - (\sigma_s^2)^D \\
&= (\sigma_s^2)^D + \sum_{k=1}^D \binom{D}{k} (\sigma_s^2)^{D-k} (\sigma_N^2)^k - (\sigma_s^2)^D \\
&= \sum_{k=1}^D \binom{D}{k} (\sigma_s^2)^{D-k} (\sigma_N^2)^k.
\end{aligned} \tag{4.24}$$

Even for a noiseless and distortionless frequency multiplier, (4.24) shows that the output noise power $\mathbb{E} [n_{\text{out}}^2(t)]$ depends on both the input signal and noise powers as well as the multiplication factor D . This can affect the linearization results and careful attention should be given to maximize the input signal power σ_s^2 to minimize the contribution of the noise and mixed signal and noise powers, i.e. terms with $(\sigma_s^2)^{D-k} (\sigma_N^2)^k$, on the total output noise power $\mathbb{E} [n_{\text{out}}^2(t)]$. For the case where $\sigma_s^2 \gg \sigma_N^2$, a first order approximation can be made for (4.24) to find that

$$\mathbb{E} [n_{\text{out}}^2(t)] \approx D(\sigma_s^2)^{D-1} (\sigma_N^2) \tag{4.25}$$

$$= \frac{D(\sigma_s^2)^D}{\text{SNR}_{\text{in}}}. \tag{4.26}$$

Furthermore, if we assume an input signal power of $\mathbb{E} |\tilde{z}(t)|^2 = 2\sigma_s^2 = 2 \text{ W}$, then

$$\mathbb{E} [n_{\text{out}}^2(t)] \approx D(\sigma_s^2) \tag{4.27}$$

$$= \frac{D}{\text{SNR}_{\text{in}}}, \tag{4.28}$$

which under these assumptions, the input noise power experiences a minimum power gain of $10 \log_{10}(D)$ dB. The relationship between the output noise signal's power and the input SNR of (4.24) is illustrated in Fig. 4.5 when $\sigma_s^2 = 1 \text{ W}$, which confirms that the input noise signal experiences a gain of $10 \log_{10}(D)$ (dB) due to the inherent nonlinearity of the distortionless and noiseless frequency multiplier, which is not seen in the case for a linear and noiseless PA. Furthermore, given a desired output noise power, the corresponding signal to noise ratio required from the signal source driving the frequency multiplier with a certain multiplication factor D can be determined from Fig. 4.5.

As discussed in Section 4.2, the bandwidth of the signal is expanded by a minimum of D . Thus, the equivalent noise that appears at the output from the input should also be

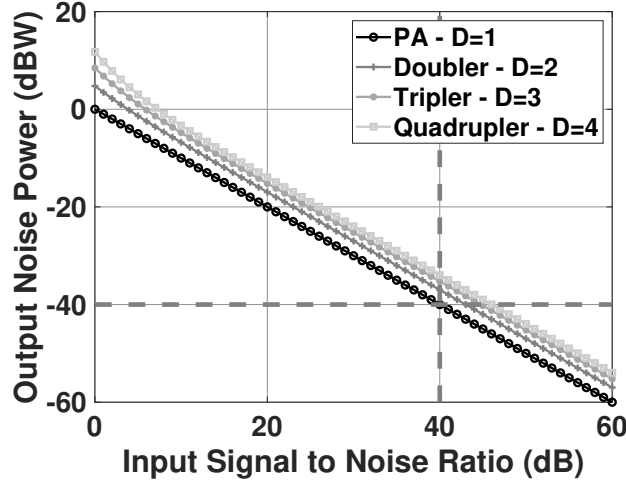


Figure 4.5: Output noise power versus the input signal to noise ratio assuming $\sigma_s^2 = 1$ W for distortionless and noiseless PAs, doublers, triplers, and quadruplers.

considered over the bandwidth expansion of D . To account for this, the total input noise power σ_N^2 should be considered to be spread over D times the input signal bandwidth. Consequently, the noise power in the input signal's bandwidth only, which is denoted by $\sigma_{N,BW}^2$, is related to the total input noise power through

$$\sigma_{N,BW}^2 = \frac{\text{E} |\tilde{n}_{in}(t)|^2}{D}. \quad (4.29)$$

With this noise bandwidth consideration, the relationship in (4.28), which assumes $\sigma_s^2 \gg \sigma_N^2$, and $\sigma_s^2 = 1$ W, becomes

$$\text{E} [n_{out}^2(t)] \approx D^2(\sigma_{N,BW}^2), \quad (4.30)$$

which implies that the input noise power within the bandwidth of the signal experiences a gain of $10 \log_{10}(D^2)$ dB as it passes through the frequency multiplier. It is noted that when $D = 1$, such as the case with PAs, the output noise power still equals to the input noise power for a distortionless and noiseless PA.

In implementing a frequency multiplier based signal generation module, the dominant noise source in the system is the quantization noise of the DAC, which can be considered as a white noise process. To illustrate the deterioration, an ideal frequency multiplier is considered for simulation. The desired signal $\tilde{d}(t)$ is an OFDM signal with a modulation

bandwidth of 200 MHz, a normalized power of 0 dBm, and a PAPR of 9.5 dB. The signal $\tilde{z}(n)$ is corrupted by quantization noise $\tilde{n}_{in}(t)$ distributed according to a complex uniform distribution $\mathcal{U}[\frac{-\Delta}{\sqrt{8}}(1+j), \frac{\Delta}{\sqrt{8}}(1+j)]$ before passing into the frequency multiplier. The parameter Δ represents the quantization step size and for the purpose of this simulation a DAC with 8.5 bits is used, which is similar to the effective number of bits of the DAC used in the measurement setup in the following section. This results in an input noise power of $\sigma_{N,BW}^2 = -53$ dBm. Since an ideal frequency multiplier is considered, only the D -th root box from Section 4.3 is required. The output spectra of the frequency doubler, tripler, and quadrupler normalized to 0 dBm are shown without predistortion in Fig. 4.6(a) and with predistortion in Fig. 4.6(b). By only considering the in-band noise power for the cases with and without predistortion, Table 4.1 shows the resulting simulated $E|\tilde{n}_{out}(n)|^2$, and the predicted $E|\tilde{n}_{out}(n)|^2$ based on (4.23).

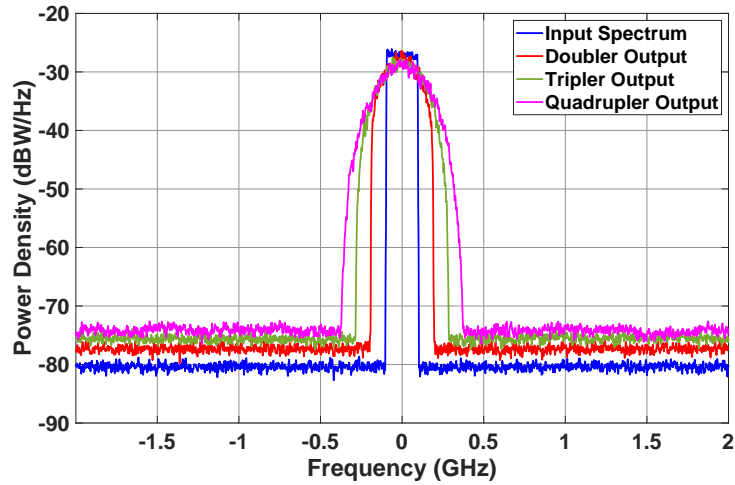
Table 4.1: Simulated impact of a noiseless and distortionless frequency multiplier on the input noise signal given an input signal power of $E|\tilde{z}(n)|^2 = 0$ dBm and an output signal power of $E[(|\tilde{z}(n)|^2)^D] = 0$ dBm

		Without DPD		With DPD	
D	$\sigma_{N,BW}^2$ (dBm)	Simulated $E \tilde{n}_{out}(n) ^2$ (dBm)	Predicted $E \tilde{n}_{out}(n) ^2$ (dBm)	Simulated $E \tilde{n}_{out}(n) ^2$ (dBm)	Predicted $E \tilde{n}_{out}(n) ^2$ (dBm)
2	-53.0	-47.0	-47.0	-47.8	-48.0
3		-43.5	-43.4	-44.7	-44.4
4		-40.9	-40.9	-41.8	-41.8

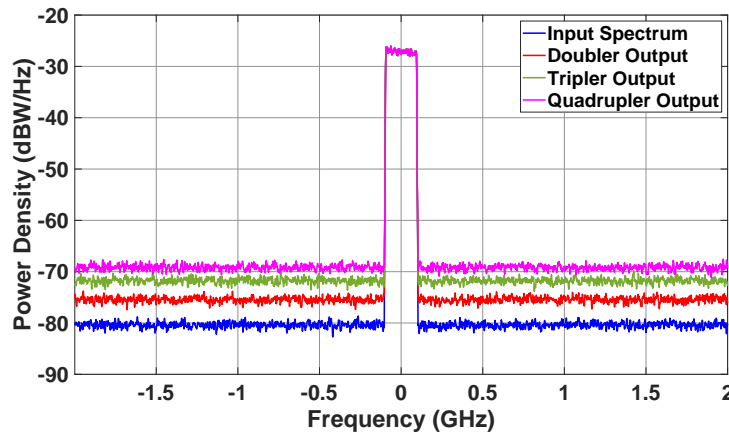
4.5 Test and Measurement Results

The test and measurement setup shown in Fig. 4.7 was used to validate the linearization capacity of the proposed DPD scheme when applied to a frequency doubler with an output centered around 12.5 GHz, a frequency quadrupler with an output centered around 25 GHz and a frequency tripler with an output centered around 63 GHz.

To cope with the wide spread of output frequencies, dedicated up-converters and down-converters were used. A Keysight 12 bit, 12 GS/s arbitrary waveform generator (AWG) (M8190A) is used to first generate the test signals at an IF of 1.35 GHz for the frequency doubler and quadrupler, and 1.55 GHz for the frequency tripler. The custom built IQ



(a)



(b)

Figure 4.6: Output spectra of an ideal frequency multiplier (a) without predistortion applied, and (b) with predistortion applied.

board is then used to condition the IF signals and provide a mechanism to control the DC offset and cancel the LO feedthrough of the IQ mixer. At the output of the IF signal generation stage, a directional coupler is used to monitor its output signal, $x(t)$, and synthesize a pre-equalization filter to compensate for its non-flat frequency response. The frequency response of the vector signal analysis (VSA) stage in the setup is characterized for post-digitization equalization using a pre-calibrated multi-frequency source (Keysight's

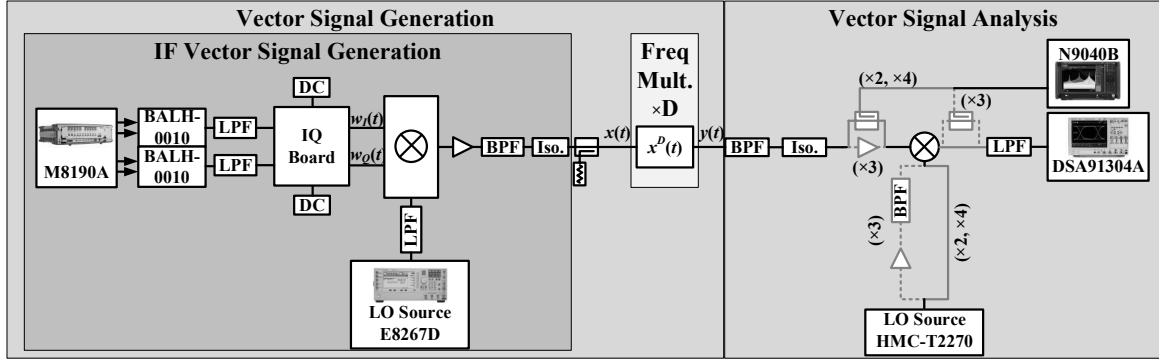


Figure 4.7: Test setup for investigating frequency multiplier based signal generation [27], [29], [55], [56]

U9391G). In the following, a detailed description of the various components used to build the test setup in Fig. 4.7 is given.

- Frequency Doubler and Quadrupler Linearization:** An IQ mixer (MLIQ-0416 from Marki Microwave) is used in the frequency doubler and quadrupler validation cases to up-convert the AWG's IF output signal to a frequency of 6.25 GHz. The IF signal is then filtered, and amplified using the gain amplifier (MAAM-011109 from MACOM). This was followed by an isolator (CS-6.000 from Meca Electronics) to reduce the amount of reflections in the interface between the frequency multiplier input and the output of the IF signal generation stage. For the frequency doubler and quadrupler case, a frequency doubler (HMC573 from Analog Devices) is utilized as the first frequency multiplier in the chain to up-convert the signal to 12.5 GHz. A directional coupler is then used to assess the proposed DPD scheme's linearization capacity for a frequency doubler. For the assessment of the proposed DPD scheme for linearizing a frequency quadrupler, a second frequency multiplier (A2510-2x-20 from Spacek Labs) is added to the output of the first frequency doubler to up-convert the signal to an output frequency of 25 GHz. To analyze the output of the frequency doubler and quadrupler and train their corresponding PDs, a mixer (MM1-1140H from Marki Microwave) is used to down-convert their output signals to an IF.
- Frequency Tripler Linearization:** An IQ mixer (MLIQ-1845 from Marki Microwave) is used in the frequency tripler case to up-convert the AWG's IF output to a frequency of 21 GHz. The signal is then filtered, and boosted through a cascade of two gain amplifiers (MAAM-011109 from MACOM and HMC6981LS6 from Analog

Devices). The output signal of the frequency tripler (WR12x3 from Virginia Diodes) is centered at 63 GHz. This signal is then fed to a cascade of a custom built BPF, an isolator (QIF-V00000 from Quinstar), a gain amplifier (QGW-50661720 from Quinstar), and a down-converting balanced mixer (SFB-15-N1-M from Sage Millimeter). To generate an LO signal for the down-conversion mixer, a gain amplifier (QGW-50661720 from Quinstar) followed by a custom BPF is used.

A 50 GHz spectrum analyzer (N9040B from Keysight Technologies) is used to view the output spectra of the frequency doubler and quadrupler and the down-converted output spectra of the frequency tripler. The VSA routines and DPD training were performed using resampled data (sampling rate equal to 3 GS/s) collected from Keysight’s 13 GHz, 40 GS/s oscilloscope (DSA91304A) used for digitizing the down-converted signals. Two signal generators (Keysight’s E8267D and HMC-T2270 from Hittite Microwave) are used to provide LO signals for the mixers used in the setup.

The validation of the proposed DPD scheme was carried out using OFDM test signals with modulation bandwidths of 200 MHz and 400 MHz, and PAPRs of 9.5 dB and 9.6 dB, respectively. For the measurement at 12.5 GHz and 25 GHz, each sub-carrier is modulated using 64-QAM, and 256-QAM modulation schemes for the modulation bandwidths of 200 MHz and 400 MHz, respectively. For the measurement at 63 GHz, a sub-carrier modulation scheme of 64-QAM is used for the OFDM signal with a modulation bandwidth of 400 MHz and a PAPR of 9.6 dB.

In each validation step, four major test cases of interest, denoted by (a), (b), (c), and (d), are considered. In case (a), the results of the frequency multiplier’s output signal are shown without DPD applied. While cases (b), (c), and (d) represent the cases where the first two PD modules are applied, all three PD modules are applied with ML settings, and the memory terms are added into the third PD module of the proposed DPD scheme, respectively.

4.5.1 Linearization of a Single Frequency Doubler

As can be deduced from Fig. 4.8, Fig. 4.9, and Table 4.2, without any DPD applied to the doubler (case (a)), the distortions of the frequency doubler causes significant bandwidth expansion, gain and phase variations, and EVMs.

If the DPD is set to compensate for only the ideal squaring envelope transformation of the frequency doubler (case (b)), then the output signal displays residual distortions as shown in Fig. 4.8, and the bandwidth expansion, NMSEs and EVMs are reduced compared

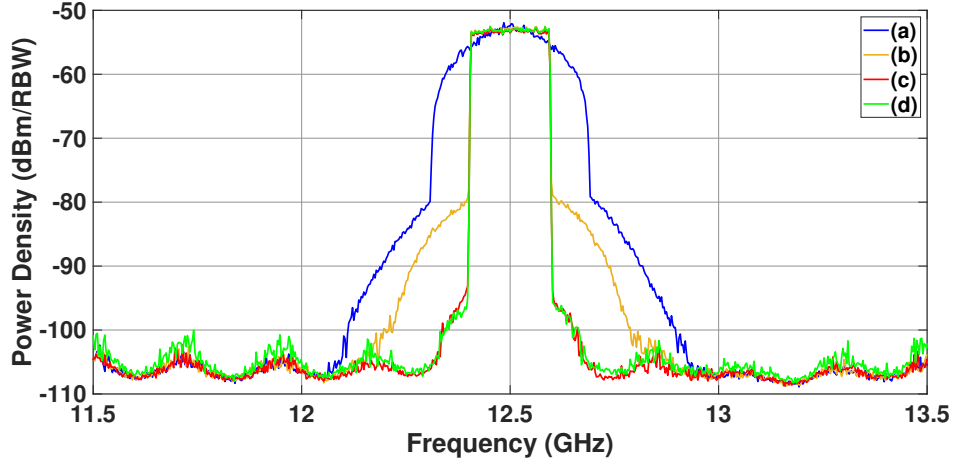
Table 4.2: Linearization results for the frequency doubler system generating OFDM signals at 12.5 GHz

200 MHz OFDM signal with 64 QAM subcarrier modulation				
Case	NMSE (%)	EVM (%)	ACPR L/U (dB)	No. Coef.
(a)	142	2977	9 / 8	0
(b)	8.8	5.9	31 / 30	2
(c)	2.8	1.5	47 / 48	9
(d)	2.4	1.4	48 / 48	52
400 MHz OFDM signal with 256 QAM subcarrier modulation				
Case	NMSE (%)	EVM (%)	ACPR L/U (dB)	No. Coef.
(a)	142	2471	9 / 9	0
(b)	9.2	6.0	31 / 30	2
(c)	3.7	2.0	42 / 45	9
(d)	3.0	1.8	48 / 48	55

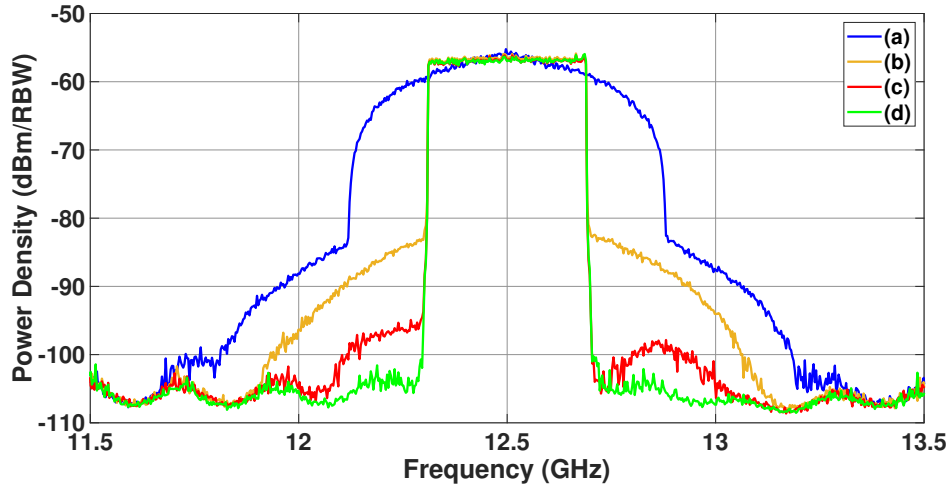
to case (a). To correct for these residual distortions, PD_3 is activated with a ML setting of $N_3 = 6$ (total of 9 DPD coefficients) in case (c), thereby resulting in a complete reduction of the out of band spectral regrowth when the frequency doubler is driven by an OFDM test signal with a modulation bandwidth of 200 MHz as shown in Fig. 4.8(a) and Table 4.2. When the DPD scheme with the same settings is applied to linearize a frequency doubler driven with a OFDM test signal with a 400 MHz of modulation bandwidth, then some residual out of band emissions were observed in Fig. 4.8(b). Based on the results from case (c), it can be concluded that a majority of the distortions exhibited by the frequency doubler can be mitigated using a ML DPD scheme with minimal complexity. Adding additional memory terms to PD_3 (case (d)), by setting $M_{NL3} = 3$, $M_{L3} = 5$ for 200 MHz, and $M_{L3} = 8$ for 400 MHz, resulted in an improved NMSE and EVM, and the balancing of the ACPRs as shown in Table 4.2. This improvement is more significant in the case of the test signal with a modulation bandwidth of 400 MHz as observed in Fig. 4.8 and Table 4.2. It is noted that the inclusion of the memory terms in PD_3 did not escalate the number of DPD coefficients and therefore a minimal complexity DPD scheme is maintained.

4.5.2 Linearization of a Frequency Quadrupler

Similar to the frequency doubler case, if not mitigated, the nonlinear effects from the frequency quadrupler's causes significant bandwidth expansion and exhibits significant deviations from the ideal quartic envelope transformation as shown in Fig. 4.11 and 4.12.



(a)



(b)

Figure 4.8: Measured output spectra of a frequency doubler driven with an OFDM signal with (a) 200 MHz of modulation bandwidth, (b) 400 MHz of modulation bandwidth.

Furthermore, the output signal suffers from excessive EVM as observed in Table 4.3.

When the first PD with $N_1 = 3$ and the quartic root module are activated (case (b)), the results presented in Fig. 4.11 further confirm that there are deviations from an ideal quartic envelope transformation requiring PD_3 . To handle these non-idealities, a ML DPD scheme is used with PD module settings of $N_1 = 3, D = 4, N_3 = 6$. The

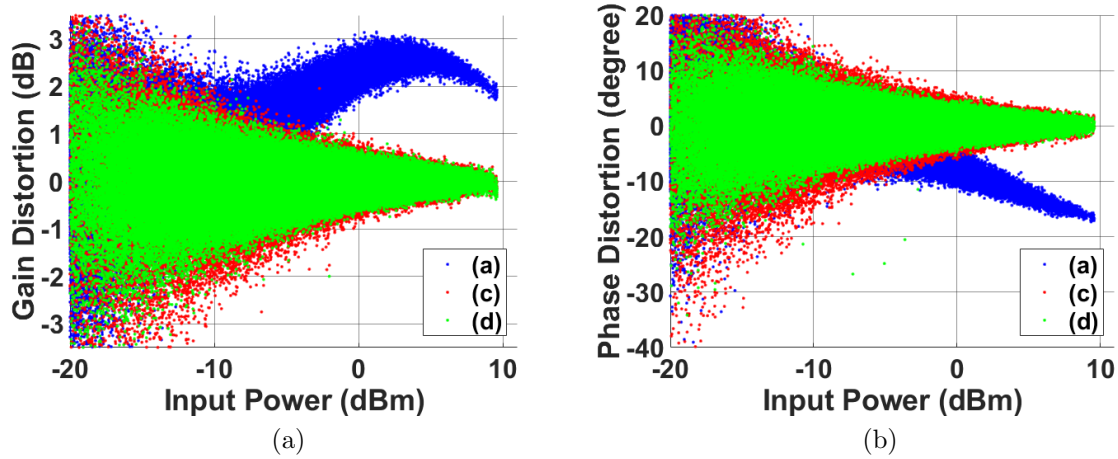


Figure 4.9: Distortion curves of a frequency doubler driven by an OFDM signal with 400 MHz of modulation bandwidth: (a) gain distortion, (b) phase distortion.

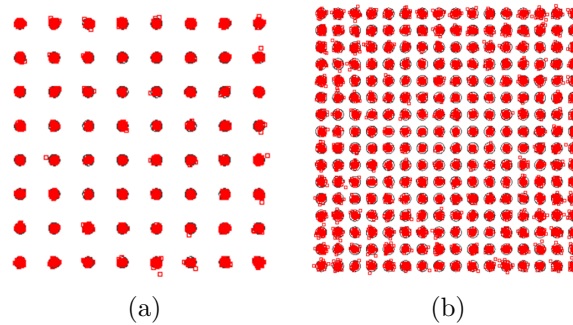
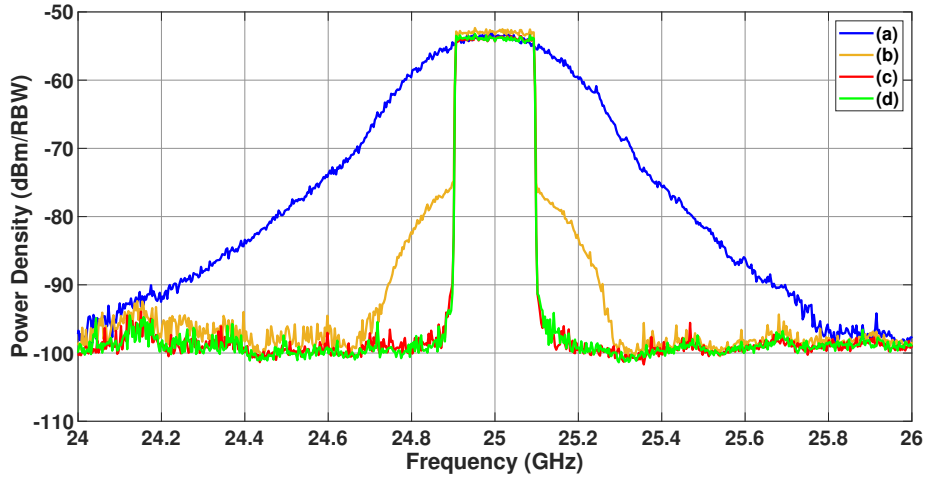
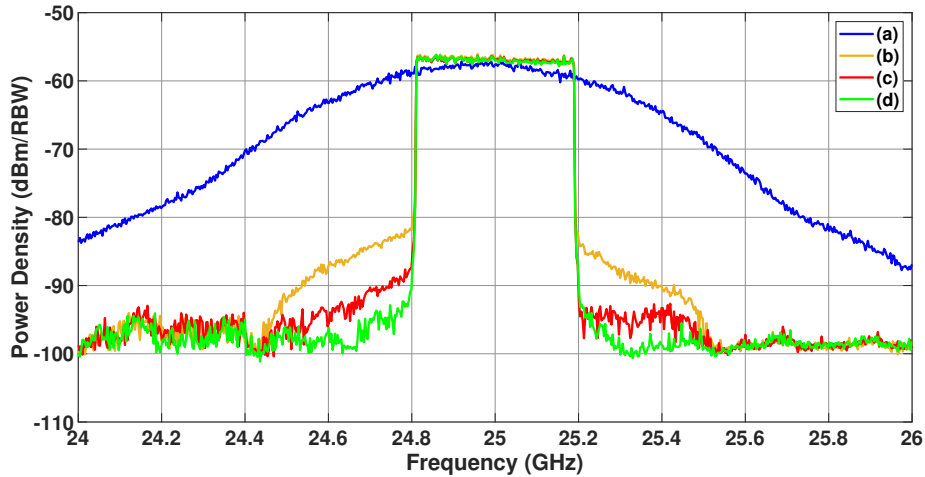


Figure 4.10: Demodulated and equalized OFDM signal's constellations for a linearized frequency doubler driven with (a) 200 MHz of modulation bandwidth at 12.5 GHz for case (d), (b) 400 MHz of modulation bandwidth at 12.5 GHz for case (d).

linearization results summarized in Fig. 4.11 and Table 4.3 reveal similar trends to that of the frequency doubler case. Most of the nonlinear distortions are mitigated in both modulation bandwidth cases. Comparing to the frequency doubler, there are less residual adjacent channel distortions associated with the nonlinear memory effects exhibited by the frequency quadrupler. This can be due to the lower fractional bandwidth of the test signal at the frequency quadrupler's output of 25 GHz. Furthermore, only a single DPD module is required as the predistorted signal is a narrowband signal until the last frequency



(a)



(b)

Figure 4.11: Measured output spectra of a frequency quadrupler driven with an OFDM signal with (a) 200 MHz of modulation bandwidth, (b) 400 MHz of modulation bandwidth.

multiplier stage as discussed in Section 4.3. This implies that all stages up to the second frequency multiplier can be considered to only contribute ML distortions. To correct for the residual distortions, case (d) investigates the use of memory terms in PD_3 resulting in overall DPD settings of $N_1 = 3, D = 4, N_3 = 6, M_{NL3} = 3,$ and $M_{L3} = 5$ for a total

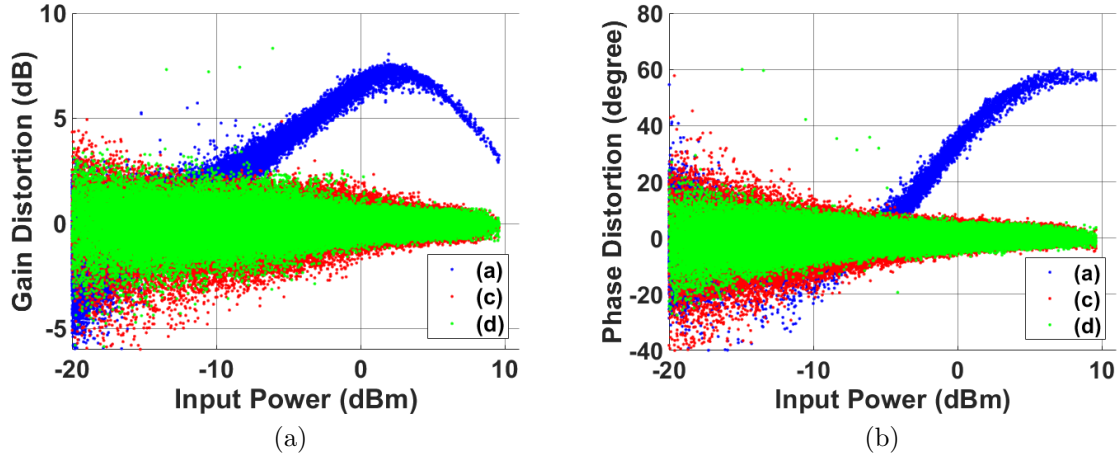


Figure 4.12: Distortion curves of a frequency quadrupler when driven by an OFDM signal with 400 MHz modulation bandwidth: (a) gain distortion, and (b) phase distortion.

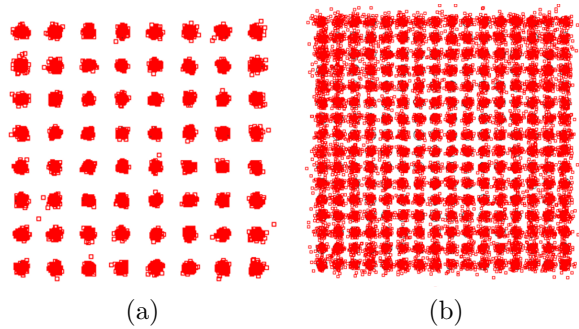


Figure 4.13: Demodulated and equalized OFDM signal's constellations for a Linearized frequency quadrupler driven with (a) 200 MHz of modulation bandwidth at 25 GHz for case (d), and (b) 400 MHz of modulation bandwidth at 25 GHz for case (d).

of 52 coefficients for the 200 MHz case; and $M_{L3} = 8$ for a total of 55 coefficients for the 400 MHz case. When comparing to the frequency doubler case, similar trends are found in Table 4.3 and Fig. 4.11 where the additional memory terms only improve the NMSE and EVM in the 200 MHz case, while the NMSE, EVM and ACPRs are improved in the 400 MHz case. This validation case with the frequency quadrupler consisting of a cascade of frequency doublers demonstrates the excellent capability of the proposed low complexity DPD scheme to compensate for the strong non-idealities present in frequency multipliers.

Table 4.3: Linearization results for a frequency quadrupler generating OFDM signals at 25 GHz

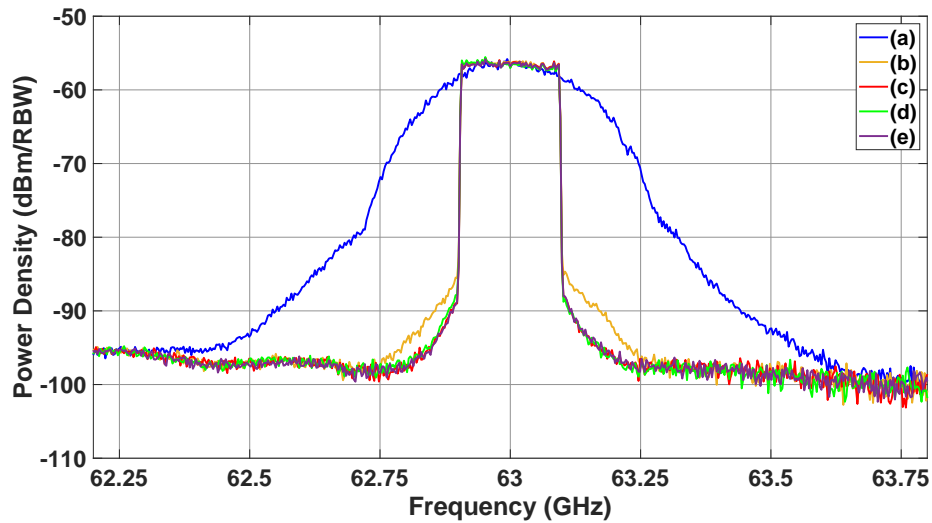
200 MHz OFDM signal with 64 QAM subcarrier modulation				
Case	NMSE (%)	EVM (%)	ACPR L/U (dB)	No. Coef.
(a)	141	1905	5 / 5	0
(b)	9.5	7.3	30 / 31	3
(c)	4.2	3.4	43 / 43	10
(d)	3.5	3.1	43 / 43	53
400 MHz OFDM signal with 256 QAM subcarrier modulation				
Case	NMSE (%)	EVM (%)	ACPR L/U (dB)	No. Coef.
(a)	141	6889	4 / 6	0
(b)	9.4	5.8	29 / 32	3
(c)	5.4	4.1	36 / 39	10
(d)	4.3	3.6	40 / 41	56

4.5.3 Linearization of a Frequency Tripler

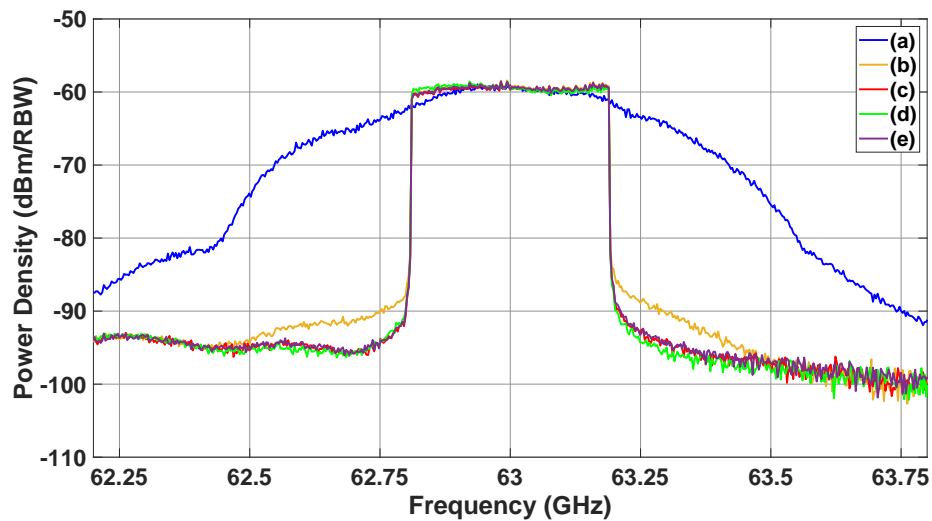
Similar trends in the bandwidth expansion of the output signal caused by the nonlinear distortions of the frequency tripler are observed in Fig. 4.14.

Table 4.4: Linearization results for the frequency tripler system generating OFDM signals at 63 GHz

200 MHz OFDM signal with 64 QAM subcarrier modulation				
Case	NMSE (%)	EVM (%)	ACPR L/U (dB)	No. Coef.
(a)	141	2430	7 / 6	0
(b)	7.0	5.3	35 / 34	2
(c)	5.8	4.7	38 / 37	8
(d)	4.9	4.6	38 / 38	30
(e)	5.8	4.7	38 / 37	8
400 MHz OFDM signal with 64 QAM subcarrier modulation				
Case	NMSE (%)	EVM (%)	ACPR L/U (dB)	No. Coef.
(a)	142	1530	7 / 7	0
(b)	8.9	6.7	31 / 33	2
(c)	7.5	5.8	35 / 35	8
(d)	6.0	5.7	35 / 36	34
(e)	7.6	5.8	35 / 35	8



(a)



(b)

Figure 4.14: Measured output spectra of a frequency tripler driven with an OFDM signal with a (a) 200 MHz modulation bandwidth, (b) 400 MHz modulation bandwidth.

The gain and phase distortions characteristics in Fig. 4.15 confirm the significant deviations of the tripler behaviour from the ideal cubic envelope transformation. When the cubic root and the first PD with $N_1 = 2$ modules are activated (case (b)), residual distortions

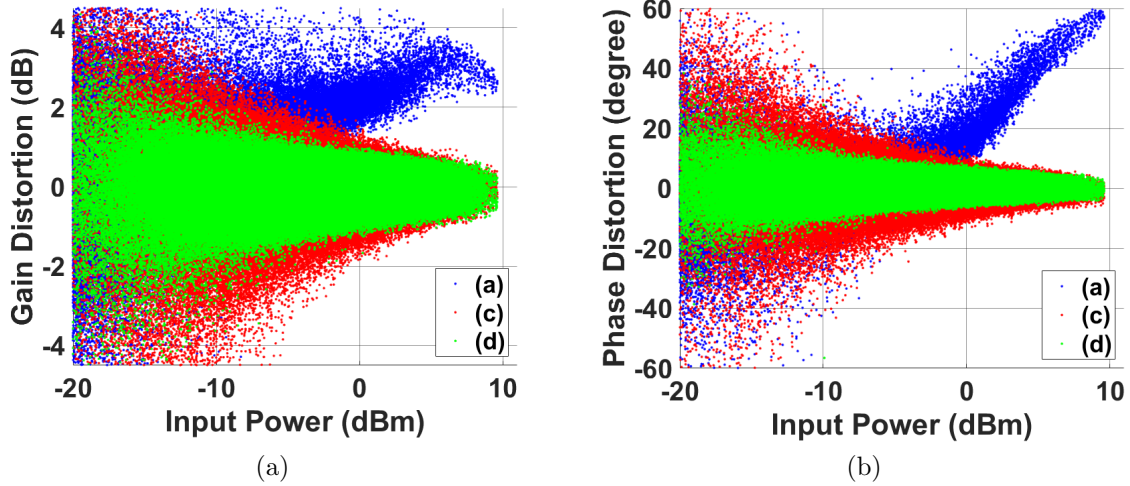


Figure 4.15: Distortion curves of a frequency tripler when driven with an OFDM signal with 400 MHz modulation bandwidth: (a) gain distortion (b) frequency phase distortion.

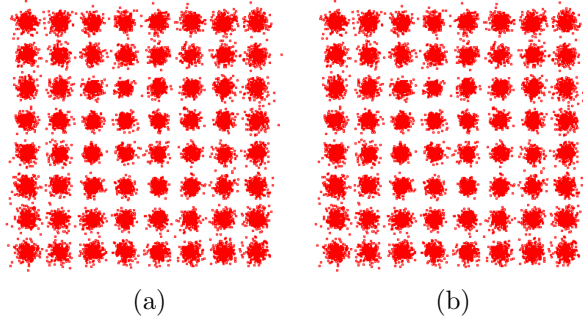


Figure 4.16: Demodulated and equalized OFDM signal's constellations for a linearized frequency tripler driven with (a) 200 MHz of modulation bandwidth at 63 GHz for case (d), (b) 400 MHz modulation bandwidth at 63 GHz for case (d).

tions are observed as shown in Fig. 4.14. ML PDs with ML settings of $N_1 = 2, N_3 = 5$ are utilized (case (c)) to mitigate these residual distortions. As can be determined from Fig. 4.14, all of the observable nonlinear distortions are suppressed. Furthermore, since the output frequency is centered at 63 GHz, the fractional bandwidths of the test signals are small resulting in negligible memory effects. If memory terms are added to PD₃ in case (d), then the following settings were used for the PDs: $N_1 = 2, D = 3, N_3 = 5, M_{NL3} = 2,$ and $M_{L3} = 8$ for the 200 MHz modulation bandwidth case and $M_{L3} = 12$ for the 400

MHz modulation bandwidth case. As can be deduced from Table 4.4, using these additional memory terms in PD_3 improved the NMSE and the EVM in both modulation bandwidth test cases, but did not significantly affect the output signal quality. Similar to the frequency doubler and quadrupler, the frequency tripler predominately exhibits ML distortions. However, the limiting factor in the performance of the DPD scheme for this part of the experiment is the VSA stage's reduced dynamic range resulting in a observed output signal with a reduced SNR for signal analysis and DPD training. Since the distortions exhibited by the frequency multiplier are predominantly ML at high frequencies, the training of the PDs can be done with a narrowband signal to cope with the reduced dynamic range for DPD training. For instance in case (e) shown in Fig. 4.14 and Table 4.4, the ML PD is identified using an OFDM signal with a modulation bandwidth of 50 MHz and the ML PD is applied to the OFDM signals with modulation bandwidths of 200 MHz and 400 MHz. When comparing the ML DPD performances of case (e) and case (b), it is observed that there are no significant differences in the linearization capacity for the two test signals. In spite of the setup limitation, the results show the potential of employing frequency multipliers for extending the signal generation capabilities of vector signal sources to the high frequencies, while using low complexity DPD schemes.

4.6 Conclusions

In this chapter, the non-ideal effects of frequency multipliers on vector modulated input signals were thoroughly analyzed. The analysis lead to the development of an complex baseband equivalent Volterra series behavioural model for representing the envelope transformation of the frequency multiplier. To compensate for the unwanted distortions exhibited by the frequency multiplier driven by vector modulated signals, an accompanying new digital predistortion (DPD) scheme was proposed and its underlying training algorithm was presented. To prove the viability of the proposed DPD scheme while avoiding experimental setup complications at the sub-THz frequency ranges, the proposed DPD scheme was applied to mitigate the unwanted distortions exhibited by frequency doubler, quadrupler, and tripler under test driven by OFDM signals with modulation of 200 MHz and 400 MHz at center frequencies of 12.5 GHz, 25 GHz, and 63 GHz, respectively. Despite its low complexity (low number of coefficients), the proposed DPD scheme demonstrated an excellent linearization capacity to mitigate the unwanted distortions exhibited by frequency multipliers. This paves the road for the application of frequency multipliers for the frequency extension of existing vector signal sources to high frequencies such as millimeter wave and sub-terahertz frequencies.

Chapter 5

Conclusions

In this thesis, two signal generation architectures the accompanying compensation schemes to mitigate the impairments for the generation of wideband modulated at the mm-wave were presented.

In the conventional direct conversion signal generation architectures, the frequency dependent IQ imbalance effects over ultra wide bandwidths were first analyzed. To mitigate the large amounts of distortion, a new interleaved multi-tone test signal based identification and compensation scheme was proposed. The test signal was further modified to be used for a sub-sampling TOR. This scheme was experimentally validated by mitigating the IQ imbalance effects in a direct conversion frequency converter using an off-the-shelf IQ mixer operating at 30 GHz driven with a interleaved multi-tone signal with 4 GHz of modulation bandwidth. The proposed test signal structure enabled IQ imbalance detection and compensation with a reduced sampling rate TOR. Subsequently, a low-complexity pruned Volterra series based DPD scheme was devised to successfully mitigate the nonlinear distortions exhibited by the power amplifier stage and maximize the signal quality of OFDM signals with modulation bandwidths up to 800 MHz.

However as the operating frequency increases into the high mm-wave and sub-THz frequency ranges, the number of challenges associated with the implementation of traditional direct conversion architectures for wideband vector modulated signal generation also increase. A potential solution using a frequency multiplier based vector modulated signal generation system was proposed in this thesis. To study the behaviour of frequency multipliers, a Volterra series based behavioural model was derived to model the nonlinear envelope transformation of frequency multipliers. Afterwards the synthesis of a low complexity DPD scheme to mitigate the nonlinear distortions created by frequency multipliers

driven with non-constant envelope signals was presented. The impact of the intrinsic nonlinear characteristics of a frequency multiplier on the input noise signal was also studied. Various frequency multiplier based signal generation systems were implemented using off-the-shelf frequency doublers, and triplers to serve as proof of concept prototypes at frequencies of 12.5 GHz, 25 GHz, and 63 GHz. These prototypes generated acceptable signal qualities when generating OFDM signals with modulation bandwidths up to 400 MHz and the results of these prototypes are summarized in Fig. 5.1. The experiments confirmed the successful ability to generate wideband OFDM signals with acceptable levels of EVM and ACPR levels with low complexity DPD schemes due to the mainly memoryless behaviour of the frequency multiplier system. The proof of concept prototypes with the proposed low complexity DPD scheme shows the viability in its application to extend the frequency capabilities of vector signal sources to high frequencies.

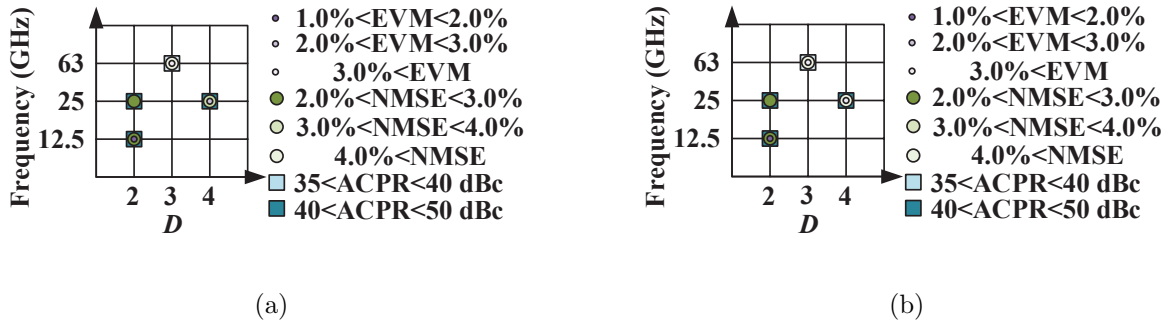


Figure 5.1: Achieved signal quality in the investigation of frequency multiplier based vector signal generation systems for OFDM signals with modulation bandwidths of (a) 160 and 200 MHz and (b) 320 and 400 MHz [33].

5.1 Future Work

For the future of this work, the frequency multiplier based vector signal generation will be extended to be used for higher frequency and wider bandwidth vector signal generation. Furthermore, the cascaded nonlinear effects of a frequency multiplier and the power amplifier operating in its high efficiency region are to be investigated. Lastly, its application in beamforming architectures for vector modulated signal generation at the mm-wave and sub-THz frequencies are to be investigated.

References

- [1] T. S. Rappaport, S. Sun, R. Mayzus, H. Zhao, Y. Azar, K. Wang, G. N. Wong, J. K. Schulz, M. Samimi, and F. Gutierrez, “Millimeter wave mobile communications for 5G cellular: It will work!” *IEEE Access*, vol. 1, pp. 335–349, 2013.
- [2] International Telecommunication Union (ITU), “IMT vision framework and overall objectives of the future development of IMT for 2020 and beyond,” International Telecommunication Union Radiocommunication (ITU-R), Tech. Rep., 2015.
- [3] T. S. Rappaport, Y. Xing, G. R. MacCartney, A. F. Molisch, E. Mellios, and J. Zhang, “Overview of millimeter wave communications for fifth-generation (5G) wireless networks - with a focus on propagation models,” *IEEE Transactions on Antennas and Propagation*, vol. 65, no. 12, pp. 6213–6230, Dec 2017.
- [4] J. Wood, *Behavioral Modeling and Linearization of RF Power Amplifiers*. Artech House, 2014.
- [5] A. Niknejad and H. Hashemi, *mm-Wave Silicon Technology: 60 GHz and Beyond*, ser. Integrated Circuits and Systems. Springer US, 2008.
- [6] L. Ding, Z. Ma, D. R. Morgan, M. Zierdt, and G. T. Zhou, “Compensation of frequency-dependent gain/phase imbalance in predistortion linearization systems,” *IEEE Trans. Circuits Syst. I*, vol. 55, no. 1, pp. 390–397, Feb. 2008.
- [7] S. Cripps, *RF Power Amplifiers for Wireless Communications*, ser. Artech House microwave library. Artech House, 2006.
- [8] S. Benedetto and et al., “Modeling and performance evaluation of nonlinear satellite links-a volterra series approach,” *IEEE Trans. Aerosp. Electron. Syst.*, vol. AES-15, no. 4, pp. 494–507, Jul. 1979.

- [9] A. Zhu, J. C. Pedro, and T. J. Brazil, “Dynamic deviation reduction-based volterra behavioral modeling of RF power amplifiers,” *IEEE Transactions on Microwave Theory and Techniques*, vol. 54, no. 12, pp. 4323–4332, Dec 2006.
- [10] D. R. Morgan, Z. Ma, J. Kim, M. G. Zierdt, and J. Pastalan, “A generalized memory polynomial model for digital predistortion of RF power amplifiers,” *IEEE Transactions on Signal Processing*, vol. 54, no. 10, pp. 3852–3860, Oct 2006.
- [11] F. Mkadem, M. C. Fares, S. Boumaiza, and J. Wood, “Complexity-reduced Volterra series model for power amplifier digital predistortion,” *Analog Integr. Circuits Signal Process.*, vol. 79, no. 2, pp. 331–343, May. 2014.
- [12] L. Ding, F. Mujica, and Z. Yang, “Digital predistortion using direct learning with reduced bandwidth feedback,” in *2013 IEEE MTT-S International Microwave Symposium Digest (MTT)*, June 2013, pp. 1–3.
- [13] A. Chung, M. B. Rejeb, Y. Beltagy, A. M. Darwish, H. A. Hung, and S. Boumaiza, “IQ imbalance compensation and digital predistortion for millimeter-wave transmitters using reduced sampling rate observations,” *IEEE Trans. Microw. Theory Techn.*, vol. 66, no. 7, pp. 3433–3442, July 2018.
- [14] J. K. Cavers and M. W. Liao, “Adaptive compensation for imbalance and offset losses in direct conversion transceivers,” *IEEE Trans. Veh. Technol.*, vol. 42, no. 4, pp. 581–588, Nov. 1993.
- [15] L. Anttila, M. Valkama, and M. Renfors, “Frequency-selective I/Q mismatch calibration of wideband direct-conversion transmitters,” *IEEE Trans. Circuits Syst. II*, vol. 55, no. 4, pp. 359–363, Apr. 2008.
- [16] V. Rampa, “I/Q compensation of broadband direct-conversion transmitters,” *IEEE Trans. Wireless Commun.*, vol. 13, no. 6, pp. 3329–3342, Jun. 2014.
- [17] M. Kim, Y. Maruichi, and J. i. Takada, “Parametric method of frequency-dependent I/Q imbalance compensation for wideband quadrature modulator,” *IEEE Trans. Microwave Theory Techn.*, vol. 61, no. 1, pp. 270–280, Jan. 2013.
- [18] J. Xia, E. Ng, and S. Boumaiza, “Wideband compensation of RF vector multiplier for RF predistortion systems,” *IEEE Trans. Circuits Syst. II*, vol. 63, no. 11, pp. 1084–1088, Nov. 2016.

- [19] J. Luo, A. Kortke, W. Keusgen, and M. Valkama, “Efficient estimation and pilot-free online re-calibration of I/Q imbalance in broadband direct-conversion transmitters,” *IEEE Trans. Veh. Technol.*, vol. 63, no. 6, pp. 2506–2520, Jul. 2014.
- [20] J. K. Cavers, “The effect of quadrature modulator and demodulator errors on adaptive digital predistorters,” in *Proc. of Vehicular Technology Conf. - VTC*, vol. 2. IEEE, Apr. 1996, pp. 1205–1209 vol.2.
- [21] H. Cao, A. S. Tehrani, C. Fager, T. Eriksson, and H. Zirath, “I/Q imbalance compensation using a nonlinear modeling approach,” *IEEE Trans. Microwave Theory Techn.*, vol. 57, no. 3, pp. 513–518, Mar. 2009.
- [22] L. Anttila, P. Handel, and M. Valkama, “Joint mitigation of power amplifier and I/Q modulator impairments in broadband direct-conversion transmitters,” *IEEE Trans. Microwave Theory Techn.*, vol. 58, no. 4, pp. 730–739, Apr. 2010.
- [23] L. Fan, Y. Li, and M. Zhao, “Joint IQ imbalance and PA nonlinearity pre-distortion for highly integrated millimeter-wave transmitters,” in *2014 IEEE Globecom Workshops (GC Wkshps)*, Dec. 2014, pp. 399–404.
- [24] B. Schubert, A. Gkceoglu, L. Anttila, and M. Valkama, “Augmented Volterra predistortion for the joint mitigation of power amplifier and I/Q modulator impairments in wideband flexible radio,” in *2013 IEEE Global Conf. on Signal and Inform.Process.*, Dec. 2013, pp. 1162–1165.
- [25] M. Schroeder, “Synthesis of low-peak-factor signals and binary sequences with low autocorrelation (corresp.),” *IEEE Trans. Inf. Theory*, vol. 16, no. 1, pp. 85–89, January 1970.
- [26] S. Boyd, “Multitone signals with low crest factor,” *IEEE Transactions on Circuits and Systems*, vol. 33, no. 10, pp. 1018–1022, Oct 1986.
- [27] Keysight Technologies, “Keysight M8190A arbitrary waveform generator 12 GSa/s,” 2018. [Online]. Available: <https://www.keysight.com/en/pdx-x201725-pn-DSA91304A/infiniium-high-performance-oscilloscope-13-ghz>
- [28] —, “Keysight N5183B MXG X-series microwave analog signal generator 9 kHz to 40 GHz,” 2018. [Online]. Available: <https://www.keysight.com/en/pd-1969138-pn-M8190A/12-gsa-s-arbitrary-waveform-generator>

- [29] ———, “Keysight DSA91304A Infiniium high performance oscilloscope: 13 GHz,” May 2018. [Online]. Available: <https://www.keysight.com/en/pdx-x202011-pn-N5183B/mxg-x-series-microwave-analog-signal-generator-9-khz-to-40-ghz>
- [30] Y. Beltagy, A. Chung, P. Mitran, and S. Boumaiza, “On the calibration of the feedback receiver using reduced sampling rate and its application to digital predistortion of 5G power amplifiers,” in *2017 IEEE MTT-S International Microwave Symposium (IMS)*, Jun. 2017, pp. 1549–1552.
- [31] Z. Wang, W. Chen, G. Su, F. M. Ghannouchi, Z. Feng, and Y. Liu, “Low feedback sampling rate digital predistortion for wideband wireless transmitters,” *IEEE Trans. Microwave Theory Techn.*, vol. 64, no. 11, pp. 3528–3539, Nov. 2016.
- [32] H. Huang, P. Mitran, and S. Boumaiza, “Digital predistortion function synthesis using undersampled feedback signal,” *IEEE Microw. Wireless Compon. Lett.*, vol. 26, no. 10, pp. 855–857, Oct. 2016.
- [33] A. Chung, M. B. Rejeb, Y. Beltagy, A. Darwish, H. Hung, and S. Boumaiza, “High frequency and wideband modulated signal generation using frequency doublers,” in *2018 IEEE MTT-S Int. Microw. Symp. Dig.*, Jun. 2018.
- [34] H. Song, J. Kim, K. Ajito, N. Kukutsu, and M. Yaita, “50-Gb/s direct conversion QPSK modulator and demodulator MMICs for terahertz communications at 300 GHz,” *IEEE Transactions on Microwave Theory and Techniques*, vol. 62, no. 3, pp. 600–609, March 2014.
- [35] S. Kang, S. V. Thyagarajan, and A. M. Niknejad, “A 240 GHz fully integrated wideband QPSK transmitter in 65 nm CMOS,” *IEEE Journal of Solid-State Circuits*, vol. 50, no. 10, pp. 2256–2267, Oct 2015.
- [36] K. K. Tokgoz, S. Maki, S. Kawai, N. Nagashima, J. Emmei, M. Dome, H. Kato, J. Pang, Y. Kawano, T. Suzuki, T. Iwai, Y. Seo, K. Lim, S. Sato, L. Ning, K. Nakata, K. Okada, and A. Matsuzawa, “13.3 a 56Gb/s W-band CMOS wireless transceiver,” in *2016 IEEE International Solid-State Circuits Conference (ISSCC)*, Jan 2016, pp. 242–243.
- [37] N. Sarmah, P. R. Vazquez, J. Grzyb, W. Foerster, B. Heinemann, and U. R. Pfeiffer, “A wideband fully integrated SiGe chipset for high data rate communication at 240 GHz,” in *2016 11th European Microwave Integrated Circuits Conference (EuMIC)*, Oct 2016, pp. 181–184.

- [38] K. Katayama, K. Takano, S. Amakawa, S. Hara, A. Kasamatsu, K. Mizuno, K. Takahashi, T. Yoshida, and M. Fujishima, “20.1 a 300 GHz 40nm CMOS transmitter with 32-QAM 17.5Gb/s/ch capability over 6 channels,” in *2016 IEEE International Solid-State Circuits Conference (ISSCC)*, Jan 2016, pp. 342–343.
- [39] K. Takano, S. Amakawa, K. Katayama, S. Hara, R. Dong, A. Kasamatsu, I. Hosako, K. Mizuno, K. Takahashi, T. Yoshida, and M. Fujishima, “17.9 a 105Gb/s 300 GHz CMOS transmitter,” in *2017 IEEE International Solid-State Circuits Conference (ISSCC)*, Feb 2017, pp. 308–309.
- [40] K. B. Cooper, R. J. Dengler, G. Chattopadhyay, E. Schlecht, J. Gill, A. Skalare, I. Mehdhi, and P. H. Siegel, “Submillimeter-wave active radar imager,” in *2007 Joint 32nd International Conference on Infrared and Millimeter Waves and the 15th International Conference on Terahertz Electronics*, Sept 2007, pp. 922–923.
- [41] J. Park, H. Ryu, K. Ha, J. Kim, and D. Baek, “76-81-GHz CMOS transmitter with a phase-locked-loop-based multichirp modulator for automotive radar,” *IEEE Transactions on Microwave Theory and Techniques*, vol. 63, no. 4, pp. 1399–1408, April 2015.
- [42] J. Song, C. Cui, S. Kim, B. Kim, and S. Nam, “A low-phase-noise 77-GHz FMCW radar transmitter with a 12.8-GHz PLL and a $\times 6$ frequency multiplier,” *IEEE Microwave and Wireless Components Letters*, vol. 26, no. 7, pp. 540–542, July 2016.
- [43] C. L. Cuccia and E. W. Matthews, “PSK and QPSK modulators for gigabit data rates,” in *1977 IEEE MTT-S International Microwave Symposium Digest*, June 1977, pp. 208–211.
- [44] A. Darwish and et. al., “Efficient linear transmission of complex waveforms at 216 GHz using nonlinear multiplier chains,” in *2016 IEEE MTT-S Int. Microw. Symp. Dig.*, May 2016, pp. 1–3.
- [45] A. Chung, M. B. Rejeb, A. Darwish, H. Hung, and S. Boumaiza, “Frequency doubler based outphasing system for millimeter wave vector signal generation,” in *2018 48th European Microwave Conference (EuMC)*, Sep. 2018.
- [46] Y. Park and J. S. Kenney, “Adaptive digital predistortion linearization of frequency multipliers,” *IEEE Trans. Microw. Theory Techn.*, vol. 51, no. 12, pp. 2516–2522, Dec. 2003.

- [47] Y. Park, R. Melville, R. C. Frye, M. Chen, and J. S. Kenney, “Dual-band transmitters using digitally predistorted frequency multipliers for reconfigurable radios,” *IEEE Trans. Microw. Theory Techn.*, vol. 53, no. 1, pp. 115–122, Jan 2005.
- [48] J. H. Choi, S. M. Kang, and K. H. Koo, “Digital predistortion of frequency multiplier for dual band wireless LAN transmitter,” in *IEEE MTT-S Int. Microwave Symp. Dig, 2005.*, Jun. 2005, pp. 4 pp.–.
- [49] S. M. Kang, S. W. Nam, and K. H. Koo, “Adaptive linearization of frequency doubler using DGS,” in *2007 IEEE/MTT-S International Microwave Symposium*, June 2007, pp. 1225–1228.
- [50] Y. Zhao, L. Deng, X. Pang, X. Yu, X. Zheng, H. Zhang, and I. T. Monroy, “Digital predistortion of 75–110 GHz W-band frequency multiplier for fiber wireless short range access systems,” *Opt. Express*, vol. 19, no. 26, pp. B18–B25, Dec 2011.
- [51] Y. Liu, G. Liu, and P. M. Asbeck, “High-order modulation transmission through frequency quadrupler using digital predistortion,” *IEEE Trans. Microwave Theory Tech.*, vol. 64, no. 6, pp. 1896–1910, Jun. 2016.
- [52] D. Nopchinda, Z. He, G. Granstrom, M. Gavell, and H. Zirath, “8-PSK upconverting transmitter using E-band frequency sextupler,” *IEEE Microwave and Wireless Components Letters*, vol. 28, no. 2, pp. 177–179, Feb 2018.
- [53] M. Schetzen, *The Volterra and Wiener theories of nonlinear systems*, ser. A Wiley - Interscience publication. Wiley, 1980.
- [54] S. Maas, *Nonlinear Microwave and RF Circuits*. Artech House, 2003.
- [55] Keysight Technologies, “Keysight E8267D PSG vector signal generator, 100 kHz to 44 GHz,” May 2018. [Online]. Available: <https://www.keysight.com/en/pdx-x202238-pn-E8267D/psg-vector-signal-generator-100-khz-to-44-ghz>
- [56] —, “Keysight N9040B UXA signal analyzer, multi-touch, 2 Hz to 50 GHz,” 2018. [Online]. Available: <https://www.keysight.com/en/pdx-x202152-pn-N9040B/uxa-signal-analyzer-multi-touch-3-hz-to-50-ghz>